

All-fiber Raman probe

Anna Chiara Brunetti
Ph.D. Thesis
July 2012

All-fiber Raman probe

Ph.D. Thesis
Anna Chiara Brunetti

July 31st, 2012



DTU Fotonik
Department of Photonics Engineering
Technical University of Denmark
Ørstedes Plads 345A
DK-2800 Kgs. Lyngby
Denmark

Fatti non foste a viver come bruti,
ma per seguir virtute e canoscenza

*(You were not born to live like brutes,
but to follow virtue and knowledge)*

Dante Alighieri,
La divina Commedia
Inferno XXVI, 118-120

Contents

Preface	vii
Acknowledgements	ix
Abstract	xiii
Resumé (Danish abstract)	xv
PhD publication list	xvii
1 Introduction	1
1.1 The FøSu project	2
1.2 Thesis structure	4
2 Raman spectroscopy	7
2.1 Introduction	7
2.2 Raman spectra	8
2.3 Fundamentals of Raman scattering	11
2.3.1 A note on the coherence properties of Raman and Rayleigh scattering	16
2.3.2 Raman scattering cross-section	16
2.3.3 Limitations of the classical theory	17
2.4 Summary	18
3 Optical fiber Raman probes	19
3.1 Introduction	19
3.2 Fiber optic Raman probes	22
3.2.1 Multi-fiber probes	24
3.2.2 Single-fiber probes	25
3.2.3 Lensed probes	29
3.2.4 Externally filtered probes	30
3.3 Summary	31

4 Tunable all-in-fiber Rayleigh-rejection filter for Raman spectroscopy	33
4.1 Introduction	34
4.2 Photonic crystal fibers	37
4.2.1 Index-guiding fibers	38
4.2.2 Photonic bandgap fibers	39
4.2.3 Liquid-filled photonic bandgap fibers	40
4.3 Tunable Rayleigh-rejection filter based on liquid-filled PBG fiber	42
4.3.1 Filter realization	43
4.3.2 Filter application	47
4.4 Summary	51
5 Raman probe based on a double-clad fiber	53
5.1 Introduction	53
5.2 Raman probe based on double-clad fiber	57
5.2.1 Fiber cleaving and mounting	58
5.2.2 Experimental setup	60
5.2.3 Self-propelled catastrophic breakdowns	64
5.2.4 Raman spectra	64
5.3 Summary	67
6 Raman probes based on optically-poled double-clad fibers	69
6.1 Introduction	70
6.2 Optical poling	72
6.3 Raman probe based on an optically-poled double-clad fiber	74
6.3.1 Optical poling of the double-clad fiber	75
6.3.2 Experimental setup	78
6.3.3 Raman Spectra	80
6.4 Double-clad fiber coupler	83
6.4.1 Coupler fabrication	84
6.4.2 Experimental setup	88
6.4.3 Raman Spectra	89
6.5 Summary	92
7 Conclusion and future developments	93
7.1 Future developments	97
7.1.1 Novel applications	98
Acronyms	103
Bibliography	105

Preface

The work presented in this Thesis has been carried out as a part of my Ph.D. project in the period May 1st, 2009 to July 31st, 2012. The work mainly took place at DTU Fotonik (Technical University of Denmark, Department of Photonics Engineering), with the exception of a ~one year-long research stay spent at the Department of Fiber Photonics of the Research Institute Acreo AB (Kista, Sweden), under the supervision of Dr. Walter Margulis.

The Ph.D. project was financed by the Commission for Health, Food and Welfare of the Danish Council for Strategic Research, in the frame of the project “Towards robust fermentation processes by targeting population heterogeneity at microscale”, and supervised by

- K. Rottwitt (main supervisor), Professor, DTU Fotonik, Technical University of Denmark, Kgs. Lyngby, Denmark
- K.V. Gernaey (co-supervisor), Associate Professor, DTU Kemiteknik, Technical University of Denmark, Kgs. Lyngby, Denmark

Acknowledgements

I have never listened to anyone who criticized my taste in space travel, sideshows or gorillas. When this occurs, I pack up my dinosaurs and leave the room.

Ray Bradbury

You would not believe it.

All of this started four years ago, in front of a football field in São Pedro (Brazil), about 10400km away from here. I was attending my first conference, right after the end of my M.Sc. project, and in that particular moment I was talking to somebody, I cannot even remember whom, while watching some other conference attendees playing football. That's when the thought first hit me: this is what I want to do with my life.

This is what I wanted to do, research, and so I went back home, in Italy—back then “home” had a clear meaning, it only meant one thing—, and I applied for a Ph.D. project at DTU Fotonik, where I had spent a few months the previous winter. I had a clear plan, back then, nothing less than becoming the *best ever* Ph.D. student and completing my project with the *best ever* Ph.D. thesis. Never been an ambitious person, no.

Looking back at the last three years, I am not quite sure my old self would be 100% satisfied. This Thesis, *my work*, is probably quite far from the ideal of perfection she was asking me to achieve. I can almost hear her, When did she give me permission to lower the expectation bar?, and instead of feeling guilty I cannot help but smiling and just say, You have no idea what you are talking about. Sorry, kid: this time *I* know better.

Three years (and three months) have gone, since I started, and I have been stretching and crumpling up the meaning of the word “home” several times, in the meanwhile, adjusting it to distances and people. Leaving it behind, to have a place to go back to. Throwing it in front of me, to have something to look forward to.

Three years (and three months) have gone, since I started, and now I can say, in all honesty, that I am glad I did it. It has been exhausting, often disappointing, at times even *disgusting*, and I am relieved that I won't have to do it ever again. It has been strengthening, often satisfying, at times even *exciting*, and I am happy that I never gave up.

The Ph.D. experience has been formative from all perspectives. I feel like I learned so much, not *just* about fibers and physics but also, and above all, about myself.

If I have become a better person and a good researcher, if I made it through these challenging years, and if there is any value in the work presented in this Thesis, credit has to be given to the following people, without whom all of this would have been impossibly hard.

My supervisor, Professor **Karsten Rottwitt**, for giving me the opportunity to work at DTU Fotonik as a Ph.D. student, for his guidance during the project and for letting me hit my head against some *damn* hard walls, to prove me that I could handle it. Who would have thought.

My co-supervisor, Associate Professor **Krist V. Gernaey**, for always *making* the time to meet me and discuss about my results, or sometimes the lack of them, and for teaching me that, in the end, a Ph.D. is all about being proud of having done my best. I am.

Dr. **Walter Margulis**, for his encouraging guidance and brilliant suggestions, for always being ready to *throw me a lifebuoy* during the last-minute panic attacks of the Thesis writing process, and for never allowing me to believe that I would not get to the end of this Ph.D. project.

I believe not enough words have ever been invented, in English or Italian or any other language, to properly thank **Lara Scolari**. She has been at my side ever since my M.Sc. project, first as a supervisor, then as a colleague, and now as a dear friend. Credit goes to her for professional advice and for morally rescuing me from some of the lowest lows of the

last few years.

My sincere gratitude goes to **Walter Margulis, Lara Scolari, Johannes Weirich, Karsten Rottwitt** and **Viktor Nordell**, who took the time to proofread parts of this Thesis, point out its weaknesses, and suggest improvements.

I would like to thank **Thomas T. Alkeskjold** and **Lars-Ulrik A. Andersen**, for their help and support.

My colleagues at DTU Fotonik, especially **Anders T. Pedersen**, for always fixing *whatever* I ever tried to write in my terrible Danish, and for translating the abstract of this Thesis. My (past and present) office-mates, **Lara Scolari, Johannes Weirich, Lei Wei, Xiaomin Liu, Valentina Cristofori, Kristian R. Hansen** and **Casper Larsen**, for the good time and fruitful discussions in the office. The (past and present) colleagues I had the chance to work with, **Charlotte I. Falk, Danny Noordegraaf**, and **Toke Lund-Hansen**, for being extremely dedicated to our experiments.

Andrijana Bolic, from DTU Kemiteknik, probably the only person in the known universe able to explain me some chemistry without making me fall asleep on the spot, for the good and funny time in the lab.

My colleagues at Acreo, especially **Patrik Rugeland**, for helping out with the coupler, and my partner-in-crime **Aziza Sudirman**, for *force-feeding* me kilograms of chocolate and for turning “the girls corner” into one of the coziest places on earth.

Alessio, Aziza, Carolina, Elena, Irene, Maria, Pontus, Rachele, Valentina and all my friends.

Finally, I would like to express my deepest gratitude to **Viktor**, for keeping me sane all throughout the last few months, and to **my family**, without whom none of this would have been possible. “Home” is *anywhere* they are.

Abstract

The design and development of an all-in-fiber probe for Raman spectroscopy are presented in this Thesis.

Raman spectroscopy is an optical technique able to probe a sample based on the inelastic scattering of monochromatic light. Due to its high specificity and reliability and to the possibility to perform *real-time* measurements with little or no sample preparation, Raman spectroscopy is now considered an invaluable analytical tool, finding application in several fields including medicine, defense and process control.

When combined with fiber optics technology, Raman spectroscopy allows for the realization of flexible and minimally-invasive devices, able to reach remote or hardly accessible samples, and to perform *in-situ* analyses in hazardous environments.

The work behind this Thesis focuses on the proof-of-principle demonstration of a *truly* in-fiber Raman probe, where *all* parts are realized by means of fiber components. Assuming the possibility to use a fiber laser with a fundamental radiation at 1064nm, in-fiber efficient second harmonic generation is achieved by optically poling the core of the waveguide delivering the excitation light to the sample. In this way, Raman spectroscopy in the visible range can be performed. The simultaneous delivery of the excitation light and collection of the Raman signal from the sample are achieved by means of a double-clad fiber, whose core and inner cladding act as “independent” transmission channels. A double-clad fiber coupler allows for the recovery of the collected Raman scattering from the inner-cladding region of the double-clad fiber, thus replacing the bulk dichroic component normally used to demultiplex the pump and Raman signal. A tunable Rayleigh-rejection filter based on a liquid filled-photonic bandgap fiber is also demonstrated in this work.

The integration of the devices described in this Thesis allows for the

realization of a *complete* fiber Raman probe, where also the generation of the excitation radiation is done in-fiber.

Resumé (Danish abstract)

I denne ph.d.-afhandling præsenteres design og udvikling af en *all-in-fiber* sonde til Raman spektroskopi.

Raman spektroskopi er en optisk teknik, som ved hjælp af uelastisk spredning af monokromatisk lys er i stand til at undersøge en prøve . På grund af dens høje specificitet og pålidelighed, samt muligheden for at udføre målinger i real-tid uden nævneværdig forudgående behandling af prøven, anses Raman spektroskopi nu som et uundværligt analytisk redskab med anvendelser indenfor adskillige områder såsom medicin, forsvar og proces-kontrol.

Kombineret med fiberoptik giver Raman spektroskopi mulighed for at konstruere fleksible og ikke-invasive måleapparater, i stand til at nå svært tilgængelige steder, samt udføre in-situ analyser i farlige miljøer.

Denne afhandling fokuserer på en *proof-of-principle* demonstration af en all-in-fiber Raman sond, hvor samtlige dele består af optiske fiberkomponenter. Under antagelse af muligheden for at benytte en fiberlaser med en fundamental bølgelængde på 1064nm opnås effektiv *second harmonic generation* via optisk poling af fiberkernen, som leverer excitationslyset til prøven. På denne måde kan Raman spektroskopi i det synlige bølgelængdeområde udføres. Den samtidige levering af excitationslys og opsamling af Raman-signal fra prøven opnås ved hjælp af en *double-clad* fiber, hvis kerne og indre kappe fungerer som uafhængige transmissionskanaler. En double-clad fiber-kobler gør det muligt at genvinde Raman-signalet fra den indre kappe i double-clad fiberen, og denne komponent erstatter således den dikroiske komponent, som normalt bruges til at demultiplexe pumpe- og Raman-signalet. Desuden demonstreres et justerbart filter baseret på en fotonisk båndgabsfiber fyldt med flydende

krystaller til bortfiltrering af Rayleigh-spredt lys.

Ved integrering af komponenterne beskrevet i denne afhandling kan en komplet fiber Raman sonde realiseres, hvor også pumpelyset genereres i en fiber.

PhD publication list

Journal publications

1. **A.C. Brunetti**, W. Margulis, and K. Rottwitt, “Raman probes based on optically-poled double-clad fiber and coupler”, *Optics Express* 20: 28563-28572 (2012).
2. **A.C. Brunetti**, L. Scolari, T. Lund-Hansen, J. Weirich and K. Rottwitt, “All-in-fiber Rayleigh-rejection filter for Raman spectroscopy”, *Electronics Letters* 48(5):275–276 (2012).
3. R. Lencastre Fernandes, M. Nierychlo, L. Lundin, A.E. Pedersen, P.E. Puentes Tellez, A. Dutta, M. Carlqvist, A. Bolic, D. Schäpper, **A.C. Brunetti**, S. Helmark, A.-L. Heins, A.D. Jensen, I. Nopens, K. Rottwitt, N. Szita, J.D. van Elsas, P.H. Nielsen, J. Martinussen, S. J. Sørensen, A.E. Lantz, K.V. Gernaey, “Experimental methods and modeling techniques for description of cell population heterogeneity”, *Biotechnology Advances*, 29 (6): 575–599 (2011).
4. R.W. Berg, A. Riisager, O.N. Van Buu, R. Fehrmann, P. Harris and **A.C. Brunetti**, “X-ray Crystal Structure, Raman Spectroscopy and Ab Initio DFT Calculations on 1,1,3,3-Tetramethylguanidinium bromide”, *Journal of Physical Chemistry A*, 114(50):13175-13181 (2010).

Conference contributions

5. **A.C. Brunetti**, W. Margulis, and K. Rottwitt, “Raman probe based on optically-poled double-core fiber”. In *Optical Sensors*, Optical Society of America, paper STu1F.6 (2012).
6. **A.C. Brunetti**, L. Scolari, T. Lund-Hansen and K. Rottwitt, “Low-loss tunable all-in-fiber filter for Raman spectroscopy”. In *Optical Sensors*, Optical Society of America, paper SWA3 (2011).

7. **A.C. Brunetti** and K. Rottwitt, “Raman Scattering in a dimethyl sulfoxide-filled hollow-core photonic crystal fiber”. In *XXII International Conference on Raman Spectroscopy*, AIP Conference Proceedings, 1267, pages 796–797 (2010).
8. K. Nielsen, **A.C. Brunetti**, H. Pakarzadeh and K. Rottwitt, “Stimulated Raman scattering in microstructured polymer optical fibers”. In *Proceedings of SPIE*, Vol. 7714, Paper 7714-10 (2010).

Relevant publications from my M.Sc. Thesis

9. **A.C. Brunetti**, L. Scolari, J. Weirich, L. Eskildsen, G. Bellanca, P. Bassi and A. Bjarklev, “Gaussian filtering with tapered oil-filled photonic bandgap fibers”. In *Proceedings of 1st Workshop on Specialty Optical Fibers and Their Applications WSOF 2008*, São Pedro (SP), Brazil, pages 113-116 (2008).

Books chapters

10. K. Rottwitt, **A.C. Brunetti**, J. Lægsgaard, J. Weirich, L.S. Rishøj, X. Liu, L. Scolari, M.E.V. Pedersen, A.T. Pedersen, H. Steffensen, L. Wei, “Enhancing the capacity of light : biowatch: it’s time for a healthcheck”, book chapter in *Beyond optical horizons : today and tomorrow with photonics - 1 ed.* - Kgs. Lyngby, DTU Fotonik, 75-87 (2009).

Chapter 1

Introduction

Nothing is withheld from us
which we have conceived to do.

Russell A. Kirsch

Raman spectroscopy went from being an “esoteric” optical technique to becoming one of the most common analytical tools available today. This was made possible by the improvements in instrument technology during the second half of the twentieth century.

Besides the laser [1], inventions like the charge-coupled device (CCD) array detector [2] and small low-cost spectrometers have come to represent milestones in the widespread evolution of Raman spectroscopy, making it fast and reliable, and applicable to all kinds of samples. The possibility to bring the spectroscopic equipment outside the laboratory and to perform measurements in-field opened up for a wide range of applications, from art and archeology [3] to forensics and defense [4], from planetary science [5] to medicine [6–8].

The development of the first *fiber Raman probes* in the early eighties [9, 10] greatly enriched the possibilities of this spectroscopic technique. The combination of Raman spectroscopy and fiber technology allowed for the realization of flexible and minimally invasive devices, able to reach samples located far away from the laser source and spectrometer. The concept of *in-situ* real-time analysis was now extended to samples located in remote and/or hazardous environments. Untrained operators could perform the measurements, without worrying about alignment issues or their own safety. Raman investigations were soon carried out *in-vivo*, i.e. within a living organism. Biomedical applications in par-

ticular drove the development of such devices, ultimately bringing them *inside* the human body, inserted into catheters, endoscopes and needles [11–14].

When integrated into a small-size reactor, a fiber Raman probe serves as a real-time process monitoring sensor. The acquired spectral data provide direct information about the variables involved in the process and their correlation. Furthermore, the Raman signal represents an immediate feedback to the ongoing reaction, based on which real-time optimization of the process can be performed.

1.1 The FøSu project

This Ph.D. project finds its *raison d'être* in the frame of the FøSu Project, a name coined from the Danish words “Fødevarer” (food) and “Sundhed” (health)¹.

The FøSu project aims at investigating the mechanisms affecting the dynamics and level of cell heterogeneity in culture of microorganisms. The adjective “heterogeneous” in this case refers specifically to single-organism populations, whose cells differ the one from the other in terms of shape, size, gene pool and so on. While bench-scale bioreactors used for process development can be considered *homogeneous* environments to a good approximation, the same does not hold for large scale reactors used in industrial cultivations. This may be the reason for the lower yield and productivity resulting from scaled-up aerobic fermentation processes [15, 16]. However, it is believed that the impact of heterogeneity on a typical microbial population is not always detrimental. This property is in fact considered responsible for a quicker adaptation of the cells to new operating conditions, thus having a beneficial effect on the culture [17, 18].

Based on the hypothesis that there exists an *optimum* level of heterogeneity which leads to a robust fermentation process with sustained high productivity, the FøSu project represents a multi-disciplinary effort to develop suitable methodologies for controlling the level of heterogeneity in the population already at bench scale. As such, it combines analyses

¹The term FøSu represents a shortening of name of the Commission funding the project, namely the “Programkomiteen for Sundhed, Fødevarer og Velfærd” (Programme commission for Health, Food and Welfare) of the Danish Council for Strategic Research.

of molecular mechanisms at the cellular level with a thorough understanding of all process aspects and a quantitative description of the system. An excellent review of the experimental methods and modeling techniques for the description of cell population heterogeneity, assumed as the starting point of the project, is given in [19].

From an economic point of view, the optimization of industrial fermentation processes is extremely relevant for Denmark, whose companies produce more than 70% of all enzymes used worldwide via fermentation processes.

Essential to the real-time monitoring of a bioprocess is the integration of sensors in the system. Spectroscopic techniques such as Raman and infrared (IR) spectroscopy are commonly used to identify and characterize heterogeneity in microbial populations [20–22].

The main goal of this Ph.D. project was the design and development of an all-in-fiber Raman probe, compact enough to be integrated into a small-size bench-scale reactor (1 ÷ 2mL in volume, accomodates a probe up to ~ 4 mm in diameter) and *unfocused* not to compromise the cell viability. The device ought to be of simple operation, so that untrained personnel could use it, relatively cheap and portable. This last condition in particular relied on the outcome of a second Ph.D. project, aiming at the realization of a suitable fiber laser. Since this second project never started, the activity described in this Thesis was tailored to account for the lack of a custom-designed in-fiber light source.

Being in-fiber Raman spectroscopy a rather mature technique, efforts were made to demonstrate novel fiber solutions meant to improve and complete the work previously done by others, so that all the “building blocks” needed to realize a *truly* all-in-fiber Raman probe would be available.

In general, a Raman spectroscopic experiment requires the following steps:

1. Generation of the excitation light;
2. Delivery of the excitation light to the sample / Excitation of Raman scattering;
3. Collection of the scattered light;
4. Filtering of the collected light;
5. Detection of the filtered light.

As for the in-fiber generation of the excitation light, fiber lasers operating in the IR range are nowadays commercially available. The possibility to use such a device was therefore taken for granted. The attention was instead focused on the in-fiber wavelength conversion needed to excite Raman spectroscopy with visible light, an aspect never addressed before.

While a big effort had been made by others to optimize aspects like the delivery of the excitation light to the sample and the collection of the scattered radiation, little had been done as for the in-fiber demultiplexing of the two signals, whenever they are propagating simultaneously along the same waveguide. Given the importance of this aspect, the demonstration of a fiber demultiplexing component was addressed in this project.

The availability of fiber-based Rayleigh-rejection filters, a key component in a Raman spectroscopy experiment, was rather limited. A novel implementation of such a device was demonstrated in this work.

Despite a few previous attempts in this direction [23], the implementation of a spectrometer based on optical fiber technology was considered far from becoming a reality. Thus spectrometers based on a (bulk) dispersion grating and a CCD detector were used all throughout this project.

Due to lack of time, the solutions resulting from this Ph.D. could not be tested on a real bioreactor. However, the work here presented represents the first step towards the demonstration of a complete all-in-fiber Raman system, where everything except the spectrometer is made by optical fiber components.

1.2 Thesis structure

An introduction to Raman spectroscopy is given in Chapter 2, with main focus on the key aspects which are relevant to understand the work presented in this Thesis.

Chapter 3 presents an overview of the state-of-the-art in the field of fiber Raman probes. The advantages and disadvantages of single- and multi-fiber probe geometries are discussed, to clarify the challenges faced during this project and to better understand the design choices made.

A low-loss tunable Rayleigh-rejection filter based on a photonic crystal

fiber (PCF) infiltrated by a high-index liquid is described in Chapter 4. An introduction to PCFs is given at the beginning of the chapter, in order for the reader to understand the inherent spectral filtering action performed by a fiber guiding light by the photonic bandgap (PBG) effect, and how it is possible to tune such a spectral behaviour at will. The filter realization is described, and its spectral characteristic is compared to that simulated by means of a finite element method (FEM) code. The results of a Raman spectroscopy experiment based on the device, also presented in [24, 25], are then discussed.

Chapter 5 deals with a probe based on a double-clad fiber. The device allows for the propagation of the excitation light to the sample along its core and the collection of the scattering in its inner cladding. A bulk dichroic component is needed to demultiplex the laser and scattered radiation at the in-coupling section of the waveguide, thus allowing for the recovery of the collected Raman signal. The results of a Raman spectroscopy experiment carried out with this probe on a sample of cyclohexane are presented and discussed. Some practical issues faced during this activity are also described.

Chapter 6 represents an additional step forward towards the realization of an all-in-fiber Raman probe. Two single-fiber Raman probes are described, both based on optically-poled double-clad fibers. These devices represent one of the first practical applications of the (26-year-old) optical poling technique. After a brief introduction on optical poling, the realization of a Raman probe based on a single optically-poled double-clad fiber is described. The results of the application of such a device to the Raman spectroscopic investigation of a sample of dimethyl sulfoxide (DMSO), also reported in [26], are shown and discussed. The second device, a Raman probe based on a double-clad fiber coupler with one of its fibers optically-poled, is then introduced. The coupler realization is described and a Raman spectrum of a sample of DMSO acquired with such a probe is shown and discussed.

Chapter 7 concludes this Thesis, summing up the contribution of this project to the field of in-fiber Raman spectroscopy and glancing at some possible future developments of the work here presented.

Chapter 2

Raman spectroscopy

It's a crazy world out there.
Be curious.

Stephen Hawking

Raman spectroscopy is an optical probing technique based on the inelastic scattering of monochromatic light. As a result of the interaction between the incident radiation and the sample under study, wavelengths different from the excitation one are emitted. The analysis of the emitted spectrum provides qualitative and quantitative information about the molecular composition and structure of the sample. Due to its high specificity and reliability, Raman spectroscopy allows for the unambiguous identification of a wide range of samples in a fast and noninvasive way.

This chapter provides a brief introduction to Raman spectroscopy and the phenomenon of spontaneous Raman scattering, followed by an overview of the key aspects which are relevant to the work presented in this Thesis.

2.1 Introduction

The phenomenon of inelastic scattering of light, nowadays universally known as Raman scattering, was experimentally observed for the first time in 1928 by Raman and Krishnan [27], though its existence had been postulated five years earlier by Smekal [28]. However, it was not until the last decades of the twentieth century, with the invention of

the laser and the huge improvements in detector technology (above all the introduction of charge-coupled device array detectors [2, 29, 30] and Fourier-transform spectrometers [31]), that Raman spectroscopy could prove itself as the fast, reliable and invaluable analytical tool it is known as today. This is mainly due to the inherently weak nature of Raman scattering, with approximately 1 over 10^{10} incident photons undergoing inelastic scattering. Additionally, the detection of Raman scattering in the visible range is often impeded by the competing phenomenon of fluorescence, which is usually orders of magnitude more intense [32]. With the instrumentation currently available, Raman spectroscopy is now a mature technology which finds applications in several fields, ranging from chemistry and pharmacy [33] to medicine [6–8], forensics and defense [4], art and archeology [3] and process control [34].

Variations of Raman spectroscopy have been developed in the last few decades, mainly in an attempt to enhance the sensitivity of the process. Surface-enhanced Raman spectroscopy (SERS) [35], coherent anti-stokes Raman spectroscopy (CARS) [36, 37] and tip-enhanced Raman spectroscopy (TERS) [38] are just a few examples of these improved techniques.

2.2 Raman spectra

The qualitative and quantitative information resulting from Raman scattering is gathered in a Raman spectrum, i.e. a plot of the scattered intensity versus the wavelengths at which the scattering occurs. Modern spectrometers usually count photons rather than measure watts. Therefore, the intensity of the Raman signal is usually expressed in (photon) *counts*. Counts are often plotted versus *wavenumber shifts*, in units of inverse length (cm^{-1}), rather than versus wavelength. This allows for the fast comparison of spectra of the same sample, since when expressed in cm^{-1} the position of the Raman lines is always the same, regardless of the specific excitation wavelength used. In this way, a sample can be identified by simply comparing its Raman spectrum with a set of reference spectra, for instance digitally stored in a database. The same does not hold in case of spectra plotted versus wavelength, for which the position of the peaks shifts according to the *pump* wavelength. The conversion between wavelength and *Raman shift* (as a wavenumber shift is often referred to) can be done by means of the following equation

$$\Delta\text{Raman} = \frac{1}{\lambda_{\text{laser}}} - \frac{1}{\lambda_{\text{Raman}}} \quad (2.1)$$

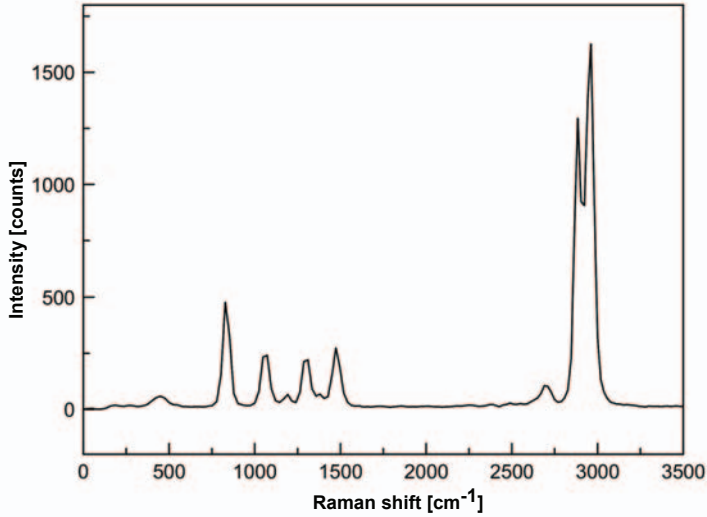


Figure 2.1: Raman spectrum of cyclohexane (C_6H_{12}), recorded over a 1s acquisition time. The measurement was repeated 3 times to avoid spectral artifacts. The intensity of the Raman bands, plotted versus wavenumbers, is here expressed in photon counts, common practice for modern spectrometers.

where λ_{laser} is the excitation wavelength and λ_{Raman} is the measured wavelength of a given peak. An example of Raman spectrum is shown in Fig. 2.1.

As wavelength and energy are related, a Raman spectrum is a plot of the scattered intensity versus energy. In particular, inelastic scattering results from the interaction of the incident radiation with the (vibrating) molecules of a given sample, causing photons to be emitted at different energies with respect to the excitation light. The position of each Raman peak corresponds to one of these energy shifts. Therefore, the combination of peak position and intensity provides information about the particular molecular vibration which caused the energy shift.

Elastically-scattered light (Rayleigh scattering) is instead characterized by same energy (wavelength) of the exciting radiation. Thus, the Rayleigh line occupies the position of zero shift (0 cm^{-1}) in the spectrum. The frequency of the inelastically-scattered photon is wavelength-shifted with respect to the incident photon by the emission or the absorption of a phonon. In the first case (emission of a phonon), a line appears in the spectrum at a longer wavelength than the pump light (Raman Stokes scattering). This corresponds to an energy transfer from the pump to

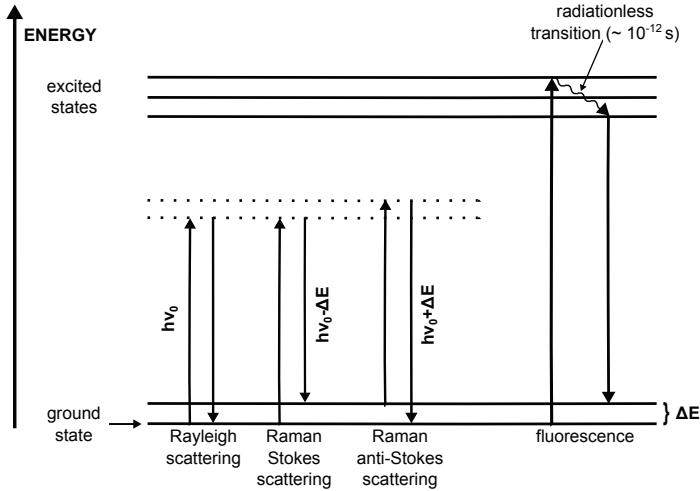


Figure 2.2: Spectroscopic transitions underlying Rayleigh and Raman spectroscopy and fluorescence. Rayleigh-scattered light has the same energy (wavelength) of the incident radiation, while Raman Stokes- and Raman anti-stokes-scattered light have a lower and higher energy than the excitation radiation, respectively. Fluorescence emission always has a lower energy than the incident beam. Raman scattering and fluorescence occur on different timescales (femtosecond and nanosecond, respectively).

the molecules. In the second case (absorption of a phonon) the line appearing in the spectrum is blue-shifted in relation to the pump (anti-Stokes Raman scattering). Thus, light is scattered with a higher energy than the incident radiation. The Stokes and anti-Stokes lines are located symmetrically about the Rayleigh line, though the peaks intensities on the two sides are normally very different [32]. This is due to the fact that, unless the molecules of the sample are already in an excited vibrational state during the scattering process (for instance if the temperature of the sample has been previously increased), Stokes Raman scattering is much more likely to happen. This can be understood by considering that, at thermal equilibrium, the number of atoms at different energy levels obeys the Boltzmann population distribution equation,

$$\frac{N_2}{N_1} = e^{-\frac{E_2 - E_1}{kT}} \quad (2.2)$$

where N_1 and N_2 are the number of atoms at energy state E_1 and E_2 , respectively, k is the Boltzmann constant (8.6×10^{-5} [eV/K]) and T is the temperature. If the energy shift $\Delta E = E_2 - E_1 \gg kT$, then $N_2 \ll N_1$. For this reason, only the Stokes side of the spectrum is

normally considered, due to the higher intensity of the Stokes-scattered light compared to the anti-Stokes-scattered light.

An energy level diagram like the one shown in Fig. 2.2 provides an intuitive explanation of the energy exchanges underlying the generation of the Raman lines. Scattering may occur whenever the energy of the incident light is not sufficient to promote a large electronic transition, the base of fluorescence, as also indicated in Fig. 2.2 for comparison. In this latter case, incident light is absorbed by a fluorescent molecule, or *fluorophore*, which is promoted to an excited level. After a fast nonradiative decay at high energy configurations, the fluorophore eventually reaches the lowest energy excited state, which is metastable. Next, the fluorophore returns to its ground state, and the excess energy is emitted as light. Longer excitation wavelengths, i.e. smaller excitation energies, may cause Rayleigh and Raman scattering, but not the appearance of fluorescence. In other words, scattering can occur for *any* wavelength of the excitation radiation, while the same does not hold for fluorescence.

2.3 Fundamentals of the classical theory of Raman scattering

A theoretical treatment of Raman scattering can be done in a classical and quantum mechanical way. Both approaches relate the scattered radiation to the oscillating electric and magnetic multipole moments induced in a molecule by an incident electric field, the most significant of which is normally the oscillating electric dipole [39]. Although a description in terms of classical mechanics does not account for the quantized nature of vibrations and is therefore deficient, it does provide enough insight into the subject to understand the work presented in this Thesis, and in addition it is considerably simpler. For this reason, only a classical treatment of the phenomenon is considered in this Chapter.

What follows is based on the *microscopic* approach presented in [39], where the interaction between monochromatic radiation and a *single* scattering molecule is considered. Only the aspects which are important to understand the results discussed in the next Chapters of this Thesis are here reported. The reader who wants further and more detailed information is encouraged to check the excellent “The Raman Effect” by Long [39].

The radiation is treated as a plane wave of frequency ω_1 , while the molecule is assumed to be free to vibrate but not to rotate. For simplicity, a single molecule is considered here.

Upon illumination with plane monochromatic waves of frequency ω_1 , an oscillating electric dipole is induced in a molecule, responsible for the scattering of light by the molecule itself. The intensity radiated by such a dipole along a direction forming an angle θ with its axis, in terms of time-averaged power per unit solid angle, is given by

$$I = k'_\omega \omega_s^4 p_0^2 \sin^2 \theta \quad (2.3)$$

where p_0 is the amplitude of the induced dipole with frequency ω_s , generally different from ω_1 and

$$k'_\omega = \frac{1}{32\pi^2 \varepsilon_0 c_0^3} \quad (2.4)$$

where c_0 and ε_0 are the velocity of light in vacuum and vacuum dielectric permittivity respectively. Eq. (2.3) shows that the scattered intensity I at a particular frequency is determined by the amplitude of the induced electric dipole at that frequency. Moreover, it is worth noting that the scattered intensity is proportional to the fourth power of the scattered frequency ω_s . The total time-dependent induced electric dipole moment vector of the molecule can be approximated by its linear term,

$$\mathbf{p} \approx \mathbf{p}^{(1)} = \overline{\overline{\alpha}} \cdot \mathbf{E} \quad (2.5)$$

where \mathbf{E} represents the time-dependent electric field vector of the incident monochromatic radiation of frequency ω_1 ,

$$\mathbf{E} = \mathbf{E}_0 \cos(\omega_1 t) \quad (2.6)$$

and $\overline{\overline{\alpha}}$ is the polarizability tensor of the molecule, function of its molecular vibrational frequencies. The polarizability is a material property, different for different molecules. Thus, Eq. (2.5) relates the dipole to the electric field inducing it, through the properties of the molecule.

The polarizability of a molecule is affected by molecular vibrations, which are usually considered to be composed of normal modes, i.e. synchronous motions of atoms or groups of atoms that may be excited independently, without leading to the excitation of other normal modes. A vibration implies a periodic displacement of the (nuclei of the) atoms of the molecule from their equilibrium configuration. In general, a molecule

with N atoms has $3N - 6$ normal modes of vibration. This number increases to $3N - 5$ for a linear molecule, i.e. a molecule whose atoms are arranged on a straight line, as is carbon dioxide (CO_2), for instance. As an example, Fig. 2.3 shows the three normal modes of vibration of water, for which $N = 3$. The k -th mode is represented by the normal coordinate Q_k , associated with the molecular vibrational frequency ω_k . This coordinate refers to the position of the atoms of the molecule with respect to their equilibrium position.

A single normal mode of vibration Q_k is considered. Assuming harmonic motion, where a variation of the polarizability in a vibration is proportional to the first power of Q_k , the dependence of the polarizability on the molecular vibrations can be expressed (in component form) as a perturbation of the equilibrium condition, as follows

$$(\alpha_{\rho\sigma})_k = (\alpha_{\rho\sigma})_0 + (\alpha'_{\rho\sigma})_k Q_k \quad (2.7)$$

where

$$(\alpha'_{\rho\sigma})_k = \left(\frac{\partial \alpha_{\rho\sigma}}{\partial Q_k} \right)_0 \quad (2.8)$$

and $(\alpha_{\rho\sigma})_0$ is the value of $\alpha_{\rho\sigma}$ at the equilibrium configuration. The subscript 0 on the derivatives indicates that these have to be taken at the equilibrium. Given its validity for all tensor components Eq. (2.7) can be reformulated in the following way

$$\bar{\alpha}_k = \bar{\alpha}_0 + \bar{\alpha}'_k Q_k \quad (2.9)$$

where Q_k is a scalar quantity which multiplies all components of $\bar{\alpha}'_k$.

Assuming now that the restoring force of the vibration is proportional to the first power of its displacement Q_k (*mechanical harmonicity*), the normal coordinate Q_k can be expressed as

$$Q_k = Q_{k0} \cos(\omega_k t + \delta_k) \quad (2.10)$$

where Q_{k0} is the coordinate amplitude and δ_k its phase vector. The value of $\bar{\alpha}_k$ obtained by combining Eq. (2.9) with Eq. (2.10) can now be inserted into Eq. (2.5), together with the electric field vector given by Eq. (2.6). Thus, the linear induced dipole can be written as

$$\mathbf{p}^{(1)} = \bar{\alpha}_0 \mathbf{E}_0 \cos(\omega_1 t) + \bar{\alpha}'_k \mathbf{E}_0 Q_{k0} \frac{\cos((\omega_1 + \omega_k)t + \delta_k) + \cos((\omega_1 - \omega_k)t - \delta_k)}{2} \quad (2.11)$$

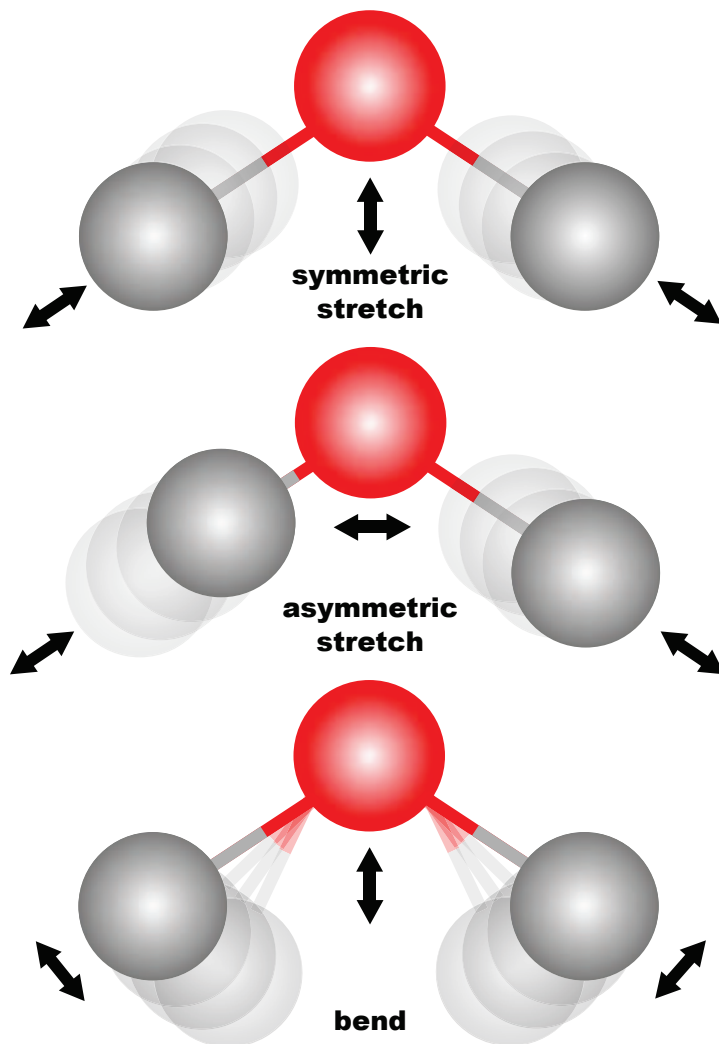


Figure 2.3: Normal modes of vibration of a molecule of water (H_2O): from the top, symmetric and asymmetric stretch and bend. Indicated in red is the atom of oxygen, while the atoms of hydrogen are shown in white. Black arrows mark the directions in which the nuclei of the atoms vibrate about their equilibrium positions.

Eq. (2.11) shows that the linear induced dipole has three distinct frequency components, ω_1 and $\omega_1 \pm \omega_k$, whose amplitude is linearly dependent on \mathbf{E}_0 :

$$\mathbf{p}^{(1)} = \mathbf{p}^{(1)}(\omega_1) + \mathbf{p}^{(1)}(\omega_1 + \omega_k) + \mathbf{p}^{(1)}(\omega_1 - \omega_k) \quad (2.12)$$

where $\mathbf{p}^{(1)}(\omega_1)$ is proportional to the *classical scattering Rayleigh tensor*, $\overline{\overline{\alpha}}^{\text{Ray}} = \overline{\overline{\alpha}}_0$, whereas $\mathbf{p}^{(1)}(\omega_1 \pm \omega_k)$ is proportional to the *classical Raman scattering tensor* $\overline{\overline{\alpha}}_k^{\text{Ram}} = \frac{1}{2}\overline{\overline{\alpha}}'_k Q_{k0}$.

Unlike $\overline{\overline{\alpha}}_k^{\text{Ray}}$, which is an equilibrium polarizability tensor, $\overline{\overline{\alpha}}_k^{\text{Ram}}$ is a polarizability tensor associated with ω_k . The induced dipole $\mathbf{p}^{(1)}(\omega_1)$ has the same phase as the incident field and is responsible for radiation at ω_1 (Rayleigh scattering). The induced dipoles $\mathbf{p}^{(1)}(\omega_1 \pm \omega_k)$ give instead rise to radiation at $\omega_1 + \omega_k$ (anti-Stokes Raman scattering) and $\omega_1 - \omega_k$ (Stokes Raman scattering), and are shifted in phase relative to the incident field by a quantity δ_k . δ_k defines the phase of the normal vibration Q_k relative to the field, and is in general different for different molecules. It is worth noting that $\mathbf{p}^{(1)}(\omega_1)$ is proportional to $\overline{\overline{\alpha}}_0$, the inherent polarizability of the molecule, while $\mathbf{p}^{(1)}(\omega_1 \pm \omega_k)$ are proportional to $\overline{\overline{\alpha}}'_k$, whose components are usually smaller in value than those of $\overline{\overline{\alpha}}_0$. Thus, Raman scattering is generally much weaker than Rayleigh scattering.

From Eq. (2.11) it is also possible to deduce the primary selection rule for Raman activity: in order for Raman scattering associated to a molecular frequency ω_k to arise, at least one of the components $(\alpha'_{\rho\sigma})_k$ of the derived polarizability tensor $\overline{\overline{\alpha}}'_k$ (thus of $\overline{\overline{\alpha}}_k^{\text{Ram}}$) must be non-zero. That is, only vibrations that change the polarizability of the molecule yield Raman scattering. In other words, Raman scattering arises from the electric dipoles oscillating at $\omega_1 \pm \omega_k$, which are produced when the electric dipole oscillating at ω_1 is modulated by the molecular vibrations at ω_k . The nuclear motions are coupled to the electric field by the rearrangement of the electrons, which imposes a harmonic variation on the polarizability. Rayleigh scattering, on the other hand, is always present: the condition for its existence is in fact that $\overline{\overline{\alpha}}^{\text{Ray}}$ be non-zero, which is true for all molecules.

By substituting the squares of the appropriate components of the classical electric dipole amplitudes $\mathbf{p}^{(1)}(\omega_1)$ or $\mathbf{p}^{(1)}(\omega_1 \pm \omega_k)$, into Eq. (2.3), it is possible to calculate the scattering intensity at a particular frequency.

2.3.1 A note on the coherence properties of Raman and Rayleigh scattering

A treatment based on a single scattering molecule space-fixed in its equilibrium configuration is generally deficient, since material systems are normally composed by a large number of molecules, whose orientation is not necessarily fixed. However, Raman scattering bears an arbitrary phase relation to the incident radiation, since its phase depends on the phase of the molecular vibration (δ_k in Eq. (2.11)), which to a good approximation varies arbitrarily from molecule to molecule. Thus, all molecules in the material system of interest act as independent sources of radiation, regardless of the degree of correlation between their positions. Assuming an incoherent Raman scattering does not represent an unrealistic constraint¹. The same cannot be said about Rayleigh scattering, which is instead in phase with the incident radiation, as can be seen from Eq. (2.11). In this case, interference between the scattering from different molecules may occur, depending on the specific arrangement of the molecules, and different observation directions may lead to different degrees of coherence.

2.3.2 Raman scattering cross-section

The relationship between the intensity I of Raman and Rayleigh scattered radiation from a single molecule (see Eq. (2.3)) and the irradiance \mathcal{I} of the incident radiation has the general form

$$I = \sigma' \mathcal{I} \quad (2.13)$$

where σ' , with the unit $\text{m}^2 \text{sr}^{-1} \text{molecule}^{-1}$, is defined as the (*first differential scattering cross-section*) of the molecule. A typical value for σ' is of the order of $10^{-31} \text{cm}^2 \text{sr}^{-1} \text{molecule}^{-1}$.

For the purpose of comparing the scattering efficiency of different molecules, it is useful to introduce scattering cross-sections, due to their dependance on molecular properties rather than on the irradiance of the incident radiation. Different definitions of scattering-cross section exist, the most common of which is the one resulting from Eq. (2.13), that is

¹In the regime where *stimulated* Raman scattering occurs, the Stokes photons may be emitted in phase with the local Stokes wave, and the incoherent assumption breaks down.

$$\sigma' = \frac{I}{\mathcal{I}} \quad (2.14)$$

The magnitude of the cross-section, *empirically* determined, gives a direct indication on the strength of the Raman signal from a given molecular system. In the following Chapters of this Thesis, the indication of a sample as a “strong” or “weak” Raman scatterer always relates to the magnitude of its Raman scattering cross-section. As an example, the values of scattering cross-sections for the peaks located at 802, 1030, 1273 and 1450 cm^{-1} of liquid cyclohexane (C_6H_{12}), as they appear in [40], are listed in Table 2.1 (in units of $\text{cm}^2 \text{sr}^{-1} \text{molecule}^{-1}$).

Raman peak [cm^{-1}]	Raman cross-section [$\text{cm}^2 \text{sr}^{-1} \text{molecule}^{-1}$]
802	9.06×10^{-30}
1030	5.37×10^{-30}
1273	4.61×10^{-30}
1450	6.17×10^{-30}

Table 2.1: Raman scattering cross-sections of selected Raman lines of cyclohexane (adapted from [40]).

2.3.3 Limitations of the classical theory

The classical approach reported in this chapter offers some useful qualitative insights but does not represent a complete treatment of all aspects of Raman spectroscopy. The frequency dependence of the scattered light resulting from the classical theory is correct, as well as the relation between the Rayleigh scattering tensor and the equilibrium polarizability tensor $\overline{\alpha}_0$. The dependence of the *vibrational* Raman scattering tensor on the derived polarizability tensor $\overline{\alpha}'_k$ is also partially correct. On the other hand, this approach cannot account for *rotational* Raman scattering, since the classical theory does not ascribe specific discrete rotational frequencies to molecules. In other words, the quantum mechanical expression of the Raman scattering tensor is different from the classical Raman scattering tensor $\overline{\alpha}_k^{\text{Ram}}$, owing to a different formulation of the amplitude Q_k of the molecular vibration. Also, the classical treatment cannot relate the properties of the tensor $\overline{\alpha}'_k$ to those of the scattering molecule and the incident radiation. Thus, it has to be remembered that a complete and quantitative analysis of Raman scattering requires a quantum mechanical approach. Nevertheless, the brief classical treatment provided in this chapter outlines some of the key-aspects of Raman

spectroscopy, and is enough to understand the work reported and discussed in the following chapters of this thesis.

2.4 Summary

In this chapter, a general introduction to Raman scattering and Raman spectroscopy is given. The fundamentals of the classical theory of incoherent Raman and Rayleigh scattering arising from a single molecule, vibrating though not rotating are introduced. A few key-aspects of the classical theory of Raman spectroscopy are highlighted, that is

- The dependence of the intensity of the scattered light on the *fourth* power of the scattered frequency, that is on λ_s^{-4} , where λ_s is the scattered wavelength;
- For *each* molecular vibration, the linear induced dipole usually has *three* distinct spectral components, one at the same frequency ω_1 of the incident radiation (Rayleigh scattering) and two more at frequencies $\omega_1 \pm \omega_k$, where ω_k is the frequency of the molecular vibration (Stokes and anti-Stokes Raman scattering);
- Raman scattering is considerably weaker than Rayleigh scattering, and unlike Rayleigh scattering it bears an arbitrary phase relation to the incident radiation;
- Only vibrations which change the polarizability of the molecule yield Raman scattering (primary selection-rule for Raman activity), whereas Rayleigh scattering is always present;
- Different samples can be identified as “strong” or “weak” Raman scatterers, depending on their Raman cross-section.

Finally, the limitations of the classical approach are also briefly discussed.

Chapter 3

Optical fiber Raman probes

If I have seen further it is by
standing on ye sholders of Giants.

Isaac Newton

The combination of Raman spectroscopy and optical fiber technology allows for real-time *in situ* analysis of samples located in remote and hardly accessible or hazardous environments, in a minimally invasive and non-destructive way. For this reason, fiber Raman probes have found application in several fields, from medicine to process control.

This chapter begins with an overview of the main functionalities required from a probe for its use in Raman spectroscopy, given in Section 3.1. A brief discussion follows on the development of fiber probes, in Section 3.2, with a short description of the advantages and disadvantages of the single- and multi-fiber geometries. A final comment on the integration of lenses and filters in the probe head closes the chapter (Subsections 3.2.3 and 3.2.4).

3.1 Introduction

Raman spectroscopy relies on the illumination of a sample under study with monochromatic light, usually from a laser, and on the collection and analysis of the scattered light. Since Raman scattering is always

accompanied by the much more intense Rayleigh scattering, the collected radiation is usually filtered prior to its delivery to the detector in order to remove, or at least attenuate, the intense Rayleigh line. In other words, a Raman spectroscopic experiment usually consists of the following, consecutive steps:

1. Generation of the excitation light;
 2. Delivery of the excitation light to the sample / Excitation of scattering;
 3. Collection of the scattered light;
 4. Filtering of the collected light;
- and
5. Detection of the filtered light,

where the detection includes the spectroscopic analysis of the collected signal. Fig. (3.1) schematically illustrates this procedure, in the form of building blocks needed to perform a Raman experiment. Two main *paths* can be identified by looking at the previous list: an *excitation path*, along which the laser radiation is delivered to the sample (item no. 2 of the list), and a *collection path*, along which the scattering is collected, filtered and conveyed to the detector (items no. 3 and 4). The light generation and detection (items no. 1 and 5) fall outside this path structure (see Fig. (3.1)). Simply put, a Raman probe is an interface between the light excitation and detection stages and the sample under study. The design of such a probe is driven by maximal light collection, and it is usually complicated by several constraints resulting from the specific application. If for instance a probe is meant to be integrated in an endoscope, then it has to be compact and flexible, and to operate in a backscattering configuration (180° between the excitation and collection) [41]. Moreover, in case of clinical applications biocompatibility issues (optical radiation and thermal hazards, material toxicity hazards, etc) limit the range of possible materials to use [11]. Contamination issues may require the probe design to account for the presence of a container (especially in case of liquids) or a window of a given thickness. Hazardous environments may impose a given minimum distance between the actual probe head and the operator, and so on. The definition of a specific application, that is of a specific sample, also results in constraints as for the choice of the detector and of the wavelength and power of the excitation source, which in turn translate into additional

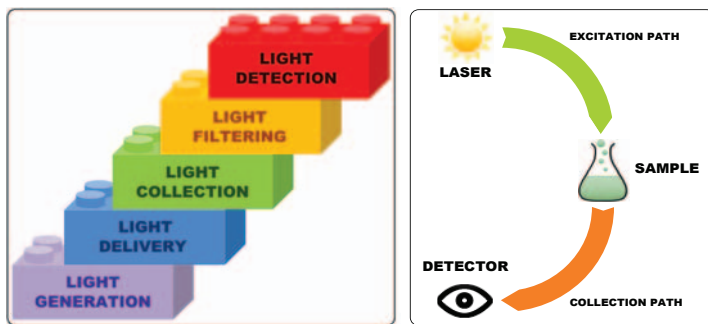


Figure 3.1: LEFT. Schematic illustration of the consecutive steps required for a Raman experiment. Monochromatic light, usually generated by a laser, is delivered to a sample. The scattering is then collected and filtered, so that only the Raman-scattered light can be delivered to a detector and analysed. RIGHT. Re-arrangement of the previous steps into two main *paths*: an *excitation path*, from the laser to the sample, and a *collection path*, inclusive of the signal filtering step, from the sample to the detector.

constraints on the spectrometer¹. When dealing with living cells, for instance, long exposure times and high intensities may result in a permanent damage to the cells, thus limiting the maximum intensity of the excitation light and irradiation time [42–45]. Additionally, fluorescent samples may require an excitation wavelength long enough to ensure that no fluorescence is generated [46], though this translates into a reduced intensity of the Raman scattered light, which is proportional to λ^{-4} . Long excitation wavelengths on the other hand may require the use of array detectors based on germanium (Ge) or indium gallium arsenide (InGaAs), since the cut off of silicon-based charge-coupled device (CCD) detectors is very close to 1064nm, i.e. the wavelength produced by a Nd:YAG laser. Tunable lasers can also be employed to distinguish the Raman signal from fluorescence, since the former follows the excitation wavelength as the pump is tuned, while the fluorescent emission remains at the same absolute wavenumbers [47, 48]. Alternatively, a time-gated detector can be used to counteract fluorescence, given that its emission takes place over a nanosecond scale, while Raman scattering usually occurs on a femtosecond scale [49]. Moreover, anti-Stokes scattering might be preferred to Stokes scattering, since the former is not affected by fluorescence, which always occurs at longer wavelengths than the exciting

¹The necessity to separate the collected Raman signal into its spectral components requires the presence of a dispersive element, usually a grating, together with the detector. Thus, spectrometers are normally used.

radiation.

3.2 Fiber optic Raman probes

The development of fiber optic Raman probes has been driven mainly by biomedical applications, in particular by the need for minimally invasive and highly accurate diagnostic techniques. Fiber technology allows for the realization of compact and flexible devices, which can easily be integrated into narrow-diameter medical instruments such as catheters, endoscopes and needles [11–14]. Nevertheless, the desire for non-destructive real-time *in situ* interrogation of remote, hardly accessible and potentially hazardous samples is not a prerogative of clinical applications. Fiber-based Raman spectroscopy offers the possibility to probe samples without compromising the safety of the operators. This, in addition to the fact that Raman spectroscopy requires minimal or no sample preparation and can be applied to all optically accessible samples, encouraged the application of fiber Raman probes to the fields of (among others) defense and security (for example for the detection of explosive materials [50, 51]), forensics [52] and in the monitoring of hazardous industrial reactions (for instance in the presence of highly toxic solvents [53]).

In-fiber Raman spectroscopy is rather mature, and a variety of probe geometries have been demonstrated over the last three decades. Some of these probes have actually made it to the field, usually those based on both fiber and bulk components, while many others have never left the lab in which they were fabricated. Several manufacturers nowadays sell compact *fiber Raman probes*, whose design normally represents a variation of that first suggested by Carrabba and Rauh [54] and schematically shown in Fig. 3.2. These probes, often termed *externally filtered*, incorporate additional optical filtering in between the fibers and the sample, in order to discriminate against the Rayleigh-scattered light and the silica background, i.e. the Raman and fluorescence spectrum of silica excited throughout the fiber.

The work described in this Thesis deals with both single- and multiple-fiber configurations. In this Chapter only probes operating in a backscattering geometry, i.e. with an angle of 180° between the excitation and collection directions, are considered. Backscattering is intuitive with single-fiber probes, where the same waveguide simultaneously delivers

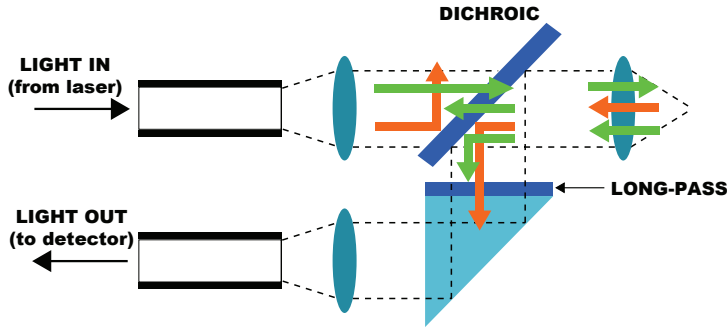


Figure 3.2: Schematic illustration of the fiber Raman probe designed by Carrabba and Rauh [54]. Laser radiation is coupled to the excitation fiber and then collimated by a lens at the fiber end. Next in line is a dichroic component which transmits the excitation light and reflects all other wavelengths, including those generated by the Raman and fluorescence emission of the fiber. The beam is then focused on the sample by a lens which is also used to collimate the collected backscattered radiation. The dichroic component reflects all wavelengths which are different than the excitation one, thus providing a first filtering of the Rayleigh scattering. An additional Rayleigh-rejection is performed by a long-pass filter. The residual Raman signal is then coupled to the collection fiber through a prism and a lens, and conveyed to the spectrometer.

the excitation light to the sample and collects the scattering. Multi-fiber probes are usually realized by assembling a single excitation fiber with one or more collection fibers, arranged so that the backscattering Raman signal is collected.

The delivery of the excitation through a fiber bundle was demonstrated in a Raman experiment by Trott and Furtak [9] in 1980. However, it proved to be rather inefficient, owing to the radiation lost to both the fiber cladding and the binding material surrounding each fiber. For this reason, in follow-up experiments a single excitation fiber has been often preferred [55]. Furthermore, in this work only multi-mode fibers have been employed (or single-mode fibers used at shorter wavelengths than the cut-off value). These are known to scramble the polarization of the laser emission except over short fiber lengths [32, 55]. Therefore the depolarization ratio of the Raman bands, i.e. the ratio between the Raman intensity observed from a direction perpendicular to the polarization of the excitation light and that observed from a parallel direction, is not considered in this Thesis.

In the rest of this chapter the attention is focused on the spectroscopic analysis of liquid samples. Reports of applications of fiber Raman probes

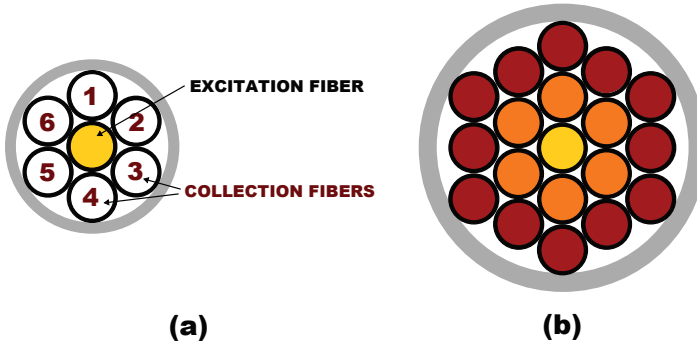


Figure 3.3: Schematic representation of n -around-1 fiber bundles with equal-sized fibers. (a) 6-around-1 bundle; (b) 18-around-1. The excitation fiber is coloured in yellow, while the fibers belonging to the first and second outer rings are marked in orange and red, respectively. The hexagonal packing of the waveguides ensures the smallest possible round cross section.

to solid or gaseous samples can be found in the literature, for example in Cooney et al. [56, 57] and Berg et al. [58].

3.2.1 Multi-fiber probes

The simplest multi-fiber Raman probe operating in a backscattering configuration is assembled by putting together two optical fibers, one fiber in charge of delivering the laser radiation to the sample, and the second one, parallel to the first, responsible for the collection of the scattered light and its delivery to the spectrometer. Such a configuration was demonstrated for the first time in 1983 by McCreery et al. [10]. In the same work, the authors suggested that the probe efficiency could be improved by employing several collection fibers, concentrically arranged around the excitation fiber, as schematically shown in Fig. 3.3 in the case of equal-sized fibers. A single collection fiber placed parallel to the illumination fiber is in fact a relatively poor collector, due to the small geometrical overlap between the the excitation and collection fibers light cones, i.e. the volume from which the scattered light is actually sampled. Provided that the cladding layer of the fibers is thin enough, the bundled arrangement suggested in [10] represents an improvement with respect to the single-collection-fiber geometry (not to be confused with the single-fiber geometry), owing to its ability to sample a larger volume [55, 59].

Fig. 3.4 schematically illustrates the overlap of illumination and collec-

tion light cones resulting from different fiber arrangements in the case of waveguides with the same diameter. In particular, in this picture the two aforementioned schemes are labelled with the letters (b) (single-collection-fiber) and (h) (fiber bundle).

Multiple rings of collection fibers are often arranged hexagonally around the illumination fiber (as depicted in Fig. 3.3 (b)). For this reason, the bundled geometry is sometimes referred to as *n-around-1*, where n represents the total number of collection fibers [55]. The hexagonal packing of the $n + 1$ equal-sized optical fibers allows for the smallest possible (round) cross section of the bundle, as explained by Utzinger and Richards-Kortum [11].

Raman probes based on bundles of fibers with different dimensions have also been demonstrated in the literature [60], though in this case the waveguides cannot be packed as efficiently as in the previous case, thus resulting in a smaller overlap of illumination and collection cones and therefore limiting the inherent advantage of having multiple collection fibers.

Probes with beveled exit surfaces, i.e. polished at an angle with respect to the fiber axis, can also be employed to achieve a larger overlap of the excitation and collection volumes, by deflecting them the one towards the other. A probe based on two parallel beveled fibers is at least 1.5 times more efficient than its analogous based on flat fibers of the same kind [11].

3.2.2 Single-fiber probes

An alternative to multiple-fiber probes are single-fiber probes, which have the inherent advantage of a complete overlap of excitation and collection light cones at all distances from the fiber end facet, as shown in Fig. 3.4 (a). A probe consisting of a single fiber is 1.4 to 1.8 times (depending on the fiber diameter) more efficient than one based on two parallel fibers with a flat tip [11]. Moreover, single-fiber probes have no *dead volume*, i.e. the region of no light-cone overlap which exists in between the fiber end facets and the minimum distance at which the scattered signal can be collected. Only when the sample-to-probe distance is greater than this minimum distance, in fact, there is any collection of the scattering by the collection fiber(s) [55]. The dead volume is instead present with all multi-fiber designs, as shown in Fig. 3.4. Additionally, single-fiber probes are more compact than multi-fiber

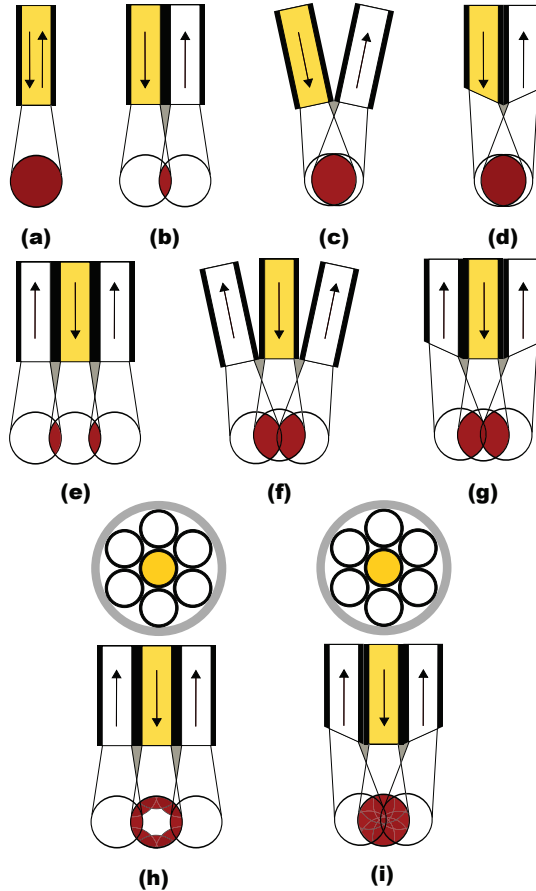


Figure 3.4: Schematic illustration of the overlap of excitation and collection light cones in case of different fiber probe configurations: (a) single-fiber probe; (b) two-fiber probe with parallel fibers and flat tips; (c) two-fiber probe with excitation and collection fibers angled the one towards the other; (d) two-fiber probe with parallel fibers and beveled tips; (e) three-fiber probe with parallel fibers and flat tips; (f) three-fiber probe with collection fibers angled inwards, towards the excitation fiber; (g) three-fiber probe with parallel fibers and collection fibers with beveled tips; (h) 6-around-1 fiber bundle with parallel fibers and flat tips; (i) 6-around-1 fiber bundle with parallel fibers and collection fibers with beveled tips. In all probe geometries, the excitation fiber is marked with a yellow colour, while the dead volume, whenever present, is coloured in grey.

ones, and at least for long fiber lengths usually much cheaper than those based on fiber bundles [61].

One drawback of the single-fiber geometry is related to the demultiplexing of the excitation and scattered radiation at one end of the fiber. The recovery of the collected light is usually performed by a bulk component such as a dichroic mirror or a beam splitter, whose losses counterbalance the gain in efficiency due to the total superimposition of the light cones [55].

The second and main drawback lies in the fact that such a configuration yields a larger silica background, i.e. the Raman and fluorescence spectrum of silica excited throughout the fiber, than multiple-fiber geometries. This signal, often referred to as fiber spectral background (FSB), is transmitted through the fiber to the spectrometer. The FSB can at best degrade the signal from the sample and at worst completely obscure it. As an example, Fig. 3.5 shows the spectrum of dimethyl sulfoxide (DMSO) acquired with a single-fiber probe: while the Raman peaks at higher wavenumbers are clearly visible, those located at lower wavenumbers are completely masked by the background emission from silica. Multi-fiber geometries, especially when used in conjunction with transparent liquids, are less affected by this background signal. The excitation radiation is in fact transmitted through the sample, and the only signal from silica that effectively couples back to the detector is that generated by the Rayleigh-scattered light along the collection fibers. This signal is less intense than the FSB generated by the primary laser radiation in the excitation fiber, since the latter is several orders of magnitude more intense than the elastically-scattered light [55, 62]. The same does not hold in case of a highly scattering sample. In fact, in this case the background emission from the excitation fiber is scattered and collected by the collection fiber(s) [61].

Myrick et al. [61] investigated the origins of background emission in silica fibers, and found that FSB arises in both core and cladding, though the signal from the core is more intense than that from the cladding for a proper in-coupling of the laser light to the fiber, due to the presence of the dopant. Ma and Li [63] extended the previous work by varying the distribution of light in the cladding and coating of the fiber, even coiling the waveguide around a pencil of small diameter, and found that the background signal originating from these regions represents a very small contribution to the overall background behaviour. This is mainly due to the fact that the FSB generated in the cladding and coating cannot be guided along the fiber, while that generated in the core and scattered

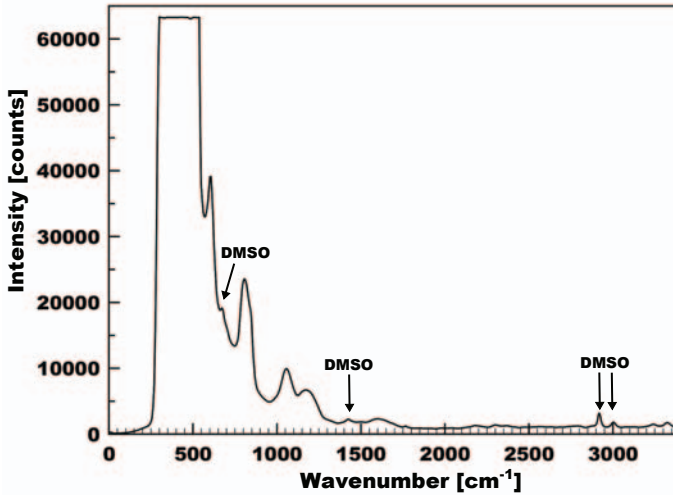


Figure 3.5: Raman spectrum of dimethyl sulfoxide (DMSO) acquired with a single-fiber probe over a 15s-acquisition time, repeated twice to avoid artifacts in the spectrum. While the DMSO peaks at higher wavenumbers are visible, those located at lower wavenumbers are partly or completely masked by the fiber background (for a complete list of Raman bands of DMSO, see Table 6.1).

at an angle which satisfies the total internal reflection (TIR) condition at the core/cladding interface propagates through the waveguide. In the same paper, the authors measured the FSB for different fibers, and demonstrated that the background signal does not depend on the core size but instead increases with an increasing numerical aperture (NA), confirming Myrick's result. Silica fibers with small NAs are therefore the best candidate for the delivery of the excitation light whenever one of the probe design goals is minimizing the fiber background signal.

One simple solution to the silica background issue is the subtraction of the background spectrum from the spectrum of the sample. However, this leads to a considerable reduction of the signal to noise ratio (SNR) of the resulting spectrum. The level of shot noise due to the intense silica background is much greater than that due to the weak signal from the sample, to the point where it can be *as intense* as the signal from the sample for weak Raman scatterers. When the FSB is subtracted from the *useful* spectrum, then the resulting Raman spectrum is affected by the residual shot noise from both the silica and the sample [55]. The use of a hollow-core fiber, be it a simple glass capillary tube coated on

its inner wall or a photonic crystal fiber (PCF) (see Chapter 3), solves the problem of the generation of silica background in a more elegant way: the excitation radiation is transmitted through the air core of the waveguide, and thus gives rise to little or no FSB (except for the weak Raman bands of oxygen and nitrogen) [12, 64].

3.2.3 Lensed probes

All probe geometries discussed so far are *unfocused*, meaning that as soon as the excitation beam leaves the fiber it begins to spread owing to diffraction, resulting in a lower and lower power density as the distance from the fiber tip increases. As thoroughly discussed by Lewis and Griffiths [55], it is often convenient to incorporate a lens in the probe head. Appropriate lens material and anti-reflection coating for the wavelengths of interest have to be chosen in order to minimize the losses due to absorption and reflection, and it is worth-noting that fluorescence from the lens itself may represent an issue in some applications, especially if the given sample is a poor Raman scatterer. However, there are several advantages related to the integration of a lens in the probe design. From an illumination point of view, a lensed probe provides a focused excitation beam, which improves the probe performances given that the intensity of the generated Raman scattering depends on the intensity of the excitation light (see equation 2.11 on page 13). On the other hand, it has to be remembered that a higher intensity increases the risk of photodegradation of the sample, an issue which might rule out the lensed design for some applications. At the same time, a focused beam decreases the sampling volume. However, since optical fibers only collect the portion of scattered signal within their NA, most often this last drawback does not represent a problem. A lensed tip also allows for a better control of the focusing distance, which in turns means that the probe-to-sample distance can be configured by tailoring the lens parameters. A relatively long focal length also allows for the integration in the system of a window or sheath meant for protection of the device. As for the signal collection, instead, the incorporation of a lens on a multi-fiber probe head minimizes the effect of the poor overlap between illumination and collection light cones and therefore of the dead volume, allowing for the employment of such a probe in direct contact applications, especially when dealing with solid samples. In particular, in a geometry like the one first introduced by Carrabba and Rauh [54], the combination of a focusing lens with a (bulk) dichroic component allows for the complete geometrical overlap of the light cones, in spite of the double-fiber probe

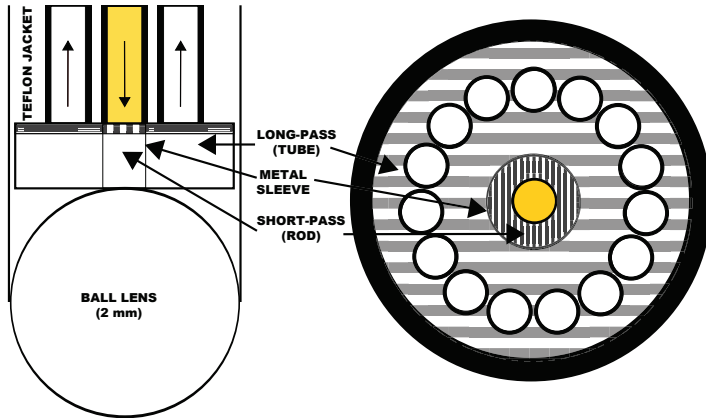


Figure 3.6: Schematic of the lensed and externally filtered probe designed by Motz et al. (adapted from [14]). Longitudinal view on the left, and transverse cross-section at the fiber-filter interface on the right. The diameter of the ball lens, in contact with the filter module, is 2mm. The metal sleeve surrounding the rod isolates it from the tube, thus preventing crosstalk.

structure.

Despite the unquestionable advantages related to the use of a lensed probe head, the work presented in the next chapters of this Thesis deals with unfocused probes. This is mostly due to the fact that the main results of this Ph.D. project have been achieved with a single-fiber probe, characterized by the overlap of excitation and collection light cones, and already affected by an intense background emission from the fiber. The introduction of an additional spectral background due to the lens (especially any reflection of the laser light and emitted FSB back into the waveguide) would have complicated the detection of the Raman signal from the samples. Even more important, as explained in Chapter 1, the probe designs resulting from the work here presented are meant for real-time monitoring of living cells, thus an unfocused probe represents a *safer* option, avoiding any photodamage of the sample.

3.2.4 Externally filtered probes

As previously mentioned, *externally filtered* is the denomination given to those probes whose head incorporates additional filtering optics, often directly mounted on the fiber tip. Generally, lensed probes are also externally filtered. One possibility is the integration in the design of a

dielectric band-pass (BP) or long-pass (LP) interference filter [12]. In particular, Motz et al. [14] used a 15-around-1 bundled geometry with filters realized by 1mm-long coated rods and tubes. One rod carrying a dielectric short-pass (SP) coating on one of its flat surfaces is fitted inside a tube coated with LP coating, and the assembly is then mounted at the distal end of the fiber, so that the first filter takes care of removing the FSB generated along the central excitation fiber, while the surrounding filter acts as a Rayleigh-rejection filter for the collection fibers (see Fig. 3.6). The design presented in [14] also includes a ball lens, which transforms the large angular distribution of scattered light emerging from the sample into a beam that falls within the NA of the collection fibers.

It is worth noting that all these externally filtered probes are meant for a single excitation wavelength, since a change in the laser wavelength requires a different filter. It is therefore not possible to use them together with tunable lasers. Moreover, the performances of such filters may become quite poor in case a high-NA fiber is used.

An alternative to the incorporation in the device of the external filtering optics is the realization of the filters *in-fiber*. An example of an in-fiber Rayleigh-rejection filter is given in Chapter 4.

3.3 Summary

This chapter provides a general introduction to Raman probes, highlighting the main functions required to perform Raman spectroscopy and therefore providing a practical definition of a Raman probe as a device which interfaces the light source with the sample and the sample with the detector. A brief overview of fiber probe geometries operating in a 180° degree configuration is given, and the main advantages and drawbacks of single- and multi-fiber devices are discussed. A comment on the convenience of incorporating a lens in the probe head and of the reason why this solution has not been implemented in the work presented in this Thesis closes the chapter, together with a note on the integration of dielectric filters in the probe design.

Chapter 4

Tunable all-in-fiber Rayleigh-rejection filter for Raman spectroscopy

Above all, don't fear difficult moments.
The best comes from them.

Rita Levi-Montalcini

The previous chapter presents an overview of various fiber Raman probe implementations, highlighting the advantages and disadvantages of the different options. A dual-fiber probe, the simplest example of multi-fiber solution, is considered in this chapter. In order to remove the elastically-scattered light, a low-loss, tunable Rayleigh-rejection filter based on a photonic crystal fiber (PCF) infiltrated by a high-index material is realized.

A brief introduction to PCFs is given in Section 4.2, followed by a description of the filter realization. The spectral characteristic of the filter is compared to that obtained with some finite element method (FEM) simulations. Finally, the results of the application of such a device to a Raman spectroscopy experiment are presented and discussed. The work on the filter is presented in Section 4.3.

4.1 Introduction

Multi-fiber Raman probes are characterized by separated excitation and collection paths. This ensures that the fiber spectral background (FSB) generated along the excitation fiber does not cover the Raman signal collected by the other fiber(s), at least as long as the sample is optically transparent (as explained in Section 3.2 of Chapter 3). This is illustrated in Fig. 4.1, showing the results of an experiment carried out as part of this thesis.

Light from a continuous wave (CW) 532nm diode-pumped solid state (DPSS) laser (Lasever LSR532U) is delivered to a sample of cyclohexane (C_6H_{12} , Merck) through a step-index optical fiber (Thorlabs HI1060). The scattered signal is collected at a 90° angle by means of a commercial fiber Raman probe (InPhotonics RPB Laboratory probe). This device takes care of filtering out the Rayleigh scattering and conveys the inelastically-scattered light to the spectrometer (Andor SR303i, cooled down to -65°C) through a $200\mu\text{m}$ -wide fiber. The spectrum, acquired over a 3s-long integration time, is minimally affected by the Raman emission from glass (appearing at wavenumbers shorter than 500cm^{-1} , see Fig. 4.1 (b)). This background signal has contributions from the excitation fiber, the collimating and coupling lenses and the glass cuvette in which the sample is contained. Thus, the presence of a filter discriminating against the silica background is not imperative. A Rayleigh-rejection filter, on the other hand, is needed. This is demonstrated by a variation of the previous experiment, schematically illustrated in Fig. 4.2. This experiment shows that the intensity of the elastically-scattered light is at least one order of magnitude higher than that of the inelastically-scattered light. The setup, schematically illustrated in Fig. 4.2 (a), involves the delivery of the laser light to the sample through the commercial probe ($105\mu\text{m}$ -wide input fiber) and the collection of the scattering by means of a $105\mu\text{m}$ -core step-index fiber (Thorlabs AFS105/125Y), directly coupled to the spectrometer. The spectrum acquired over a 3s-long integration time is dominated by the Rayleigh line, which saturates the detector as can be seen in Fig. 4.2 (b).

An all-in-fiber implementation of a Rayleigh-rejection filter was first suggested by Pelletier [65] in 1999. It is based on a Bragg grating inscribed in the collection fiber, with a period calculated such that the Bragg peak matches the laser wavelength. The Rayleigh-scattered light is reflected by the grating and does not reach the spectrometer, while the signal undergoes low loss. This solution is limited to single-mode fibers, since

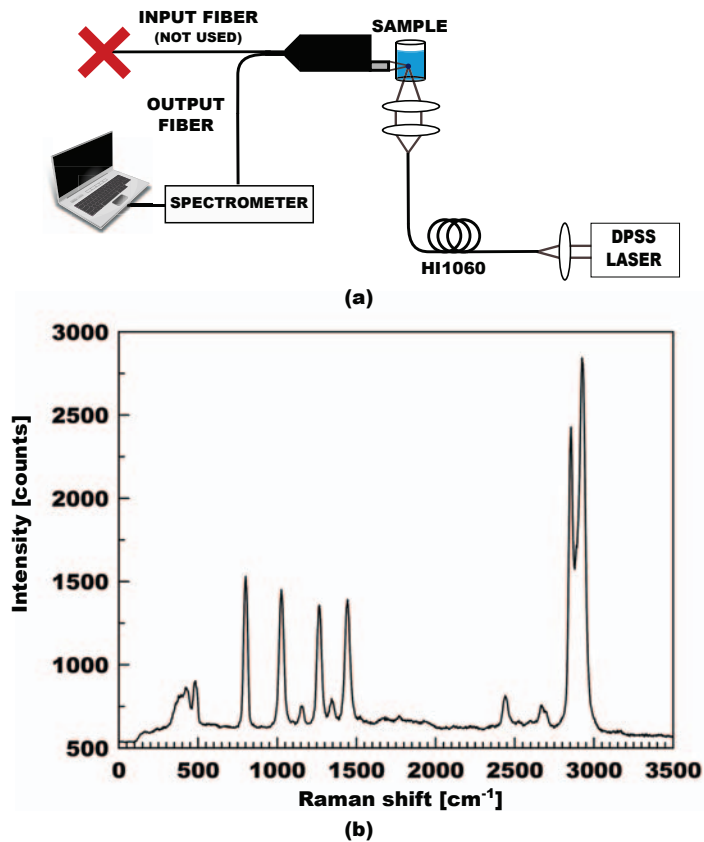
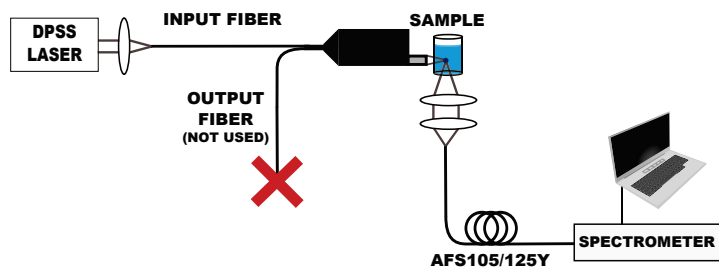
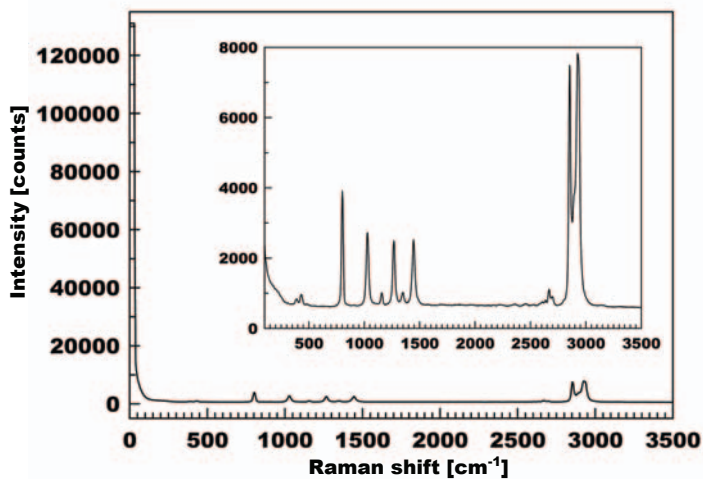


Figure 4.1: (a) Schematic illustration of the experimental setup used to demonstrate the small contribution to the detected Raman spectrum due to FSB in case of multi-fiber probe. The CCD-based spectrometer is equipped with a 600 lines/mm grating. (b) Raman spectrum of cyclohexane, acquired over an integration time of 3s, averaged twice to avoid artifacts. The Raman emission from silica, due to the fiber, the lenses and the glass container, is located at wavenumbers shorter than 500cm^{-1} . The peak at about 2440cm^{-1} is due to room illumination.



(a)



(b)

Figure 4.2: (a) Schematic illustration of the experimental setup used to demonstrate the difference in intensity between Rayleigh and Raman scattering. The CCD-based spectrometer is equipped with a 600 lines/mm grating. (b) Raman spectrum of cyclohexane, acquired over an integration time of 3s, averaged twice to avoid artifacts. Inset: detail of the Raman peaks of cyclohexane.

Bragg gratings in multi-mode fibers require a range of grating spacings which, in turn, translates into a broader reflection bandwidth. fiber Bragg grating (FBG) technology allows for some limited tunability, required whenever multiple excitation wavelengths are used. Such filters are usually tuned either thermally or mechanically [66, 67], or by applying an external electric field [68]. Though mechanical tuning is more efficient, it is also rather cumbersome to implement and therefore not always applicable to a compact Raman probe (see also [69]).

PCFs, i.e. waveguides characterized by a periodic distribution of air holes in the cladding region which runs all along the fiber axis, are good candidates for the in-fiber implementation of a Rayleigh-rejection filter. With respect to standard optical fibers, PCFs exhibit unique transmission properties, and when operating by the so-called photonic bandgap (PBG) effect they allow for the realization of spectral filters. Additionally, the spectral behaviour of these fibers can be tuned by infiltrating their holes with a material whose optical properties can be controlled by, for instance, a change in the temperature or the application of an external electric field.

4.2 Photonic crystal fibers

The confining properties of PCFs are to some degree derived from those of photonic crystals (Yablonovitch [70] and John [71], 1987), i.e. structures characterized by a periodic modulation of the refractive index on the scale of the optical wavelength. This allows the propagation of light for certain spectral bands, while the propagation of others is not allowed. The frequency intervals where no field solution exists are termed photonic *bandgaps*, from which the name of photonic bandgap (PBG) effect originates. In particular, the intuition behind the invention of PCFs is that a defect introduced in the otherwise perfectly regular pattern of a 2D photonic crystal acts like a “trap” for all those wavelengths which cannot propagate through the surrounding plane structure. Thus, by extending this structure along the third dimension, it is possible to obtain a fiber-like behaviour, where the “trapped” wavelengths are guided along the central defect which therefore acts as a core, while all the others “escape” through the encircling microstructure (cladding). In the case of PCFs the two-dimensional periodic structure is provided by an array of air holes in the cladding region, and the structural defect is generally realized by either omitting a number of them or by adding some extra ones. Thus, these waveguides are realized by means of a single

material, without the need for any dopant.

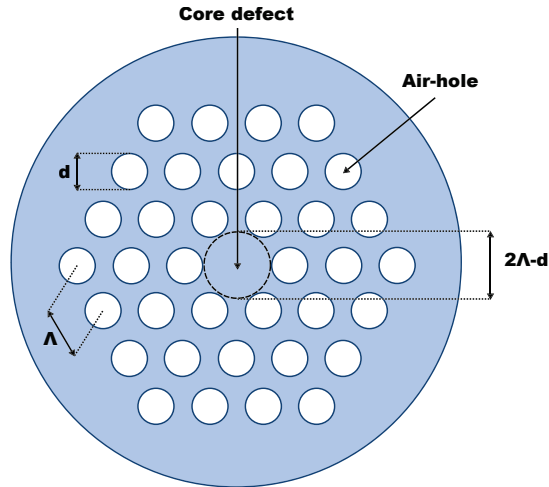


Figure 4.3: Schematic illustration of the cross-section of a typical solid-core PCF, where the core is realized by omitting a single air hole. The core diameter is often defined as $2\Lambda - d$.

The properties of PCFs are normally described through geometrical parameters such as the hole size d , the inter-hole distance (*pitch*) Λ and their ratio d/Λ (*relative hole size*), as well as by the distribution of air holes and cladding diameter D . Fig. 4.3 shows the schematic illustration of the cross-section of a solid-core PCF with triangular lattice, for which the core is formed by omitting a central air hole.

Not all PCFs guide light by the PBG effect. As a matter of fact, the first fiber with a photonic crystal cladding ever demonstrated (Knight et al. [72], 1996), operates by a principle similar to that responsible for light guidance in standard optical fibers, and therefore named modified total internal reflection (M-TIR). For this reason, this class of PCFs is referred to as index-guiding fibers. The first real PBG fiber was demonstrated two years later, always by Knight et al. [73]. Fig. 4.4 shows an example of an index-guiding fiber and of a PBG fiber.

4.2.1 Index-guiding fibers

Index-guiding PCFs guide light in a core that is generally solid. As in standard fibers, the core has a higher refractive index than the average refractive index of the cladding, defined by the air holes and the fiber material. The effective index of the guided modes lies between

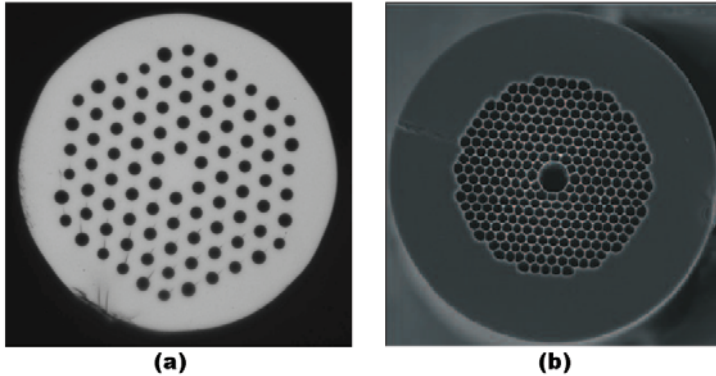


Figure 4.4: Examples of (a) index-guiding and (b) PBG PCFs. In particular, (a) optical micrograph of the end facet of a Large Mode Area (LMA) fiber (NKT Photonics LMA-15, $d = 5\mu\text{m}$, $\Lambda = 10\mu\text{m}$); (b) SEM picture of the end facet of a HC fiber (NKT Photonics HC-1550, core diameter = $10.9\mu\text{m}$, $\Lambda = 3.8\mu\text{m}$). Both pictures appear courtesy of NKT Photonics A/S.

the refractive index of the core and the average refractive index of the cladding. However, this class of PCFs also exhibits novel properties, such as the *endlessly single-mode* behaviour, obtained for a relative hole size d/Λ smaller than 0.4 [74]. In particular, this can be intuitively understood by considering the periodic structure as a modal “sieve”, where the holes represent the “wire mesh” and the glass regions in between them are pathways through which higher order modes can leak away. The fundamental mode is instead “trapped” in the core, owing to its larger lobe. If the ratio d/Λ is increased over 0.4, however, the glass gaps between the holes become narrower and more higher order modes end up being trapped in the sieve [75].

4.2.2 Photonic bandgap fibers

PBG fibers guide light in a low-index core by the PBG effect. Only modes within certain spectral windows, determined by the geometry of the periodic structure, can be guided. This is due to the fact that the cladding of a PBG fiber supports a *discrete* set of optical modes, to which the light in the core can couple. Owing to the discrete nature of the cladding modes, this can only happen at certain wavelengths.

Intuitively, the formation of these *bands* of cladding modes can be explained by observing that the microstructured cladding region of a PBG

fiber, for instance the one from Fig. 4.4 (b), is formed by a large number of silica strands. Each strand supports many distinct optical modes, each with a different value of propagation constant β . Due to the close proximity of the strands, modes with a similar β couple together forming bands of cladding modes (each covering a range of β values) separated by bandgaps. Whenever the propagation constant of the core mode matches the β values of the cladding modes, light “escapes” through the microstructure.

4.2.3 Liquid-filled photonic bandgap fibers

Whenever the holes of an index-guiding PCF are infiltrated by a liquid with a higher refractive index than silica, the core becomes a low-index region within a lattice of high-index rods separated by silica strands. The guidance mechanism changes from M-TIR to PBG, and for this reason these structures are named liquid-filled PBG fibers [76]. PBG guiding is based on a discretization of cladding modes, which in this case is caused by the high-index rods. Surrounded by silica, these rods behave as individual index-guiding waveguides, whose modes couple to form bands of *nearly degenerate* LP_{01} , LP_{11} and LP_{21} modes, i.e. modes with approximately the same refractive index. These bands are separated by bandgaps, as shown in Fig. 4.5. The core of the PCF supports a mode falling in between these bands and having an effective index lower than silica [77]. In particular, this last condition ensures that the core mode is oscillatory and that cladding modes are exponentially decaying on the plane transversal to the axis of the waveguide. This is the analogous of $n_{co} > n_{eff,co} > n_{cl}$ in standard step-index fibers, where $n_{eff,co}$ is the effective index of the mode guided along the core, and n_{co} and n_{cl} are the indices of core and cladding, respectively. The core mode cannot couple to the cladding modes owing to the difference in the effective indices. At wavelengths where the effective index of the cladding modes crosses the silica line the structure becomes transparent, thus no guidance is possible in the core anymore and minima appear in the transmission spectrum of the fiber.

Fig. 4.5 shows the bands of coupled LP_{01} , LP_{11} and LP_{21} modes, separated by bandgaps, together with the index of silica and that of the PBG mode. The simulations were performed by means of a freely available tool based on plane wave expansion method (MIT Photonic Bands), and refer to a structure characterized by a hole size $d = 3.45\mu\text{m}$ and a pitch $\Lambda = 7.15\mu\text{m}$. The filling material is isotropic with a refractive index of

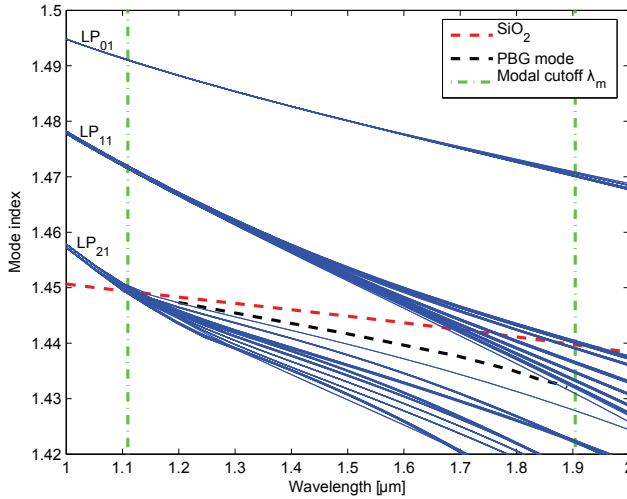


Figure 4.5: Simulated effective mode indices of the cladding modes (blue) and core mode (black) of a liquid-filled PBG fiber. Cut-off wavelengths (green) are calculated by means of Eq. 4.1. Also shown, the refractive index of silica (red). Picture appears courtesy of Lara Scolari [78].

1.5 [78].

The spectral characteristics of a liquid-filled PBG fiber have been extensively studied by (among others) Litchinitser et al. [79–82]. They derived a model which relates the transmission properties of the fiber to those of the high-index inclusions, namely the refractive index of the filling material and the hole size d . In particular, the wavelengths at which transmission minima appear can be estimated from the cut-off condition

$$\lambda_m = \frac{2d\sqrt{n_2^2 - n_1^2}}{m + 1/2} \quad (4.1)$$

where λ_m is the cut-off wavelength of the m -th mode and n_1 and n_2 are the isotropic indices of the background material (silica) and the liquid infiltrated in the fiber respectively.

Eq. 4.1 also shows that by changing the refractive index n_2 of the filling material the position of transmission minima can be tuned. Tunable devices based on infiltrated PBG fibers have been demonstrated by means of both isotropic (for example, [83]) and anisotropic materials ([78, 84–86], among others).

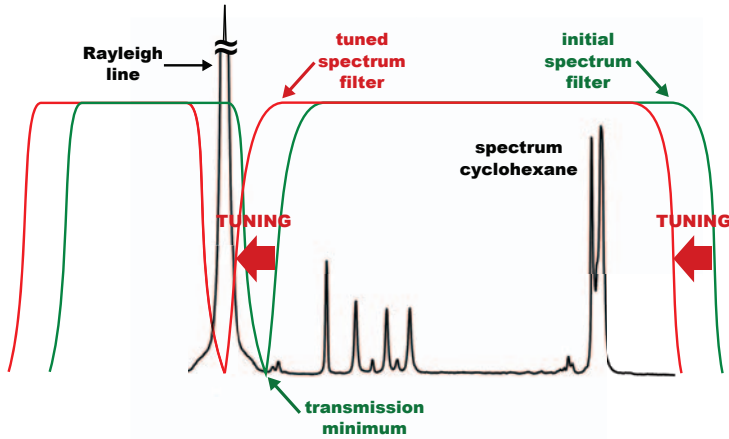


Figure 4.6: Schematic illustration of the realization of a Rayleigh-rejection filter by means of a solid-core PCF infiltrated by a material with a tunable refractive index: the (here simplified) original bandgaps of the filled fiber (green) can be moved (red) such that the position of a transmission minimum matches the Rayleigh line. The Raman spectrum from cyclohexane is shown here as an example.

4.3 Tunable Rayleigh-rejection filter based on high-index liquid-filled photonic bandgap fiber

A liquid-filled PBG fiber exhibits *transmission bandgaps*, i.e. the “forbidden” bandgaps of the surrounding periodic structure, thus behaving as a spectral filter. The shape and width of the bandgaps depend on the particular combination of fiber and filling material. By infiltrating a PCF with a proper tunable material it is possible to obtain a bandgap which is wide enough to be employed as a pass-band filter for the Raman lines of a given sample. At the same time, the spectral position of the bandgap can be adjusted so that a transmission minimum corresponds to the Rayleigh line. In this way the Raman lines reach the spectrometer with low loss, whereas the Rayleigh line is strongly attenuated. A schematic illustration of this procedure is shown in Fig. 4.6.

Being a strong Raman scatterer, cyclohexane is chosen as a test-sample. As shown for example in Fig. 4.1, its bands span a 3000cm^{-1} -wide spectral window, which corresponds to approximately 100nm when using an excitation at 532nm. In particular, the first band is positioned at 801.3cm^{-1} , 23nm away from the Rayleigh line. This requires a rather

wide bandgap with a rather steep edge on the short-wavelength side. Since PBG bandgaps are usually larger at longer wavelengths, a tunability of at least few tens of nm is needed to guarantee that the transmission minimum located on the short-wavelength side of a relatively wide bandgap corresponds to 532nm. Additionally, Raman scattering being a weak process, it is important that the filter be low-loss.

The PCF chosen (NKT Photonics LMA-5), shown in Fig. 4.7, belongs to the class of large mode area (LMA) fibers, i.e. fibers with relatively large dimensions and small effective index contrast in order to spread out the transverse field [78]. The core and outer diameter are 5 and 125 μm respectively, while the hole size d is 1.36 μm and the pitch Λ is 3.16 μm . The numerical aperture (NA) at 532nm is 0.1.

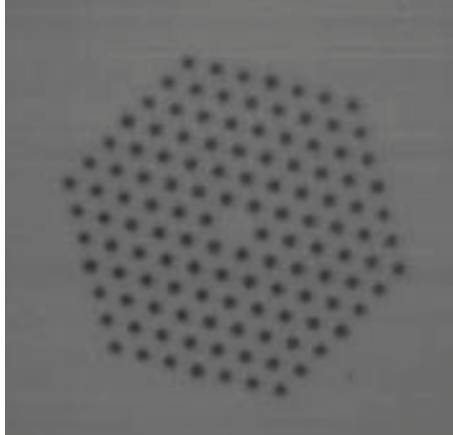


Figure 4.7: Optical micrograph of the LMA-5 used in this work.

4.3.1 Filter realization

At first a transmission spectrum of the *unfilled* fiber is measured. White light from a supercontinuum source (NKT SuperK Compact) is coupled to one end of the PCF, through a single-mode (SM) fiber. The other end of the LMA-5 is coupled to an Optical Spectrum Analyzer (OSA, Ando AQ-6315A) set to a resolution of 2nm. The setup is shown in Fig.4.8. The total length of the fiber is approximately 1m.

The fiber is then infiltrated for 5.5mm of its length with a high-index liquid (Cargille Immersion Liquid 40BN) by capillarity. In order to do so, the tip of the PCF is dipped vertically into a drop of the filling material, poured on a clean glass slide, for 5min. The infiltration length

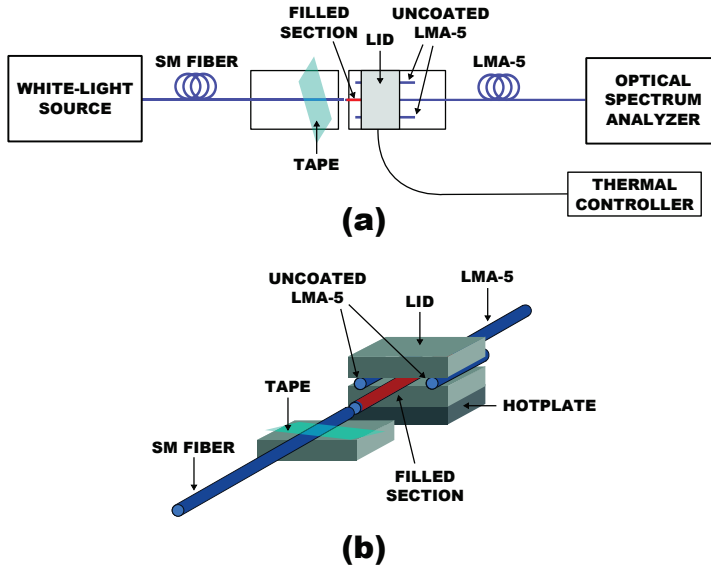


Figure 4.8: (a) Schematic illustration of the setup used to characterize the filter; (b) Detail of the butt-coupling between the SM and LMA-5 fibers: the hotplate connected to the thermal controller is also shown.

was previously determined as a trade-off between the “depth” of the transmission minima and the losses, both of which increase with the filled length. The liquid is characterized by a refractive index $n_{D,25^{\circ}\text{C}} = 1.63$ and by a thermal gradient of $-0.000454 \text{ dn}_D/dT$ (in the range $15\text{--}35^{\circ}\text{C}$). Thus, an increase in the temperature of the filled section of the fiber leads to a decrease of the term n_2^2 appearing in Eq. 4.1, and therefore to a blueshift of the transmission spectrum.

Once filled, the fiber is butt-coupled to the SM fiber which is coupled to the white light source. The infiltrated section is placed between two aluminum blocks, the bottom one in contact with a hotplate connected to a thermal controller (Linkam MC60), the top one acting as a thermal lid. On the sides of the PCF, two uncoated pieces of the same LMA-5 ensure that the lid is placed horizontally without damaging the fiber.

A transmission spectrum is recorded at room temperature (22°C), then the temperature of the infiltrated section is increased to 30°C and up to 70°C in steps of 10°C . At each step, a new spectrum is acquired. The spectra of the filled PCF at 22°C and 70°C , normalized to the spectrum of the unfilled fiber, are shown in Fig. 4.9. At room temperature, the filter exhibits a full width at half maximum (FWHM) bandwidth of 143nm , corresponding to a wavenumber range of $\approx 3549\text{cm}^{-1}$. The relatively flat

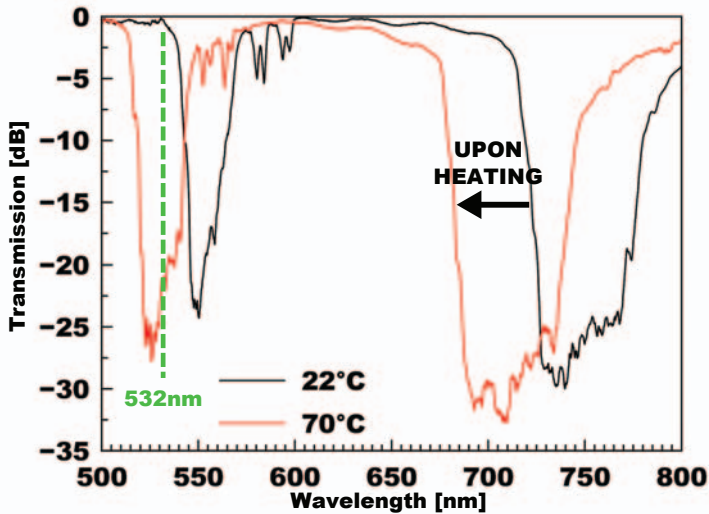


Figure 4.9: Transmission spectrum of the LMA-5 fiber filled with Cargille Immersion Liquid 40BN at 22°C and 70°C. Both spectra are normalized to the spectrum of the unfilled fiber.

bandgap and steep edges are convenient for the realization of a Rayleigh-rejection filter. The device is characterized by an insertion loss of 0.3 dB, measured at the center of the above-mentioned transmission bandgap. However, additional losses due to the ripples at the left-end side of the bandgap are to be expected in the Raman measurements.

A shift of 32nm of the central wavelength of the bandgap is measured when increasing the temperature from 22°C to 70°C. At 70°C, the extinction ratio at 532nm, relative to the centre of the bandgap, is 20.5dB. However, the spectra recorded show that the temperature at which the transmission minimum corresponds to 532nm is in between 60°C and 70°C. This is confirmed by the Raman measurements carried out later, which show a maximum attenuation of the Rayleigh line at about 65°C.

Finite element simulations

A numerical study was carried out to investigate the spectral properties and tunability of the filter. Simulations of the spectra of the infiltrated PCF at room temperature (22°C) and at 70°C are performed by using a self-made vector element-based FEM [85] based on a scheme presented in [87].

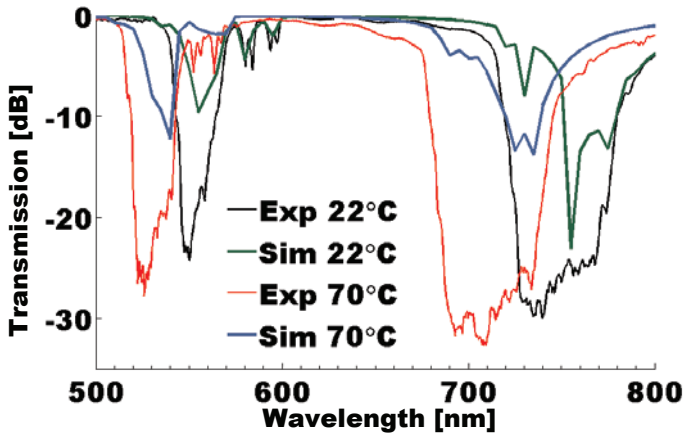


Figure 4.10: Comparison between the simulated and experimental spectra at 22°C and 70°C.

The dispersion of silica was taken into account through the Sellmeier equation [88], while the dispersion of the high-index liquid was calculated by means of Cauchy's equation

$$n(\lambda) = A + \frac{B}{\lambda^2} + \frac{C}{\lambda^4} \quad (4.2)$$

where the wavelength is expressed in Angstrom (\AA) and the coefficients A , B and C are listed in Table 4.1.

A	B	C
1.5955913	985087	7.287217E+12

Table 4.1: Chauchy's coefficients for Immersion Liquid 40BN at room temperature.

The FEM code is used to solve the generalized eigenvalue equation deriving from Maxwell's equations, and the simulated transmission spectra are calculated as the coupling losses due to mode mismatch between the PBG and M-TIR modes at the interface between the filled and unfilled sections of the PCF. This is equivalent to an experimental situation where an infiltrated LMA-5 is coupled to an unfilled one. These losses are calculated using overlap integrals [89]. The propagation losses were not taken into account. The simulated spectra of the device are compared to the experimental ones in Fig. 4.10.

The experimental and simulated spectra are in good agreement. The ripples appearing in the left-end side of the measured bandgap are also

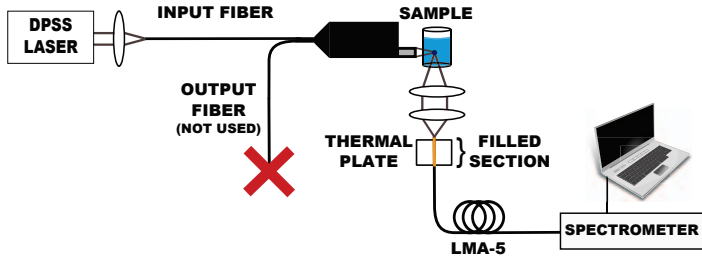


Figure 4.11: Schematic of the setup used in the Raman experiment.

present in the simulated curves. The broader and deeper transmission minima in the experimental curves are due to variations in the hole size along the fiber length, which lead to a broader cut-off since propagation losses are not considered in the model.

4.3.2 Filter application

The infiltrated PCF is then employed to collect the Raman scattering from a sample of cyclohexane, according to the setup illustrated in Fig. 4.11. Continuous wave (CW) light from a 532nm laser (Lasever LSR532U) is guided to the sample through a commercial Raman probe (InPhotonics RPB Laboratory Probe) in order to filter out the spectral background from the delivery fiber. The free-space power at the sample, measured with a powermeter, is 115mW. The scattering is collected orthogonally to the excitation, to avoid direct illumination of the filled PCF, by a collimating lens and then focused into the core of the liquid-filled PBG fiber by means of a second 10X microscope objective. The infiltrated section of the waveguide is “sandwiched” between two aluminum plates as previously explained, with the bottom one in direct contact with the hotplate connected to the thermal controller. A ~ 1 mm-long section of the PCF protrudes from the aluminum blocks. This does not represent a problem, since the meniscus between the bottom surface of the high-index liquid and the inner wall of the fiber capillaries is concave, that is the contact angle is smaller than 90° (see Fig. 4.12). Capillary forces push the liquid inwards, thus emptying the final ≈ 1 mm. The other end of the fiber is coupled to a CCD-based spectrometer (Andor Shamrock 303i), cooled down to -65°C to reduce dark current noise and equipped with a 600lines/mm grating. All measurements are carried out over an integration time of 5s averaged 25 times in order to avoid artifacts in the spectra.

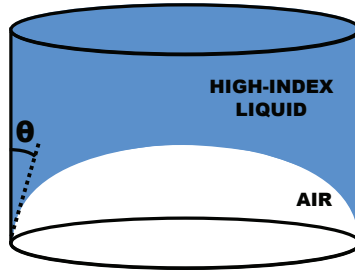


Figure 4.12: Schematic illustration of the concave meniscus between the bottom surface of the high-index liquid used in this work and the inner wall of one of the LMA-5 capillaries. The contact angle, $\Theta < 90^\circ$, is also shown.

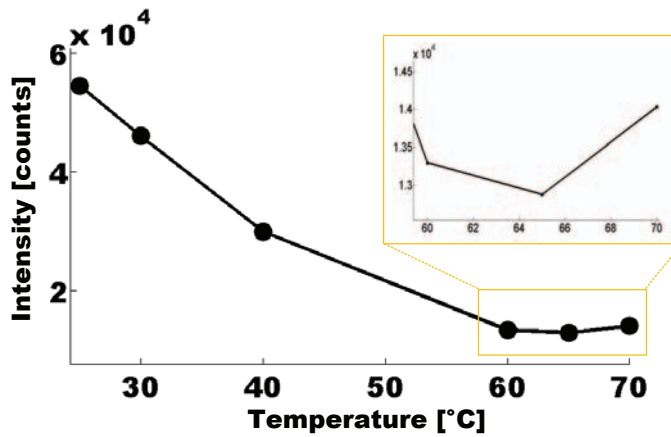


Figure 4.13: Four-fold attenuation of the Rayleigh line as the temperature of the filled section of the fiber is increased from 22°C to 70°C, in steps of 10°C. One additional measurement at 65°C is carried out in order to find the maximum attenuation (shown in the close-up).

The intensity of the Rayleigh line is monitored as the temperature of the filter is increased from 22°C to 30°C, and then up to 70°C in steps of 10°C. The trend measured is plotted in Fig. 4.13. Based on the indication that the maximum attenuation of the Rayleigh line corresponds to a temperature between 60°C and 70°C, an additional measurement at 65°C is carried out. This indeed results in the lowest intensity of the 532nm line, 4.22 times lower than at the starting value of 22°C. The filled section of the PCF is therefore held at 65°C and a Raman spectrum is acquired.

Fig. 4.14 shows the measured peaks, which are in accordance with the values reported in the literature [90], listed in Table 4.2, assuming a

small miscalibration of the spectrometer ($\approx 20\text{cm}^{-1}$). The bands corresponding to the symmetric CH stretching modes of cyclohexane (2852.9 , 2923.8 and 2938.3cm^{-1}) appear here at 2830 , 2902 and 2912cm^{-1} . However, it is worth noting that the difference between, for example, 2830cm^{-1} (measured) and 2852.9cm^{-1} (reference) amounts to less than 1nm , when an excitation of 532nm is considered in Eq. 2.1. As expected, a higher attenuation affects the Raman lines closer to the Rayleigh peak. In fact, the intense peak at 801.3cm^{-1} is not visible in the recorded spectrum. The strong line appearing at about 2420cm^{-1} is due to room illumination, and corresponds to the peak at about 2440cm^{-1} in Fig. 4.1.

Table 4.2: Band parameters of cyclohexane (adapted from [90]). The relative intensity is calculated with respect to the most intense peak (2852.9cm^{-1})

Band parameter	Cyclohexane
Centre [cm^{-1}]	384.1
Relative intensity [%]	2
Centre [cm^{-1}]	426.3
Relative intensity [%]	3
Centre [cm^{-1}]	801.3
Relative intensity [%]	95
Centre [cm^{-1}]	1028.3
Relative intensity [%]	15
Centre [cm^{-1}]	1157.6
Relative intensity [%]	6
Centre [cm^{-1}]	1266.4
Relative intensity [%]	14
Centre [cm^{-1}]	1444.4
Relative intensity [%]	12
Centre [cm^{-1}]	2664.4
Relative intensity [%]	8
Centre [cm^{-1}]	2852.9
Relative intensity [%]	100
Centre [cm^{-1}]	2923.8
Relative intensity [%]	58
Centre [cm^{-1}]	2938.3
Relative intensity [%]	67

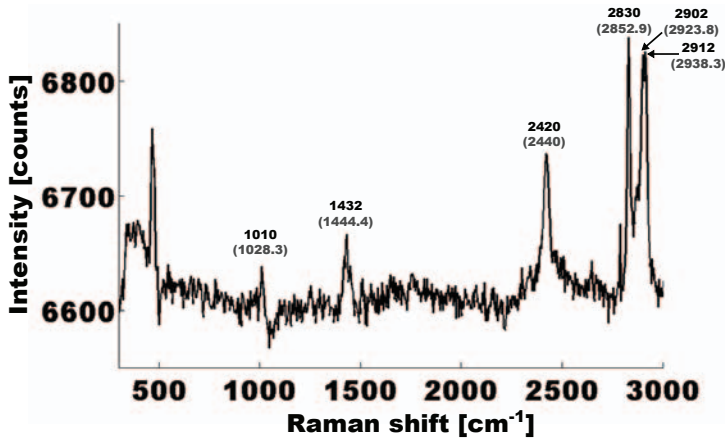


Figure 4.14: Raman spectrum of cyclohexane acquired with the high-index liquid-filled PBG fiber held at 65°C. The acquisition time is set to 5s, repeated 25 times to avoid the appearance of spectral artifacts. Indicated on top of the peaks are the measured Raman shifts (black), compared to those used as a reference (between parentheses), taken from the literature [90]. The line appearing at about 2420cm⁻¹ is due to room illumination.

The discrepancy between the measured insertion loss at 70°C (20.5dB) and the actual four-fold attenuation of the Rayleigh line at 65°C can be explained by considering that the two measurements refer to different setups and in-coupling configurations, and that the former is calculated with respect to the central wavelength of the transmission bandgap rather than the actual transmission value at 532nm.

The attenuation of the Rayleigh line can be improved by increasing the infiltration length of the PCF, at the expense of a higher insertion loss of the device.

A PCF with a higher NA will improve the collection of the Raman signal. However, once infiltrated this fiber has to exhibit a spectrum suitable for the realization of a Rayleigh-rejection filter, with wide and rather flat bandgaps characterized by steep edges.

It is reasonable to expect that a *lensed* tip would adequately replace the (bulk) objective lenses used in this work to focus the collected Raman scattering into the core of the waveguide. This can be done by, for instance, applying a micro-lens on the tip of the fiber.

4.4 Summary

In this chapter a low-loss tunable Rayleigh-rejection filter is presented. The device is based on a LMA-5 PCF infiltrated by a high-index liquid. In order to understand the working principle of such a filter, a brief introduction to PCFs is given. The filter fabrication is described, and the spectral characteristic of the device at 22°C and 70°C are presented and compared to those simulated by means of a FEM code.

Chapter 5

Raman probe based on a double-clad fiber

Now I just work as hard as I can and let the rest fall where it may. It still doesn't feel great most of the time, but I push through it, for the sake of so much good.

Andre K. Agassi

As explained in Chapter 3, single-fiber Raman probes allow for the geometrical overlap of the excitation and collection light cones at the sample. This results in a simpler and more efficient signal collection with respect to multi-fiber probes.

In this chapter, a probe based on a single double-clad fiber is demonstrated. Though the illumination and collection cones of such a waveguide do not overlap exactly, the volume within which Raman scattering is excited is entirely contained in the collection light cone. The probe, described in Section 5.2, allows for the simultaneous excitation and collection of Raman scattering.

5.1 Introduction

“Standard” single-fiber Raman probes (where “standard” means based on a single standard waveguide) are characterized by the geometrical overlap of illumination and collection light cones. This is due to the fact that the counter-propagating excitation and collected light are transmit-

ted simultaneously along the core of the waveguide. As previously discussed in Section 3.2.2 of Chapter 3, this in turn results in a strong fiber spectral background (FSB), which hinders the detection of the Raman signal from the sample, especially those lines located at lower wavenumbers.

However, a physical separation between the light traveling in the two directions within the same waveguide is possible without the need for two independent fibers. A step-index double-clad fiber¹ like the one schematically drawn in Fig. 5.1 provides “independent” paths for the transmission of the laser light to the sample and for the delivery of the collected scattering to the filtering and detection stages. This structure consists of a core surrounded by two circular cladding layers, the inner of which has a higher refractive index than the outer, such that the overall index distribution is $n_{core} > n_{clad,in} > n_{clad,out}$, where $n_{clad,in}$ and $n_{clad,out}$ represent the refractive indices of the inner- and outer-cladding regions respectively. Light can be guided in both the core and inner cladding. In particular, the monochromatic laser radiation propagates in the former, while the scattering is conveyed through the latter. This results in a reduction in the amount of FSB which is delivered to the spectrometer.

It should be noted that part of the Raman emission from the silica core, however, is scattered at an angle that does not satisfy the total internal reflection (TIR) condition at the core-inner cladding interface, and therefore “escapes” to the inner cladding. A small portion of this background signal ends up propagating in this region towards the detector. Thus, strictly speaking it is not correct to assert that the two paths are independent.

Similarly, it is not correct to say that the excitation and collection cone of a double-clad waveguide overlap *completely*, as would instead be the case for a standard (single-clad) fiber. However, in the present case the illumination light cone is completely contained within the collection

¹With respect to some previous work [26], a different terminology is adopted in this Thesis. The term “double-clad” fiber replaces the denomination “double-core” fiber. Owing to the fact that both the core and the inner cladding of this structure are used for light guidance, and to the intuitive association of the concept of light guidance with the core of an optical fiber, the waveguide was initially referred to as double-core. The regions of which the structure consists were then termed inner and outer core, and cladding. However, it was later realized that the name double-core is misleading, since fibers with two non coaxial cores may be called the same way. Additionally, this type of waveguide always appears in the literature under the name of double-clad fiber. For these two reasons, the terminology is here updated to match the conventional one.

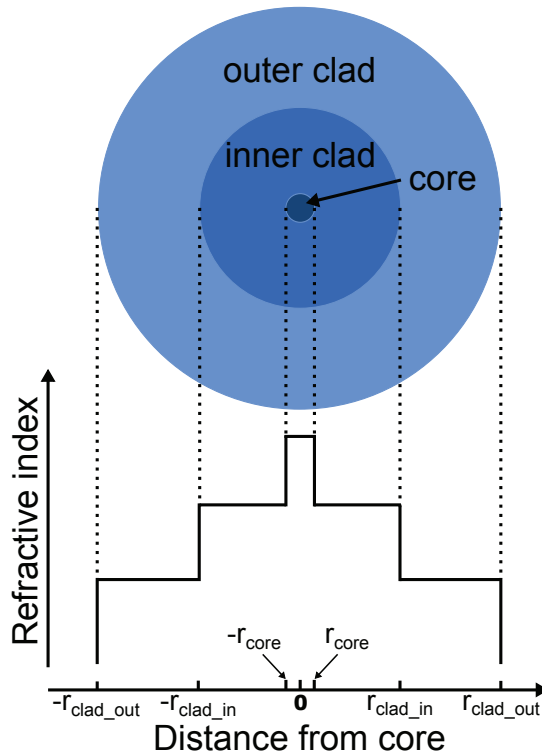


Figure 5.1: Schematic illustration of a double-clad fiber consisting of two circular cladding regions surrounding the core. The step-index structure is characterized by the indicated refractive index profile.

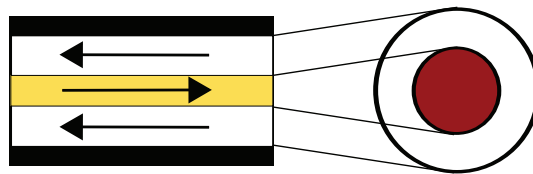


Figure 5.2: Schematic illustration of the overlap of excitation and collection light cones in a double-clad fiber like the one used in this work. Marked in yellow is the “excitation path”, while the region in which the scattering is excited is coloured in dark red.

one, as schematically illustrated in Fig. 5.2. This means that the volume within which Raman scattering is generated is entirely contained in the volume from which the inner cladding can collect light, thus allowing for an efficient collection. It is worth noting though that only the portion of the Raman signal which is scattered in a direction contained within the numerical aperture (NA) of the inner cladding is collected, as indicated

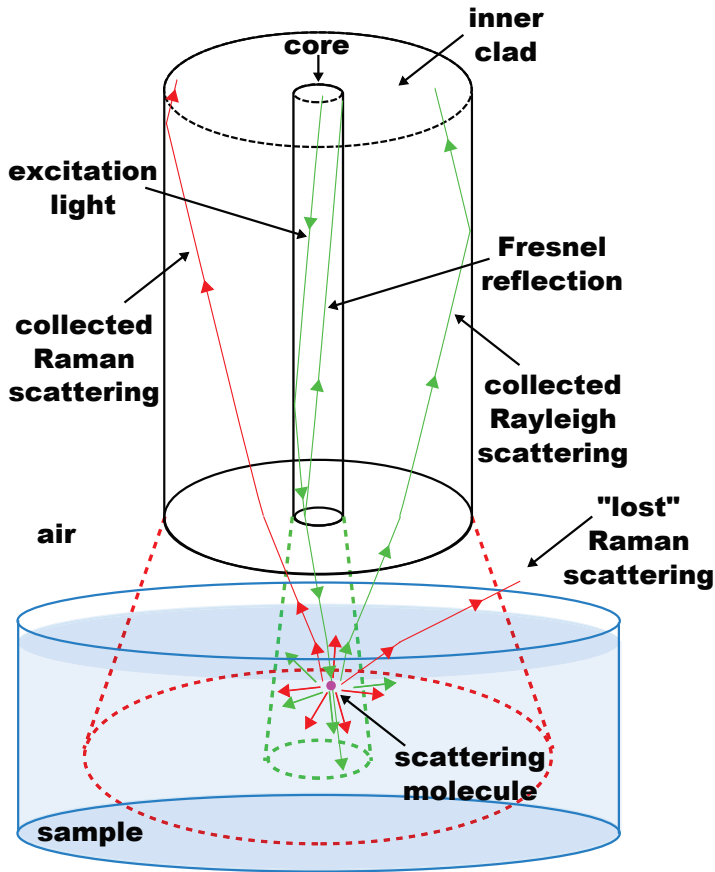


Figure 5.3: Schematic illustration of the excitation and collection of Raman (and Rayleigh) scattering with a double-clad fiber (for simplicity, only the core and inner cladding of the waveguide are shown): the excitation light illuminates the molecules of the sample, one of which is shown as an example, from the core. Part of this radiation, however, is reflected at the fiber/air interface owing to Fresnel reflection and propagates back along the core. Light is scattered in all directions by the sample, and only the fraction which is contained within the collection cone of the inner cladding is actually propagated towards the spectrometer, whereas the rest is “lost”.

in Fig. 5.3.

Double-clad fibers have the ability to support the simultaneous single-mode (SM) illumination from the core and multi-mode (MM) collection through the cladding. This configuration, often termed SM-MM, is convenient in systems which do not require coherent signal detection, such

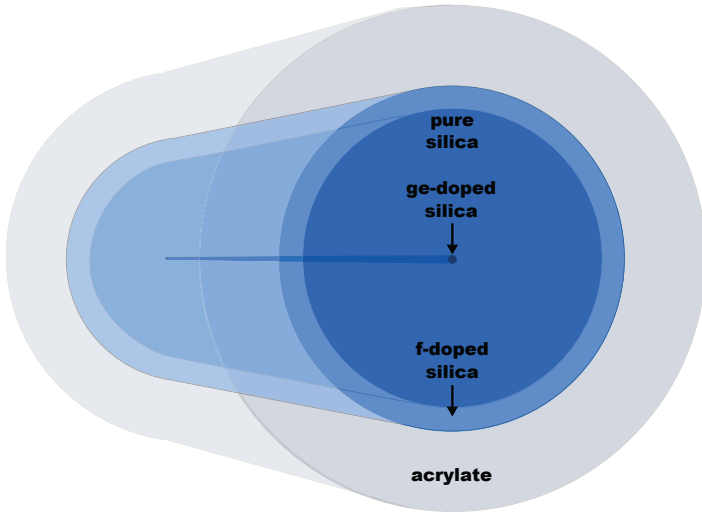


Figure 5.4: Schematic illustration of the double-clad fiber used throughout this work. The core-inner cladding refractive index difference is about 0.005, whereas that between inner and outer cladding is 0.017. The NAs of core and inner cladding are 0.124 and 0.22, respectively.

as Raman and fluorescence detection, owing to the increased collection efficiency (with respect to a single SM fiber) and depth of field (if compared to a single MM fiber) [91].

5.2 Raman probe based on double-clad fiber

The double-clad fiber used throughout this work is schematically shown in Fig. 5.4. It consists of a step-index structure with a central $7.5\mu\text{m}$ diameter germanium-doped core surrounded by a $260\mu\text{m}$ -wide pure-silica inner cladding and by an additional $20\mu\text{m}$ -wide layer of fluorine-doped outer cladding of lower refractive index. The outer fiber diameter is $300\mu\text{m}$, protected by a conventional acrylate primary coating, for a total diameter of $440\mu\text{m}$. The numerical apertures (NAs) of core and inner cladding are 0.124 and 0.22, respectively.

Assuming for simplicity that the end facet of the fiber is homogeneously illuminated by the scattered light, then the collection efficiency is approximately proportional to the area of the collecting region of the fiber. The inner cladding region of this double-cladding fiber collects

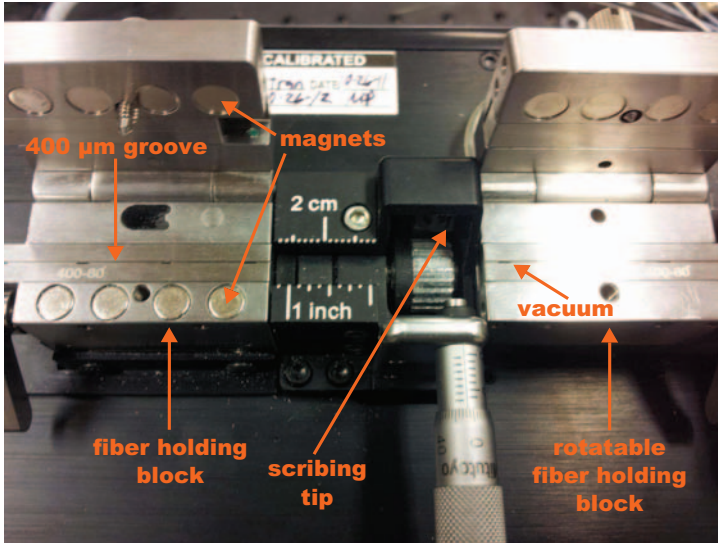


Figure 5.5: Vytran LDC400 Large Diameter Fiber Cleaver. On the walls of the 400 μm V-shaped grooves, small apertures allow for the vacuum pump to “suck” the fiber down. The right fiber holding block can be set to rotate in order to angle-cleave the fiber.

~ 17 times more light than the 62.5 μm -wide core of a single MM fiber with and a similar NA. For a SM fiber with a 8 μm -wide core and a similar NA, this values increases to ~ 1055 times.

5.2.1 Fiber cleaving and mounting

The fiber ends are cleaved by means of Vytran LDC400 Large Diameter Fiber Cleaver (Fig. 5.5). The device operates by the tension-and-scribe method, based on the fact that a crack induced on the side of a tensioned fiber propagates perpendicularly to the applied stress field [92]. This machine allows for the control by the user of both the fiber tension and cleaving angle. The first one is determined for every new type of structure by a trial-and-error procedure, checking the quality of the cleave after each attempt, and modifying the value until a good cleave is obtained. The double-clad fiber used in the work described in this Thesis requires a tension corresponding to a 752g force ($\approx 7.37\text{N}$). The cleaving angle depends on the fiber rotation angle, and previous measurements have shown a good agreement of the two angles, with $\sim 1^\circ$ of difference between them. In the experiment presented in this chapter, the rotation angle is set to 0° (flat cleave) for both fiber ends. Unlike

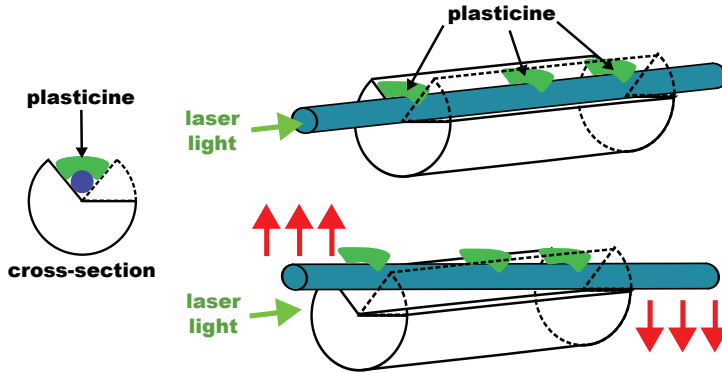


Figure 5.6: Schematic drawing of the placement of a fiber in the fiber mount by means of small pieces of plasticine. The double-clad fiber is too thick to be held in place by means of the sole plasticine, and over a few hours it lifts up on the in-coupling side, spoiling the alignment. In all drawings, a portion of the fiber mount is transparent (contoured by a dashed line) so that the fiber position can be seen. The fiber coating is not shown.

initially believed, the quality of the cleave is not deteriorated if the entire ending section of the fiber is uncoated, despite the fact that the fiber is $140\mu\text{m}$ thinner inside one holding block than in the other.

Once the fiber has been cleaved, it is “mounted” in the setup. However, owing to the thickness of the waveguide, it is not possible to hold it in place on a metallic fiber mount by means of plasticine only, as would instead be the case for a thinner fiber. A standard $125\mu\text{m}$ -diameter fiber can be held in contact with the V-shaped groove of the fiber mount by applying small pieces of plasticine on top of the fiber, as schematically drawn in Fig. 5.6. Unless the termination of the waveguide is entirely stripped from its coating (for as long a section as the length of the mount), the modelling clay has to be applied exclusively on the coated section in order to avoid bendings that would compromise the in-coupling of the laser radiation. The same holds for the double-clad fiber. However, the structure is in this case too rigid for the plastic material to hold it perfectly still, unless the fiber is held horizontally *outside* the V-groove. For this reason, an additional “clamping” stage, shown in Fig. 5.7, is added to the setup. The double-clad waveguide is “sandwiched” between two metal pieces, with a short coated piece of the same fiber on each side to keep the spacing. The stage position is kept loose until the laser light has been coupled into the core, since this in-coupling requires the position of the fiber to be adjusted, also

longitudinally. Once the coupling is done, the stage is fastened to the setup.

5.2.2 Experimental setup

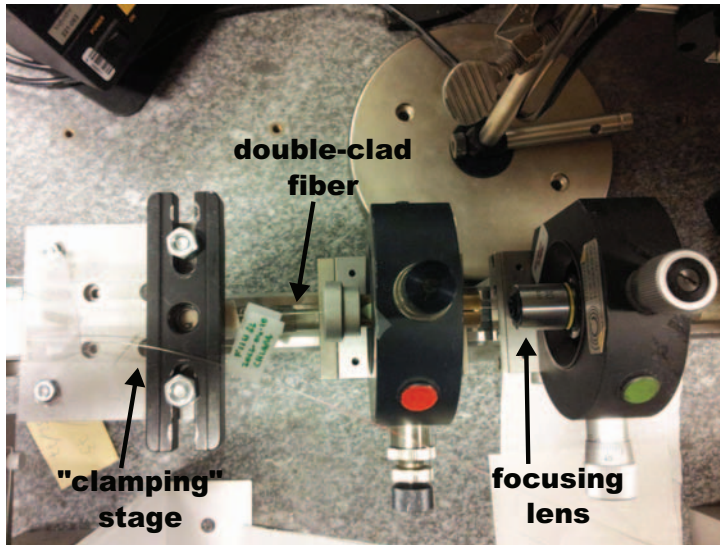
The fiber is used to perform Raman spectroscopy on a sample of cyclohexane (Merck), according to the setup presented in Fig. 5.8. 1064nm light from a Q-switched mode-locked Nd:YAG laser (Quantronix 416) is frequency-doubled by means of a KTP (Potassium Titanyl Phosphate) nonlinear crystal and coupled into the inner core of the double-clad fiber by means of a dichroic mirror and a 10X objective lens (Nikon). Each Q-switched pulse is composed by about 20 mode-locked pulses of the duration of $\approx 150\text{ps}$, generated at a 3.2kHz rate. The fiber was previously cleaved and positioned in the setup as explained in Subsection 5.2.1.

The other end of the double-clad fiber is then put in close proximity to the sample surface (approximately 1mm distance), by means of a self-made holder whose height can be manually adjusted, and in which the fiber mount can be inserted (see Fig. 5.9). The sample is illuminated from the fiber core, whereas the scattering is collected in the inner cladding.

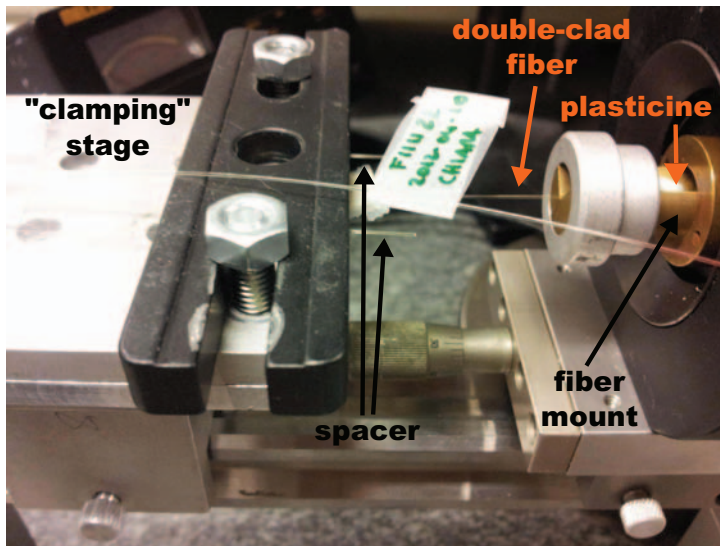
The same dichroic mirror used to couple the frequency-doubled radiation into the core is used to recover the collected scattering from the inner cladding (thus demultiplexing the excitation and Raman signal). A dual 532nm and 1064 nm notch filter (Edmund Optics) eliminates the Rayleigh-scattered light and attenuates the intense infrared (IR) light reflected by the other optical surfaces. Additional filtering of the 1064 nm light is provided by a KG5 glass.

The Raman signal is then focused by a second 10X focusing lens (Nikon) into the inner cladding layer of another piece of the same double-clad fiber. A second “clamping stage” is inserted in the setup to keep the waveguide from moving (Fig. 5.10 (a)). This fiber was previously inserted into a heat-shrink tubing which serves as an extra protective coating. After shrinking this tube, the operation was repeated with a second, larger heat shrink (Fig. 5.10 (b,c)).

The fiber is coupled to a CCD-based spectrometer (QE65000, Ocean Optics), thermo-electrically cooled down to -20°C to reduce dark current noise. The device is equipped with a 1200 lines/mm grating and is capable of signal acquisition in the bandwidth 530 – 697nm. The



(a)



(b)

Figure 5.7: (a) Top view of the in-coupling section: the double-clad fiber is held on the fiber mount by means of plasticine. The additional “clamping” stage ensures that the fiber stays horizontal; (b) The double-clad fiber “sandwiched” between two metal pieces on the additional “clamping stage”. Two pieces of the same fiber, unstripped, keep the spacing. *NOTE: The fiber labeled as “F111122 2012-04-10 CHIARA” belongs to a different setup.*

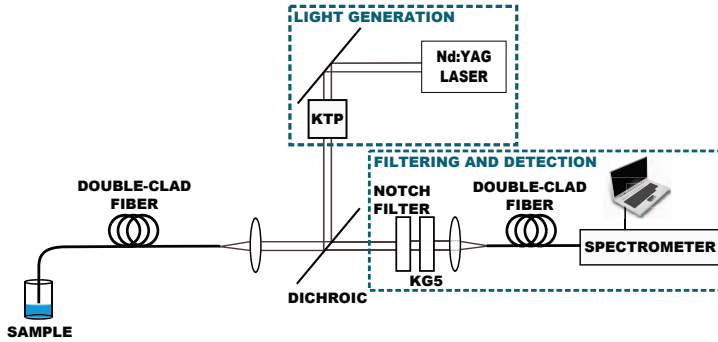


Figure 5.8: Schematic of the experimental setup. The additional “clamping stages” are not shown.

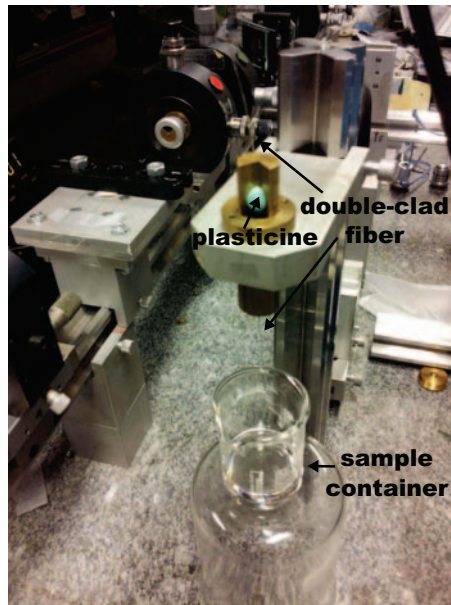


Figure 5.9: Self-made holder, mounted on a “pole” so that its vertical position can be manually adjusted. The fiber mount is inserted in the cylindrical hole, and the whole structure is lowered towards the glass beaker, so that the fiber can be dipped in the sample.

aperture slit of the spectrometer is 1 mm-high and 50 μm -wide, therefore limiting the collection efficiency of the setup. From a geometrical point of view, assuming that the cross-section of the fiber is illuminated homogeneously, then a little less than *one fourth* of the collected light enters the spectrometer ($\sim 23.5\%$). Such a relatively narrow slit width was chosen as a trade-off between the collection area and the spectral

resolution, which degrades as the slit width increases. According to the manufacturer, a $50\mu\text{m}$ -wide slit results in a spectral resolution of $\sim 0.6\text{nm}$. However, a better spectral resolution ($\sim 0.48\text{nm}$) is measured during this experimental activity, as explained in Subsection 5.2.4.

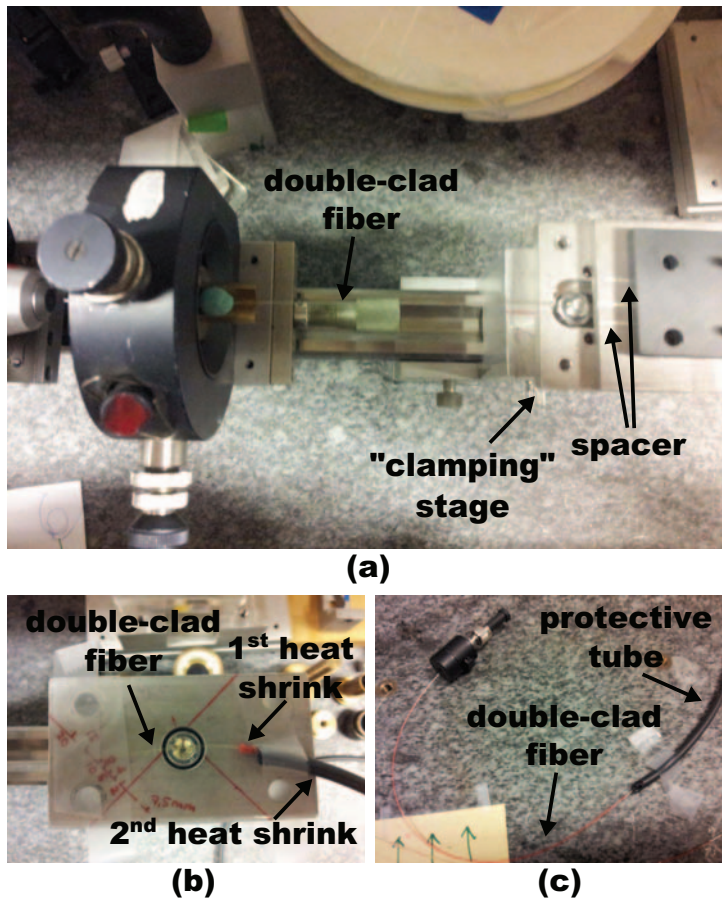


Figure 5.10: (a) Top view of the in-coupling section of the double-clad fiber coupled to the spectrometer: the waveguide is held on the fiber mount by means of plasticine, while an additional “clamping” stage ensures that the fiber stays horizontal. The fiber is “sandwiched” between two metal blocks in between two pieces of the same fiber, unstripped, which keep the spacing; (b) A third stage mounted in the setup to avoid any damage to the fiber, at the section where the latter exits the two heat shrink tubes which provide additional protection; (c) The other end of the double-clad fiber, connectorized, prior to its coupling to the spectrometer.

5.2.3 Self-propelled catastrophic breakdowns

During previous experiments carried out with the tip of the double-clad fiber *dipped into* the sample of cyclohexane, it was found that the radiation exiting the core is capable of causing the nucleation of what are believed to be *cavitation bubbles*, i.e. vapor cavities within the liquid which first expand and then collapse owing to the higher pressure of the surrounding medium (sample). The collapse results in both the emission of a shock wave and the generation of a high-speed liquid jet directed towards the sample/waveguide interface, with potentially damaging consequences for a solid surface placed at a distance shorter than twice the maximum radius of the bubble [93].

As a consequence of the optical cavitation, a fiber fuse is induced in the fiber, that is the self-destruction of the waveguide manifest as a “flash” of visible light which propagates from the original damage site towards the optical source at a speed that can reach several meters per second. Fiber fuses occur at high optical densities (starting from $\sim 2\text{MW cm}^{-2}$) in the presence of a “triggering event”, that is an external stimulus or an inherent flaw in the structure. In this case, the damage caused by the collapse of the cavitation bubble at the sample/waveguide interface may represent the trigger. Another possibility is that the reflection from the bubble (before its collapse) is instead the event triggering the destructive phenomenon. The reflection from the original damaging site increases the temperature in the fiber to $\sim 5400\text{K}$ (5127°C), enough to locally “vaporize” the glass. This results in a new damaging site, which is in turn reflective, leading to the back propagation of the damage [94].

The fiber fuse, observed *every time* the fiber is immersed into a sample of cyclohexane, is a destructive event which requires the replacement of the waveguide. For this reason, the results presented in this chapter are acquired with the tip of the double-clad fiber held outside the sample, at a distance of approximatively 1mm from its surface.

5.2.4 Raman spectra

The Raman spectrum of a sample of cyclohexane, acquired over a 15s-long time (repeated twice), is shown in Fig. 5.11. The solvent is contained in a glass beaker. The Raman lines of cyclohexane from the webpage of McCreery’s group [90], listed in Table 4.2 (Chapter 4), are assumed as reference values and indicated in the figure between parentheses. With respect to the spectrum of cyclohexane acquired with the

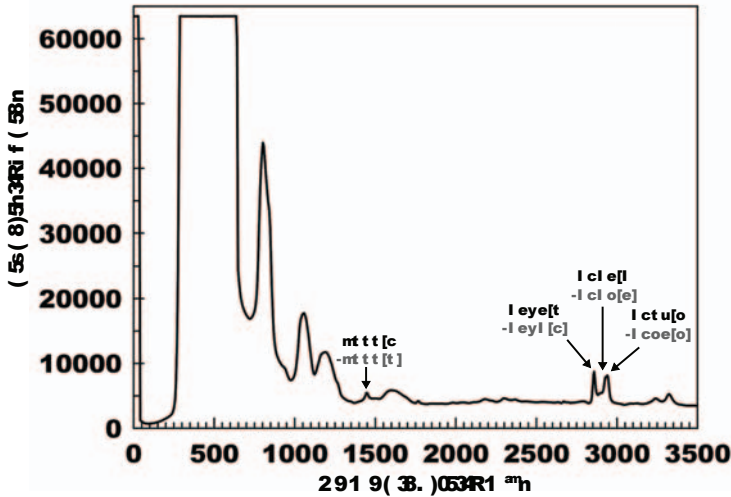


Figure 5.11: Raman spectrum of cyclohexane acquired with the double-clad fiber over an integration time of 15s, repeated twice to avoid the appearance of spectral artifacts. Only the Raman lines located at 1444.9, 2858.4, 2928.2 and 2940.3 cm^{-1} are easily identifiable, whereas the others are masked by the fiber background emission. Indicated on top of the peaks are the measured Raman shifts (black), compared to those used as a reference (between parentheses) [90].

commercial probe from InPhotonics (Fig. 4.1 in Chapter 4), the spectrum recorded with the double-clad fiber is affected by a strong FSB, which covers all the peaks from the sample with the exception of those located at 1444.9, 2858.4, 2928.2 and 2940.3 cm^{-1} . This is due to single-fiber nature of the probe: part of the background signal which is generated in the core by the excitation light is scattered at an angle which does not satisfy the TIR condition, as explained in Section 5.1. The largest contribution to the FSB, however, comes from the fiber emission in the core which is reflected at the fiber/air interface and which propagates back towards the dichroic component along the core itself. Moreover, the 532nm radiation which is reflected at the fiber/air interface ($\sim 4\%$, Fresnel reflection), also contributes to the generation of this interfering signal. The bulk dichroic component used to demultiplex the Raman and laser signals transmits all wavelengths other than 532nm, regardless of their origin (core or inner cladding).

It is worth noting that a strong Rayleigh line still appears in the spectrum, despite the presence of the notch filter. Also, the ability of the spectrometer to discriminate between the peaks at 2928.2 and

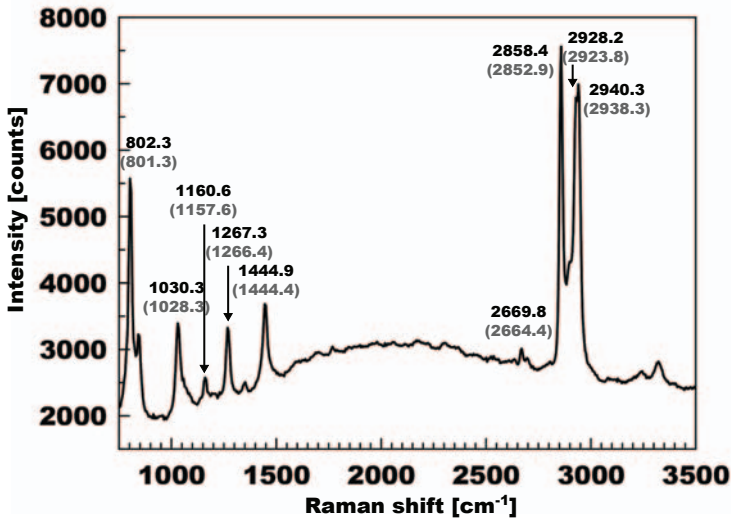


Figure 5.12: Raman spectrum of cyclohexane obtained from the subtraction of the spectrum of the double-core fiber (FSB) from the spectrum of the sample, acquired with the same fiber. Both spectra are recorded over a 15s-long interval, and the acquisition is repeated twice to avoid the appearance of spectral artifacts. Indicated on the peaks are the measured Raman shifts (black), compared to those used as a reference (between parentheses) [90]. Owing to the saturation of the detector for wavenumbers lower than 750cm^{-1} in both the measurements with and without the sample, only the $750 - 3500\text{cm}^{-1}$ range is shown here.

2940.3cm^{-1} proves that the resolution of the device is at least 0.48nm : by means of Equation 2.1 from Chapter 2, it is possible to convert the Raman shifts into the corresponding wavelengths, which in this case turn out to be 630.17nm (2928.2cm^{-1}) and 630.65nm (2940.3cm^{-1}).

In the attempt to obtain a clearer signal, a Raman spectrum of the fiber is also acquired (over the same integration time) and subtracted from the one previously recorded. In particular, the second spectrum is acquired after the removal of the sample from the glass beaker by means of a syringe, with the fiber still in place. The spectrum resulting from the subtraction, shown in Fig. 5.12, is characterized by the presence of *all* the major cyclohexane peaks. It is therefore sufficiently detailed and background-free to be considered useful.

It is worth remembering that this positive result is obtained by means of bulk components, namely the KTP crystal used to frequency-double the laser radiation and the dichroic mirror which recovers the collected

Raman scattering. These have to be replaced by equivalent in-fiber components, in order for a truly all-in-fiber Raman probe to be realized.

The spectral subtraction is only shown in the spectral range $750 - 3500\text{cm}^{-1}$. This is due to the fact that for wavenumbers lower than 750cm^{-1} the background fiber emission saturates the detector in both spectra, thus leading to a difference equal to zero.

5.3 Summary

In this chapter, a Raman probe based on a double-clad fiber is presented. The structure is described, and some experimental issues such as the formation of what are believed to be cavitation bubbles and the occurrence of fiber fuses are briefly discussed. The tool and techniques used to cleave the fiber and properly mount it in the setup are also mentioned. The Raman spectrum of Cyclohexane obtained with this device, together with a short discussion of the experimental results, closes the chapter.

Chapter 6

Raman probes based on optically-poled double-clad fibers

There is no use trying, said Alice; one can't believe impossible things. I dare say you haven't had much practice, said the Queen. When I was your age, I always did it for half an hour a day. Why, sometimes I've believed as many as six impossible things before breakfast.

Lewis Carroll

The work presented in Chapter 5 relates to the demonstration of a Raman probe based on double-clad fiber. The excitation light in the visible range is generated by a nonlinear crystal and injected in the core of the fiber, through which it is delivered to the sample. The scattering (both elastic and inelastic) is collected in the coaxial inner-cladding region of the same waveguide, from which it is recovered by means of a bulk dichroic mirror.

In order to realize an all-in-fiber Raman probe, additional steps are required, with the replacement of all remaining bulk components by equivalent fiber components. In this chapter, the in-fiber generation of the excitation light in the visible range by means of a technique known as optical poling is addressed, together with the possibility to recover the collected scattering using an integrated fiber coupler in the setup.

An introduction to optical poling is given in Section 6.2. This is followed by a description in Section 6.3 of the fabrication of a Raman probe based on an optically-poled double-clad fiber and the discussion of the results obtained with it. The fabrication and characterization of a double-clad fiber coupler is presented in Section 6.4, together with the results of a proof-of-principle Raman spectroscopy experiment carried out with a probe based on an optically-poled double-clad fiber coupler.

6.1 Introduction

Ever since their first demonstration in 1983 [10], substantial improvements in the design of fiber-based Raman probes have been reported, in the attempt to further miniaturize the devices, enhance their collection efficiency and to integrate as many of the required functionalities as possible into fiber components [11, 55–57]. As described in Chapter 3, these functionalities include the generation of the excitation light and its delivery to the sample, as well as the efficient collection and filtering of the Raman-scattered light and its delivery to a suitable detector. In case the excitation and collected signals travel along the same waveguide, then also some signal/pump demultiplexing is needed.

As seen in Chapter 4, an in-fiber Rayleigh-rejection can be realized with the use of photonic crystal fibers (PCFs). The collected elastically-scattered light can be filtered out by means of a PCF infiltrated by a high-index material. By carefully choosing the filling material, a tunable low-loss device can be obtained.

The development of a Raman probe based on a double-clad fiber is discussed in Chapter 5. The device takes care of delivering the excitation light to the sample through its core, and propagating the collected scattering towards the spectrometer in its inner cladding. The demultiplexing between the laser and collected radiation is performed by a bulk dichroic component.

As for the in-fiber generation of the excitation light, a fiber laser represents the obvious choice. The problem lies in the fact that excitation wavelengths in the visible range are usually preferred for Raman spectroscopy, owing to the inverse proportionality between the intensity of the Raman signal and the wavelength used to excite it, while monolithic fiber lasers are generally available in the near infrared (IR). Nonlinear crystals such as KTP (Potassium Titanyl Phosphate) are often used for frequency doubling, at the price of the loss of some of the advantages

of the monolithic design, such as reduced coupling losses, alignment-free operation and increased robustness. However, by poling the fiber used to deliver the excitation light to the sample, it is possible to achieve in-fiber second harmonic generation (SHG), thus preserving the all-fiber design. In this way, a fiber laser emitting a fundamental 1064nm radiation can be complemented with a poled fiber, able to generate the 532nm light of interest.

Of the various poling techniques [95], optical poling is the easiest to implement, requiring neither electrodes internal to the fiber nor a periodic ultraviolet (UV) exposure. This technique relies on the creation of a self-organized grating by means of the coherent interaction between the fundamental IR and the second harmonic (SH) waves along the fiber core. Demonstrated for the first time almost three decades ago and gaining a lot of attention in the first few years, it was soon eclipsed by thermal poling [96], characterized by a higher conversion efficiency. As much as 236 mW of green light have recently been generated in a fiber by thermal poling [97], whereas no more than a few mWs of generated visible light has ever been reported with optical poling [95].

The employment of optical poling in a Raman experiment represents one of the first practical applications of this technique. When used in conjunction with a double-clad fiber, this technique has the additional advantage of avoiding any background fiber emission from the inner cladding due to an imprecise coupling of the laser light to the waveguide (that is, the unavoidable large fraction of the externally generated SH radiation coupled to the inner cladding instead of to the core).

The last bulk optics component that should be replaced in the all-fiber implementation is the dichroic mirror used to recover the scattering from the inner cladding of the fiber. A good candidate is a double-clad fiber coupler, that is a component able to couple the collected scattering between the inner-cladding layers of two pieces of the same double-clad fiber.

During the last decade, double-clad fiber couplers have mainly been used by Lee and coworkers for fluorescence spectroscopy [98, 99], often combined with optical coherence tomography [100]. Lemire-Renaud et al. [101] demonstrated a spectrally encoded endoscopy setup based on a double-clad fiber coupler. These devices were realized by fused biconical taper (FBT) method [99, 101], side-polishing method [98], or by simple contact between the inner-cladding regions of the fibers, after the removal of the low-index polymer layer that serves as an outer cladding [100].

By optically poling one of the waveguides of a double-clad fiber coupler it is possible to obtain an all-in-fiber component which is able to generate the excitation light in the visible range required to perform Raman spectroscopy, deliver the generated radiation to the sample through the fiber core and simultaneously collect the scattering in the inner cladding. Once the backpropagating signal reaches the coupling region, a part couples out to the inner cladding of the other waveguide of the device, which conveys it to a proper filtering stage first, and then to the spectrometer.

Such an optically-poled double-clad fiber coupler-based Raman probe represents a considerable step forward in the realization of an all-fiber Raman system, to be complemented by a fiber laser at 1064 nm and an in-fiber Rayleigh-rejection filter.

6.2 Optical poling

Optical poling is a technique which allows for SHG in optical fibers by recording a permanent periodic grating along the waveguide.

Until the first report¹ of efficient SHG in a conventional glass fiber in 1986 [104], the occurrence of second-order nonlinear processes in silicate fibers was deemed to be impossible owing to the nature of glass. Fused silica is an amorphous material which exhibits a macroscopic space inversion symmetry, thus the lowest expected nonlinearity is the third order. However, by recording an electric field in the glass it is possible to “break” the inherent symmetry and allow for the appearance of second-order nonlinear effects, otherwise prohibited. Optical poling, as the process is now called, induces a permanent modification in silica, which starts behaving like a χ^2 material despite the intrinsic absence of a χ^2 [95, 105].

Though the basic microscopic mechanisms behind optically-induced SHG have never been completely understood, it is known that this process relies on the coherent interaction between the fundamental IR and the SH light. For this reason, a SH “seed” is needed for the phenomenon to start. In the absence of an external seed, it is believed that a weak SH signal is produced anyway by the fiber due to the (normally neglected) electric

¹Weak in-fiber SHG was reported before 1985 by Fujii et al. [102] and Sasaki and Ohmori [103] as a consequence of the combination of four-photon mixing and stimulated Raman scattering (at least in the second case; Fujii and coworkers were not able to fully explain their results.)

quadrupole and magnetic dipole interactions, and this weak signal acts as a seed [105]. The combination of two photons of the fundamental beam with one photon of the SH radiation is believed to result in the photoionization of glass defects, giving rise to a spatially periodic charge ejection. The electrons released in the process drift in the gradient of the optical field until they are trapped at the core-cladding interface, where they accumulate. Altogether, this charge accumulation results in a spatially periodic but temporally invariant (DC) internal electric field, permanently recorded in the fiber [95, 106].

The DC field forms a grating in the fiber, whose period depends on the relative phase of the beating fundamental and SH waves. This grating satisfies a quasi-phase matching (QPM) condition, which guarantees constructive interference and therefore an efficient frequency doubling. As suggested by Armstrong et al. [107], the periodic modulation of the refractive index of the waveguide due to the grating compensates for any difference in the phase velocities of the two waves. Written during the optical poling process, this self-organized QPM grating contributes to its own creation. Thus, the amount of frequency-doubled light at a given time depends on the amount of SH that, together with the fundamental, previously exposed the fiber. Accordingly, the *unseeded* growth² of the generated light is exponential with time [95, 108].

The period of such a grating, which in silicate fibers with a fundamental beam at 1064nm is $\sim 40\mu\text{m}$, can be measured by exposing the optically-poled fiber to chemical attack by hydrofluoric acid and by inspecting it under a phase-contrast microscope, as shown in Fig. 6.1. This is due to the fact that the rate of etching is sensitive to the intensity of the internal electric field recorded in the fiber [109].

After a given amount of time, the poling process saturates. It is now believed that the dark conductivity of the glass, which limits the amount of charge that can be accumulated, contributes to the saturation [106]. Also, it is known that frequency doubling occurs further and further into the fiber as the preparation evolves, but close to saturation the generating region reverses its movement and retreats towards the input of the fiber. This suggests that after a length of about 10cm, that is the typical final length of the grating, the coherent interaction of the two fundamental and SH waves is lost. It is reasonable to think that dispersion plays a role in disturbing the QPM regime, as well as other nonlinear phenomena such as self- and cross-phase modulation, which

²The term “unseeded” here refers to the growth of the SH light after the removal of the seed.

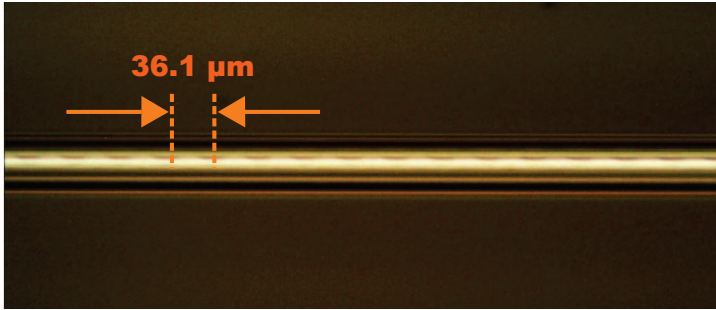


Figure 6.1: Germanosilicate fiber prepared for SHG by optical poling, etched with hydrofluoric acid (HF). The image is obtained with a phase-contrast microscope. Picture appears courtesy of Walter Margulis.

alter the relative phase of the waves [105, 110]. The strength of the recorded field is usually in the order of 10^6Vm^{-1} , about four orders of magnitude weaker than the inter-atomic field.

Optical poling is a stable process: once poled, the fiber can be removed from the setup and when exposed to light again it is still able to frequency-double efficiently the same IR wavelength used during the preparation (where “the same” here means a wavelength within a bandwidth in the order of a few Å from that originally employed in the preparation). Such an experiment is not straightforward, though: not only the wavelength has to match the one used in the preparation process to satisfy the constructed interference condition, but also the polarization of the illuminating radiation has to match the one used to pole the waveguide. This is not easy to accomplish if the fiber is not polarization maintaining (PM). In such a case, the fiber should not be bent and the temperature in the room should be fairly constant, since even a few °C temperature variation affects the polarization of the light propagating in the waveguide. In case an orthogonal polarization is used, the DC field will be three times weaker, and the generated SH *nine* times less intense. This issue can be overcome by using a PM fiber.

6.3 Raman probe based on an optically-poled double-clad fiber

The probe is fabricated by means of a double-clad fiber like the one illustrated in Figs. 5.4 and 6.2. Prior to its preparation for SHG, the fiber is hydrogen-loaded for about 1 week at a pressure of 145bar and at

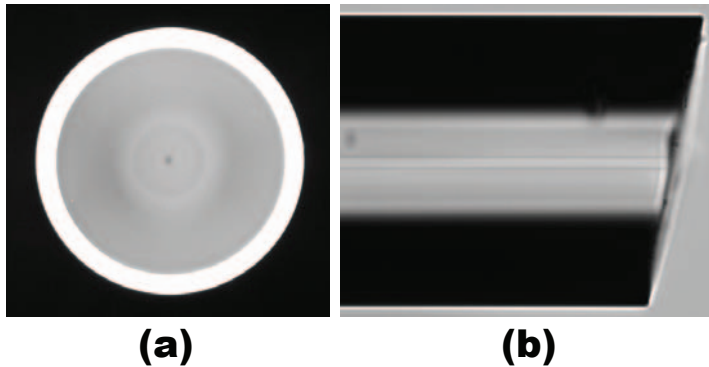


Figure 6.2: (a) Cross-section of the cleaved double-clad fiber; (b) Angle-cleaved tip (about 11°) on the sample side of the probe. The circular region of a lighter colour surrounding the core does not represent an interface between two different materials, but is instead due to the “caning” procedure during the fiber drawing process.

room temperature, and then stored in a freezer at -78°C to prevent any outdiffusion of the hydrogen. The hydrogen loading of Ge-doped silicate fibers at high pressure and low temperature is known to enhance the photosensitivity of the waveguides in the UV range, and for this reason is a technique commonly used in grating formation [111]. However, H_2 loading also enhances the efficiency of the optical poling process at 1064nm, accelerating the preparation of a fiber for SHG [112, 113].

The H_2 -loaded double-clad fiber is cleaved with Vytran LDC400 (see Subsection 5.2.1 of Chapter 5). In particular, one end is flat-cleaved, while the other is cleaved at an angle of about 11° (corresponding to a rotation angle set to 10°), in order to reduce the Fresnel reflection at the glass/sample interface. Fig. 6.2 shows an optical micrograph of the cleaved sections.

6.3.1 Optical poling of the double-clad fiber

The preparation of the double-clad fiber for SHG follows the three steps illustrated in Fig. 6.3. At first, 1064 nm light from a Q-switched mode-locked Nd:YAG laser (Quantronix 416) is frequency-doubled by means of a KTP crystal in order to generate the seed for the process. Each Q-switched pulse is composed by about 20 mode-locked pulses of the duration of $\approx 150\text{ps}$, generated at a 3.2kHz rate. Both the fundamental IR light and the SH are coupled into the core of the fiber by means of

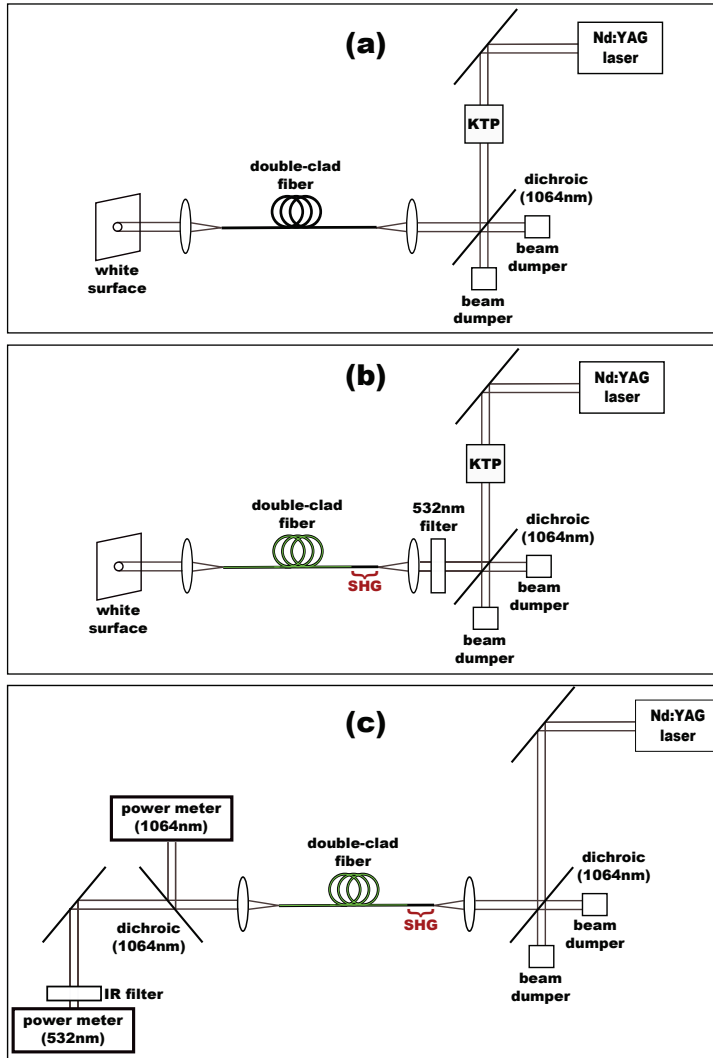


Figure 6.3: Steps needed for the optical poling of the double-clad fiber: (a) seeding of the SH light by means of a KTP crystal; (b) reading of the 532nm generated by the fiber; (c) self-sustained preparation, monitored by two power meters at 532nm and 1064nm respectively.

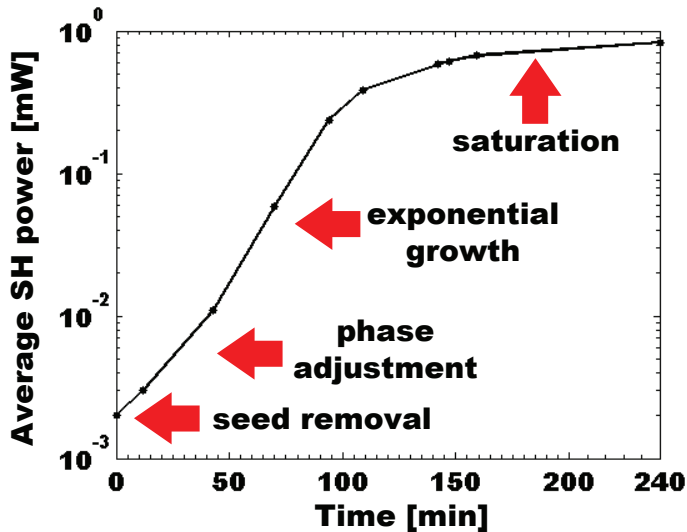


Figure 6.4: Growth of the SH with time, measured after the focusing lens and an additional filter to attenuate the IR radiation.

a dichroic mirror and a 10x focusing lens (Nikon). Although the mirror is highly reflective at 1064nm, a small amount of green light is also reflected. Since this is the same component that will later be used to demultiplex the core and inner-cladding radiation in the actual Raman experiment (see Subsection 6.3.2), it is important that the amount of reflected visible light is small. An additional mechanical “clamping” stage like the one described in Section 5.2 of Chapter 5 is placed in the setup to ensure the correct positioning of the fiber.

The in-coupling of the light to the core mode is done by near-field imaging the shape of the mode exiting the fiber on a white surface placed at a distance of about 1m from the tip of the waveguide, by means of a 20X collimating lens (Nikon) (Fig. 6.3 (a)). The 1064nm beam is coupled to the fundamental mode in order to guarantee efficient SHG. This is a bit unpractical since it requires an IR viewer. However, it is found that if the visible light from the seed is coupled to the core mode first, then finding the optimized coupling condition for the IR radiation is rather straightforward. Thus, for the sake of convenience, the coupling of the SH is optimized first.

After a few seconds of illumination with both green and IR radiation, the fiber core starts generating SH light. By inserting in the setup a filter which blocks the injection of the 532nm radiation into the waveguide, it

is possible to check whether or not there is any green light in the exit beam (Fig. 6.3 (b)). Once the optical poling process has started, then the nonlinear crystal is removed and the growth of the SH continues as a self-sustained process. Two power meters measure the average power of the generating and generated radiation, as shown in Fig. 6.3 (c).

Saturation occurs in about 4 hours, with approx 0.83 mW average power of generated green light (measured after the collimating lens and a filter attenuating the IR transmission), out of the average 450 mW of IR light initially injected into it. The generated power at the output of the fiber is estimated to be about 1mW. As expected, after an initial adjustment of the relative phase of the fundamental and SH waves which follows the removal of the seed, the unseeded growth of the SH is exponential with time, as shown on a semi-logarithmic scale in Fig. 6.4.

Optical poling takes place along the first $\sim 10 \div 20$ cm from the fiber input. Thus, in case the distal end is damaged, it can be cleaved again without consequence for the generated SH.

6.3.2 Experimental setup

In an effort to solve the issue of bubbles and fiber fuses, described in Section 5.2 of Chapter 5, other samples are tested. It is found that measurements carried out on samples of dimethyl sulfoxide (DMSO) are not affected by bubbles, unlike those performed on cyclohexane, ethanol and methanol. It is therefore possible to dip the tip of the double-clad fiber into DMSO without risking to damage the waveguide. This might be due to the different vapor pressure of the solvents, rather than on their polarity as initially thought. According to Shah et al. [114], induction of cavitation is more difficult in solvents with low vapor pressure. DMSO has the lowest vapor pressure among all the above-mentioned materials (0.61hPa versus 104hPa for cyclohexane, 59hPa for ethanol and 128hPa for methanol, all of which refer to a temperature of 20°C with the exception of DMSO, whose vapor pressure is given at 25°C [115]), which might explain the different behaviour. Being also a strong Raman scatterer, DMSO is therefore used as a sample for the experimental activity described here.

The 532 nm light generated by the optical poling of the double-clad fiber is used to perform Raman spectroscopy on a sample of DMSO (Merck), according to the setup shown in Fig. 6.5. In particular, the solvent is illuminated by the light exiting the core of the waveguide and the

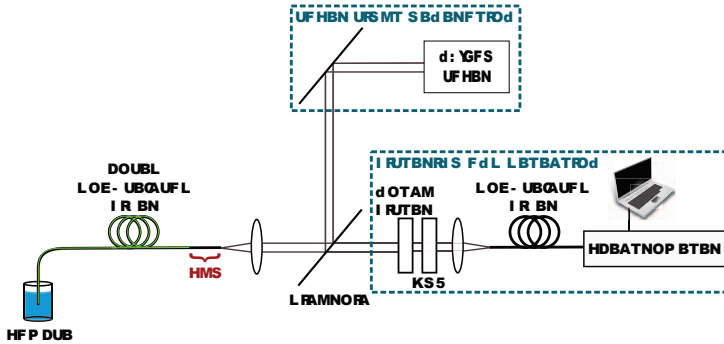


Figure 6.5: Schematic of the experimental setup. Additional “clamping” stages (not shown here) are placed in the setup to ensure the correct positioning of the fibers.

Raman-scattered light is collected in the inner cladding. The waveguide is inserted vertically into the sample by means of a holder like the one shown in Fig. 5.9.

The same dichroic mirror used to couple the laser radiation into the core is used to demultiplex the excitation light from the scattering, in order to recover the latter from the inner cladding. A dual 532 and 1064 nm notch filter (Edmund Optics) takes care of eliminating the Rayleigh-scattered light and attenuating the intense IR light reflected by the other optical surfaces. Additional filtering of the 1064 nm light is provided by a KG5 glass.

The collected Raman signal is then focused by a second 10X focusing lens (Nikon) into the inner cladding layer of another piece of the same double-clad fiber. This waveguide was previously inserted into two heat-shrink tubings which serve as an extra protective coating, as explained in Chapter 5.

The fiber is coupled to a CCD-based spectrometer (QE65000, Ocean Optics), thermo-electrically cooled down to -20°C to reduce dark current noise. The device is equipped with a 1200 lines/mm grating and is capable of signal acquisition in the bandwidth 530 – 697nm. The aperture slit of the spectrometer is 1 mm-high and 50 μm -wide, therefore limiting the collection efficiency of the setup, as discussed in Chapter 5.

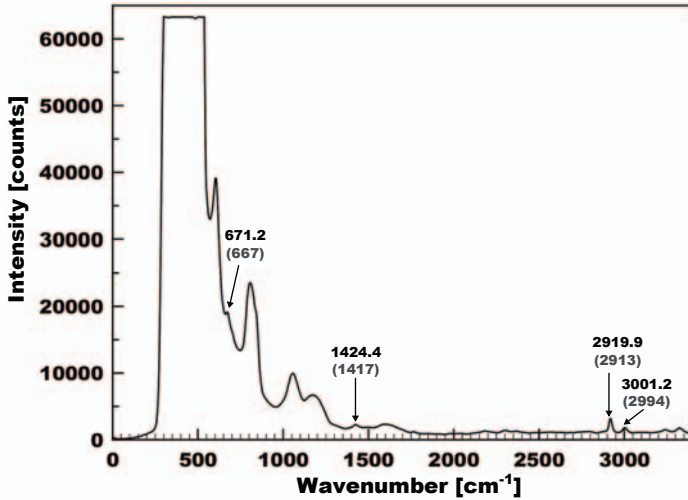


Figure 6.6: Raman spectrum of DMSO acquired with the poled double-clad fiber over an integration time of 15s, repeated twice to avoid the appearance of spectral artifacts. Only the Raman lines located at 671.2, 1424.4, 2919.9 and 3001.2 cm^{-1} are visible, whereas the others are masked by the fiber background emission.

6.3.3 Raman Spectra

At first, a spectrum of DMSO is acquired over a 15s interval, repeated twice to avoid the appearance of artifacts. This spectrum is shown in Fig. 6.6. The peaks of DMSO located at 671.2, 1424.4, 2919.9 and 3001.2 cm^{-1} are visible, despite the presence of an intense fiber spectral background (FSB). For comparison, the Raman lines of DMSO as they appear in the work by Martens et al. [116] are listed in Table 6.1. The few detectable peaks are in good agreement with the reference ones, indicated between parentheses in Fig.6.6.

As explained in Chapter 5, the intense background is mainly due to the amount of fiber emission in the core which is reflected at the fiber/sample interface and which propagates back towards the dichroic component. Additionally, the fraction of the excitation light which is reflected at the fiber end facet also generates FSB on its way back. Unlike the experiment discussed in the previous chapter, however, DMSO drastically reduces the amount of reflected light at the ending cross-section of the waveguide. In case of flat cleave, for example, the Fresnel reflection at the fiber end is approximately 4% for a fiber/air interface and approximately 4

orders of magnitude lower for a fiber/DMSO interface. This explains why, with respect to the spectrum shown in Fig. 5.11 in Chapter 5, the FSB appearing in Fig. 6.6 is less intense and more structured, with a glass peak at 601.6cm^{-1} which is too weak to saturate the detector.

In order to reduce the background due to the fiber emission, a second spectrum is acquired with the tip of the fiber held outside the liquid, at about 10cm from its surface. The measurement is carried out over 15s, repeated twice. This second spectrum is then subtracted from the first one, and the resulting spectral difference is shown in Fig. 6.7.

Table 6.1: Band parameters of DMSO (adapted from [116]).

Band parameter	DMSO (298K)	Assignment
Centre [cm^{-1}]	3010	CH/CD antisymm. stretching
FWHM [cm^{-1}]	6.9	
Relative intensity [%]	0.60	
Centre [cm^{-1}]	3000	CH/CD antisymm. stretching
FWHM [cm^{-1}]	6.9	
Relative intensity [%]	2.72	
Centre [cm^{-1}]	2994	CH/CD antisymm. stretching
FWHM [cm^{-1}]	9.4	
Relative intensity [%]	4.72	
Centre [cm^{-1}]	2913	CH/CD symm. stretching
FWHM [cm^{-1}]	5.4	
Relative intensity [%]	19.20	
Centre [cm^{-1}]	2876	CH/CD symm. stretching
FWHM [cm^{-1}]	21.3	
Relative intensity [%]	0.96	
Centre [cm^{-1}]	2830	CH/CD symm. stretching
FWHM [cm^{-1}]	14.0	
Relative intensity [%]	0.29	
Centre [cm^{-1}]	2809	CH/CD symm. stretching
FWHM [cm^{-1}]	12.3	
Relative intensity [%]	0.41	
Centre [cm^{-1}]	1426	HCH/DCD deformation
FWHM [cm^{-1}]	21.6	
Relative intensity [%]	1.09	
Centre [cm^{-1}]	1417	HCH/DCD deformation
FWHM [cm^{-1}]	18.7	
Relative intensity [%]	3.66	

Continued on next page

Table 6.1 – continued from previous page

Band parameter	DMSO (298K)	Assignment
Centre [cm^{-1}]	1307	HCH/DCD deformation
FWHM [cm^{-1}]	15.3	
Relative intensity [%]	0.47	
Centre [cm^{-1}]	1058	SO symm. stretch of monomer
FWHM [cm^{-1}]	19.8	
Relative intensity [%]	1.54	
Centre [cm^{-1}]	1042	SO antisymm. stretch of dimer
FWHM [cm^{-1}]	23.8	
Relative intensity [%]	4.87	
Centre [cm^{-1}]	1026	SO symm. stretch of dimer
FWHM [cm^{-1}]	22.1	
Relative intensity [%]	0.88	
Centre [cm^{-1}]	953	HCH/DCD rocking
FWHM [cm^{-1}]	19.8	
Relative intensity [%]	1.54	
Centre [cm^{-1}]	698	CS antisymm. stretch
FWHM [cm^{-1}]	13.6	
Relative intensity [%]	11.63	
Centre [cm^{-1}]	667	CS symm. stretch
FWHM [cm^{-1}]	12.6	
Relative intensity [%]	34.64	
Centre [cm^{-1}]	382	CSO in-plane rock
FWHM [cm^{-1}]	11.33	
Relative intensity [%]	2.97	
Centre [cm^{-1}]	333	CSO out-of-plane bend
FWHM [cm^{-1}]	13.1	
Relative intensity [%]	6.12	
Centre [cm^{-1}]	309	CSC out-of-plane bend
FWHM [cm^{-1}]	13.56	
Relative intensity [%]	1.12	

The spectral subtraction reveals the presence of the peaks located at 699.7, 958.9 and 1046.7 cm^{-1} , in addition to those appearing in the original spectrum. The lines located at wavenumbers lower than 500 cm^{-1} cannot be recovered, since in this spectral range the fiber background saturates the detector in both the spectra acquired with the tip of the fiber inside and outside the sample.

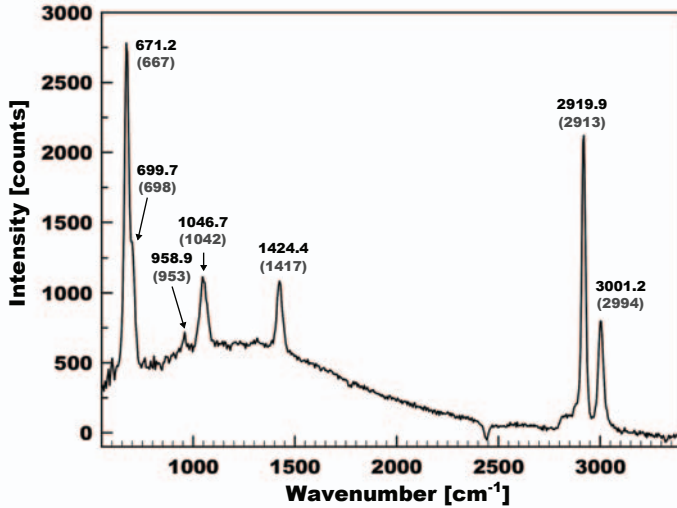


Figure 6.7: Raman spectrum of DMSO obtained from the subtraction of the spectrum of the poled double-clad fiber (FSB) from the spectrum of the sample, acquired with the same waveguide. Both spectra are recorded over a 15s time (repeated twice to avoid artifacts). Indicated on the peaks are the measured (black) and reference (grey, from [116]) Raman shifts. Owing to the saturation of the detector for wavenumbers lower than 550cm^{-1} in both the measurements with and without the sample, only the $550 - 3500\text{cm}^{-1}$ spectral range is shown here.

The notch appearing at about 2450cm^{-1} is an artifact due to the spectral subtraction.

6.4 Double-clad fiber coupler

An *all-in-fiber* Raman probe requires the replacement by a fiber component of the dichroic mirror which separates the laser radiation and the Raman signal. As a proof-of-principle experiment, a double-clad fiber coupler is demonstrated. The device is able to couple the collected Raman scattered light between the inner claddings of two pieces of the same double-clad fiber. The design of such a component follows that suggested by Ryu et al. [100] in their combined fluorescence and optical coherence tomography probe. In particular, the fluorescence signal is excited through the core and collected in the inner cladding, similarly to the operating principle of the Raman probe described in Chapter 5 (though it is worth noting that the Raman signal is normally *six* orders

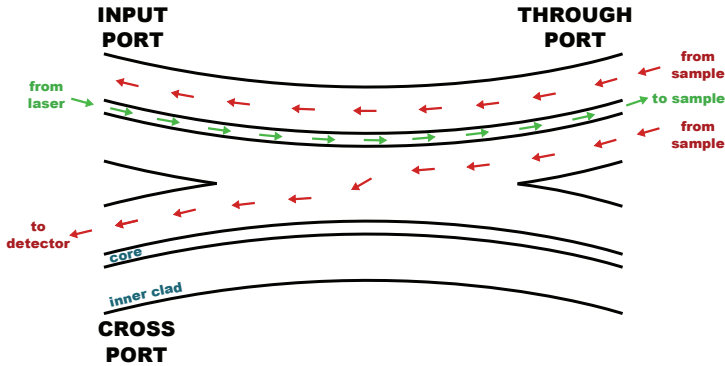


Figure 6.8: Schematic illustration of the working principle of the double-clad fiber coupler, adapted from [100]. For simplicity, the outer cladding region of the two fibers is not shown, and neither is the Rayleigh-scattered light, which is partly coupled between the two waveguides together with the collected Raman scattering.

of magnitude weaker than typical fluorescence signals [11]).

Fig. 6.8 schematically shows the working principle of this coupler. By simply allowing a direct contact between the two inner cladding regions, part of the signal travelling along the inner cladding of the first fiber is coupled out to the second fiber, without perturbing the propagation of the excitation light in the core of the first waveguide.

6.4.1 Coupler fabrication

The coupler is fabricated by locally etching the outer cladding layer of the two pieces of the same double-clad fiber and by crossing the fibers the one over the other for four times. The fabrication process and the determination of the number of crossovers is described in the next paragraphs. For comparison, the coupler presented by Ryu et al. [100] is formed by 28 crossovers over a coupling length of 16cm, for a coupling efficiency of $\sim 30\%$ (wavelength range $680 \div 900\text{nm}$).

Figure 6.9 illustrates the etching procedure. A 8 cm-long section of each fiber is stripped from its acrylate coating by means of a razorblade, and cleaned with ethanol. The outermost 1.5 cm on each side of each stripped section are then covered with a thick layer of nail varnish. This leaves a central 5 cm-wide section of exposed, clean fiber for etching. The nail varnish acts as a mask, protecting the covered sections from the hydrofluoric acid (HF) used to etch the fibers and allowing for the

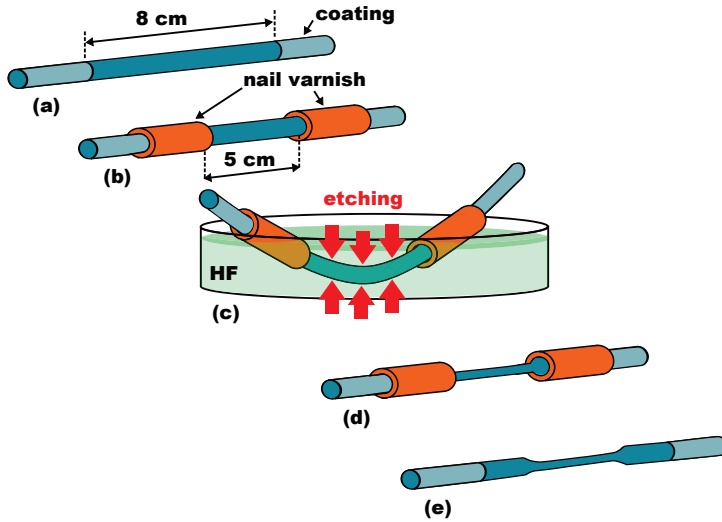


Figure 6.9: The etching process: (a) An 8cm-long section is stripped from the acrylate coating by means of a razorblade and carefully cleaned with ethanol; (b) The outermost 1.5 cm on each side of the stripped section are covered with nail varnish; (c) The stripped section is immersed in HF, with the varnish acting as a mask; (d) The etched section is left to dry and then cleaned with ethanol; (e) The fiber is cleaned with acetone to remove the nail varnish, and then again with ethanol prior to its use.

etching of the sole 5 cm-long exposed sections. The stripped sections are immersed in HF for 30min. This results in a $\sim 30 \mu\text{m}$ -reduction of the fiber radius, enough to ensure the complete removal of the entire $20 \mu\text{m}$ -wide fluorine-doped outer cladding layer. Given its hazardous nature, HF has to be handled with the uttermost care and under a proper fume hood. Once etched, the waveguides are held under a stream of de-ionized water for a few minutes and left to dry. The fibers are then cleaned with acetone in order to remove the nail varnish. Finally, the entire stripped sections are cleaned with ethanol.

The two etched double-clad fibers are then held parallel and their relative position adjusted so that the etched sections are perfectly aligned. Then the waveguides are gently pressed the one against the other, and taped to two translation stages mounted $\sim 17 \text{ cm}$ apart the one from the other. The etched sections remain in between the stages, surrounded by air.

At this point, the two fibers are fixed to one of the stages with UV-curable glue. A drop of UV-curable glue is also poured on the two parallel waveguides immediately before the beginning of their etched

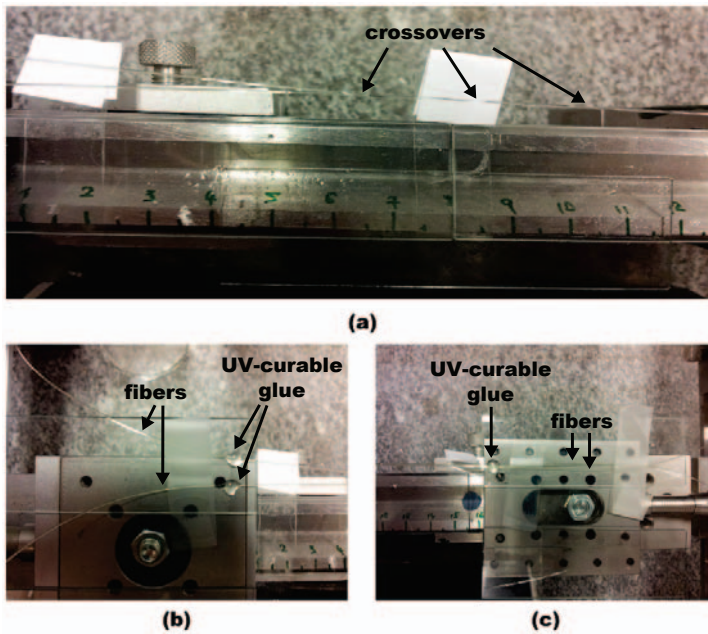


Figure 6.10: (a) Double-clad fibers crossed over each other four times in the coupler. Three crossovers are visible; (b, c) Details of the fibers fixed to the translation stages with UV-curable glue.

section, in order to keep them together. Attention is paid to avoid any contact between the UV-curable glue and the etched section, not to introduce additional losses in the system. Once the glue has solidified, the fibers are crossed the one over the other four times in correspondence of their etched sections, and then fixed to the other translation stage by means of UV-curable glue. Attention is paid not to twist the fibers, in order to avoid unnecessary losses. Three out of four crossovers are indicated in Fig. 6.10 (a). Fig. 6.10 (b) and (c) show the double-clad fibers fixed to the two stages by means of the UV-curable glue.

Once the fibers have been secured to the stages, axial tension is applied in order to ensure a close contact between them, and a drop of index-matching oil (Cargille, $n_D = 1.456$) is poured over the coupling region to facilitate the optical coupling. This represents a rather critical step in the procedure, since an excessive tension results in the breaking of the fibers (after which the entire fabrication process has to be repeated).

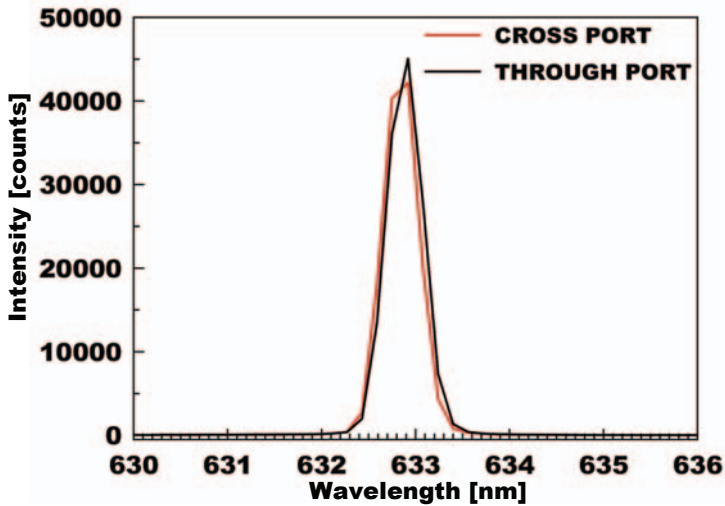


Figure 6.11: Intensity of the signals at the through and cross ports of the coupler with the fibers crossed the one over the other four times, when 632.8 nm light from a HeNe laser is loosely coupled at an angle to the input port. Both signals are recorded over 15s.

Determination of the number of crossovers

The required number of crossovers is determined by trial-and-error, starting with one crossover and increasing the number until a ~ 3 dB coupling is achieved. A 3dB coupling is the maximum that can be expected from the incoherent coupling of a large number of modes in a symmetric arrangement [101]. In particular, the fibers (flat-cleaved with Vytran LDC400) are secured to the stages and tensioned as described in the previous paragraphs, with a drop of index-matching oil poured on the crossovers to facilitate the coupling. Then 632.8 nm light from a HeNe laser (Melles Griot) is loosely coupled at an angle to one of them. The laser radiation is strongly attenuated not to saturate the detector. In the meantime, the output power at the “through” and “cross” ports of the coupler is monitored by means of a CCD-based spectrometer (Ocean Optics QE65000), cooled down to -20°C to avoid dark current noise and equipped with a 1200 lines/mm grating. The remaining *spare* fiber tip is index-matched to avoid reflections.

In case the coupling ratio is measured to be less than the desired 50%, the entire procedure is repeated: the glue which holds the fibers in place on one of the stages is removed by means of a blade, the fibers are “uncrossed” and cleaned from the oil with ethanol, then crossed again

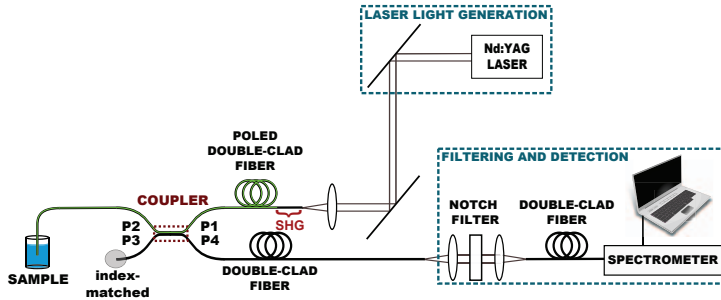


Figure 6.12: Schematic of the experimental setup. Additional “clamping” stages (not shown here) are placed in the setup to ensure the correct positioning of the fibers.

(adding one crossover with respect to the previous measurement) and fixed to the stage with UV-curable glue. The structure is then tensioned and index-matching oil is poured on the coupler.

A final number of four crossovers is found to be enough to ensure a $\sim 3\text{dB}$ coupling (at 632.8nm). Fig. 6.11 shows the intensity at the through and cross ports of the coupler, integrated over 15s.

6.4.2 Experimental setup

Once the coupler is fabricated, one of its two cores is optically poled following the procedure described in Section 6.3.1. An average of $\sim 0.49\text{mW}$ of green light is generated (measured after the focusing lens and an additional IR filter) along in the process, out of the average 450mW of fundamental radiation injected in the fiber.

Prior to the fabrication of the coupler, both waveguides³ had been hydrogen-loaded for about a week at a pressure of 145bar and at room temperature, and then stored at -78°C to prevent any outdiffusion of the hydrogen. This was done to speed up the poling process. Due to some instabilities in the laser power, however, the preparation for SH required a longer time than in the case described in Subsection 6.3.1.

The component is then mounted in the setup schematically illustrated in Fig. 6.12. Light from a Q-switched mode-locked Nd:YAG laser at 1064nm wavelength is coupled into the core of one of the double-clad fibers forming the coupler. Being this fiber optically poled, it generates

³Only the fiber which is to be poled has to be hydrogen-loaded. However, for practical reasons both waveguides were subjected to the process.

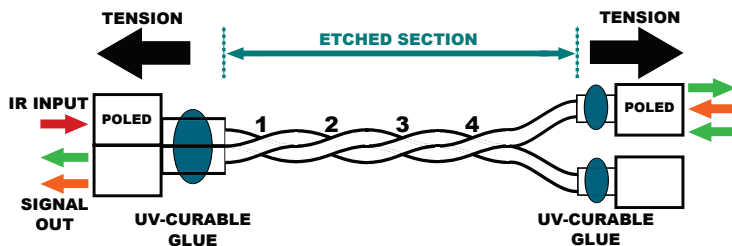


Figure 6.13: Schematic illustration of the double-clad fiber coupler. The fibers are crossed the one over the other four times and tensioned to ensure a close contact. A drop of index-matching oil (not shown) is poured over the coupler to facilitate the coupling. IR light (red arrow) is injected into the core of the poled fiber of the coupler, at the end of which both the fundamental (not shown) and the SH (green arrow) illuminate the sample. The excited scattering is collected in the inner cladding (elastic, green arrow, and inelastic scattering, orange arrow). $\sim 50\%$ of it couples out to the second fiber along the coupling region.

along its core the 532nm radiation needed to excite Raman scattering in a sample of DMSO, into which the distal end of the same waveguide is dipped. The scattering is collected in the inner cladding of the same fiber. Along the coupler region, approximately 50% of the collected light is transferred to the inner cladding of the other fiber (see Fig. 6.13), at the end of which the signal is filtered and then coupled to another piece of the same double-clad fiber. This waveguide delivers the filtered signal to the spectrometer (Ocean Optics QE65000), set as in the experiment described in Subsection 6.3.2. The remaining *spare* fiber tip is index-matched to avoid reflections.

Prior to the optical poling, the fiber end which is to be immersed in the sample and the one which is to be index-matched were re-cleaved at an angle of $\sim 8^\circ$, in order to reduce the reflections.

6.4.3 Raman Spectra

A Raman spectrum of DMSO is acquired over an integration time of 15s, repeated three times to avoid the appearance of artifacts in the spectrum. The spectrum is shown in Fig. 6.14.

The Raman lines at 671.2, 1424.4, 2919.9 and 3001.2cm^{-1} are visible in the spectrum, whereas the others are covered by the fiber background. It is worth noting that these are the same peaks appearing in the spectrum acquired *without* the coupler (Fig. 6.6), despite the fact that only part

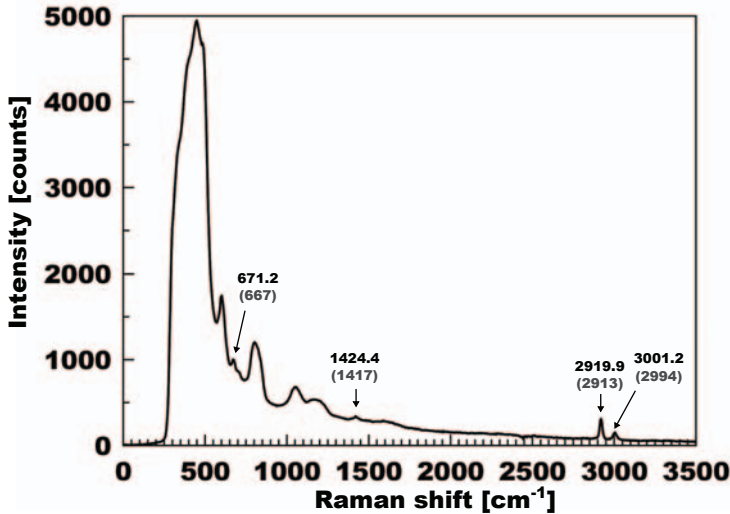


Figure 6.14: Raman spectrum of DMSO acquired with the poled double-clad fiber coupler probe over an integration time of 15s, repeated three times. Only the Raman lines located at 671.2, 1424.4, 2919.9 and 3001.2 cm^{-1} are visible, whereas the others are masked by the fiber background emission. Between parentheses, the reference values from [116].

of the collected signal ($\sim 50\%$) is transmitted to the spectrometer, and that moreover the excitation light is in this case weaker.

As expected, the FSB is significantly less intense than in the absence of the coupler (see for example Fig. 6.6). This is due to the fact that the biggest contribution to the background emission propagates in the core of the waveguide which delivers the excitation light to the sample, as previously explained in Section 6.3. Thus, in this case it does not couple out to the second fiber. Whenever a bulk dichroic mirror is used for the demultiplexing of laser and collected radiation, as for instance in the previous experiment, all the FSB propagating in the core is transferred to the spectrometer, resulting in a huge spectral background.

The ratio of the intensities of the DMSO peak at 2919.9 cm^{-1} and the FSB peak at 802.3 cm^{-1} (arbitrarily chosen as reference peaks for the two signals) in the coupler-based probe (Fig. 6.14) compares favourably with the case of the poled double-clad fiber without the coupler (Fig. 6.6). The former, 0.26, is twice as high as the latter, 0.13.

A second spectrum is then acquired with the tip of the fiber outside the sample, to be subtracted from the first one. This spectral subtrac-

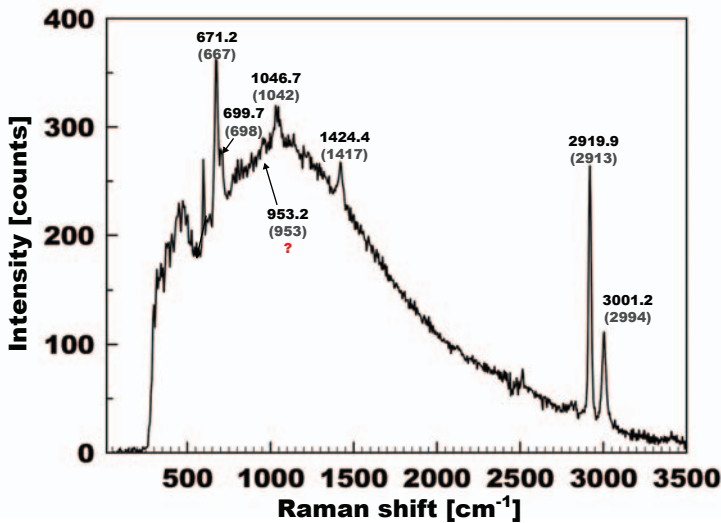


Figure 6.15: Raman spectrum of DMSO resulting from the subtraction of spectrum of the poled double-clad fiber coupler (FSB) from the spectrum of the sample, acquired with the same probe. Both spectra are recorded over a 15s interval, repeated three times. Indicated on the lines are the Raman shifts, compared to the reference values from [116].

tion, shown in Fig. 6.15, results in the appearance of the lines at 699.7 and 1046.7cm⁻¹. The attribution of the line located at 953.2cm⁻¹ is uncertain, given the level of noise in the spectrum.

The entire 0 ÷ 3500cm⁻¹ range is shown in the spectral subtraction, since this time the interfering emission from the fiber does not saturate the detector. The “hunchbacked” profile of the spectrum, less noticeable but yet present even in the spectrum from Fig. 6.7, is due to the slightly different intensities of the recorded FSB in the measurements with and without the sample, and to the fact that this background signal is mainly affecting the short-wavelength side of the spectrum.

As mentioned at the beginning of this chapter, this experiment was meant as a proof of principle, aiming at demonstrating that an optically-poled double-clad fiber coupler can efficiently be integrated into an all-in-fiber Raman probe. The positive results obtained in the field of fluorescence spectroscopy with a similar structure [100], though not optically-poled, were indeed encouraging, and yet given the difference in intensity between the typical Raman and fluorescence signals (\sim six orders of magnitude) even the detection of the few most intense peaks of DMSO (those located at 671.2, 2919.9 and 3001.2cm⁻¹) was deemed to represent a

good result. The outcome of this experiment exceeds any expectations, since not only the most intense Raman lines, but also the majority of the weaker ones appears in the collected Raman spectrum (Fig. 6.15).

With the instrumentation available at the end of this experiment, the losses of such a probe (compared to the case without the coupler) could not be evaluated. It is however reasonable to expect that an optimized version of such a coupler, for example an analogous structure fabricated by fusing the two fibers together (FBT technique), will give better results in terms of the overall loss. Additionally, fabrication by FBT method will improve the mechanical stability of the device, allowing for its on-field application.

The integration of a proper in-fiber Rayleigh-rejection filter in the setup would further reduce the overall system losses, by allowing for the elimination of the notch filter and of the objective lenses in between which it is placed, and also of the additional piece of double-clad fiber used to convey the filtered light to the spectrometer.

6.5 Summary

In this chapter, two single-fiber Raman probe configurations are presented. The first device is a single optically-poled double-clad fiber, and requires a bulk dichroic component to retrieve the collected Raman scattering from its inner cladding. It is however able to generate the desired 532nm excitation light along its core while illuminated with 1064nm laser radiation, due to optical poling. The second probe is formed by two double-clad fibers (one of which optically poled), crossed over each other four times to form a fiber coupler. In addition to its ability to generate the excitation light in the visible range along the core of one of its waveguides (owing to optical poling), the component is also able to couple $\sim 50\%$ of the collected scattering between the inner-cladding regions of the two fibers, thus replacing the dichroic mirror used in the previous experiment to demultiplex the laser and collected radiation.

Chapter 7

Conclusion and future developments

No matter where you are in life, there is always more journey ahead.

Nelson Mandela

The development of fiber Raman probes has opened up for new and, at least until two decades ago, unthinkable applications of Raman spectroscopy. The combination of Raman spectroscopy and fiber optics technology has allowed for minimally invasive *in-vivo* investigations of hardly accessible samples, such as the inside of stomach and intestine and other human organs. Analysis in hazardous environments, for instance at high temperature or pressure conditions or in the presence of highly toxic materials, were also made possible by fiber probes.

Fiber Raman probes are compact and flexible devices. Compared to conventional bulk-optics-based probes, they are not subject to alignment issues and are overall more rugged and reliable. Ever since the first demonstration of a fiber-based Raman probe in the early eighties, a number of them have been reported. Single- and multi-fiber geometries have been proposed in the attempt to optimize aspects like the delivery of the excitation light and sample illumination, and (especially) the collection efficiency of the devices.

In-fiber Raman spectroscopy being such a mature technique, in this Ph.D. project efforts were made to demonstrate novel solutions meant to complete the work done so far by others, taking one step further towards the realization of an all-in-fiber Raman system.

Assuming the possibility to use a fiber laser emitting a fundamental 1064nm radiation, the in-fiber wavelength conversion required to obtain an excitation light in the green range was achieved by optically poling the core of the waveguide delivering the excitation signal to the sample. Optical poling allows for efficient in-fiber second harmonic generation (SHG) by recording a permanent periodic grating along the waveguide.

A double-clad fiber, i.e. a step-index structure characterized by two concentric cladding layers surrounding the core, was used to simultaneously deliver the excitation light to the sample and to collect the scattered radiation. In particular, the former signal was guided in the core whereas the latter was guided in the inner cladding. This was possible owing to the overall index distribution of the waveguide, $n_{core} > n_{clad,in} > n_{clad,out}$, where $n_{clad,in}$ and $n_{clad,out}$ represent the refractive indices of the inner- and outer-cladding regions, respectively.

In this Thesis, two Raman probes based on this double-clad fiber were presented. The first was realized by injecting light at 532nm into the core of the waveguide by means of a bulk dichroic component, also used to recover the collected Raman signal from the inner cladding. In this case, the excitation light originated from the frequency doubling of light at 1064nm performed by a nonlinear crystal. The device allowed for accurate Raman spectroscopic measurements of a sample of cyclohexane, provided that the strong fiber spectral background (FSB) was removed. This was done by recording a spectrum of the fiber and subtracting it from the spectrum of the sample. The Raman lines at 1444.9 and 2858.4 cm^{-1} , together with the double peak at 2928.2 and 2940.3 cm^{-1} were already visible in the spectrum affected by the fiber background emission, whereas additional ones at 802.3, 1030.3, 1160.6, 1267.3 and 2669.8 cm^{-1} appeared after the spectral subtraction.

The second device was realized by optically poling the double-clad fiber prior to its employment. An average of $\sim 0.83\text{mW}$ of light at 532nm was generated in $\sim 4\text{h}$ by exposing the core of the fiber to an average of $\sim 450\text{mW}$ of 1064nm light. The frequency-doubled light was used to perform Raman spectroscopic analyses of a sample of dimethyl sulfoxide (DMSO). Unlike cyclohexane, this solvent allowed for the immersion of the fiber end into the liquid, without giving rise to cavitation bubbles somehow responsible for destructive fiber fuses. A rather accurate spectrum of DMSO was obtained by subtracting the spectrum of the fiber from the spectrum of the sample. With respect to the double-clad fiber which was *not* poled, a weaker contribution from the FSB was measured. This was very likely due to the index-matching action of the sample and

to the fact that the generation of the excitation light along the core prevents any FSB arising in the inner-cladding from a bad in-coupling of the laser radiation.

As a proof-of-principle experiment, a double-clad fiber coupler was realized in order to recover the collected Raman signal from the inner cladding of a double-clad fiber, without perturbing the propagation of the excitation light along the core. The device was realized by etching away the outer-cladding layer of two pieces of the same double-clad fiber and crossing the two waveguides four times the one over the other along their etched section. This scheme was adapted from a design previously introduced by Ryu et al. [100] for a fluorescence spectroscopy probe. However, it is worth noting that the typical fluorescence signal is normally about *six* orders of magnitude more intense than Raman signals, therefore the successful demonstration of an analogous coupler for a Raman spectroscopic experiment was not taken for granted. The number of crossovers was determined with a trial-and-error procedure until a coupling of ~ 3 dB between the inner-cladding regions of the two fibers was reached. A 3dB coupling is the maximum that can be expected from the incoherent coupling of a large number of modes in a symmetric arrangement. The coupling was measured at 632.8nm, the wavelength of a HeNe laser, a few nm away from two among the most intense peaks of DMSO (located at 2919.9cm^{-1} , that is 629.84nm, and 3001.2cm^{-1} , that is 633.24nm).

Once the coupler was realized, one of its fibers was optically poled. The generated green light was used to perform a Raman spectroscopic measurement of a sample of DMSO. The ending tip of the fiber was once again immersed in the liquid. The three most intense peaks from the solvent (671.2cm^{-1} , 2919.9cm^{-1} and 3001.2cm^{-1}) were clearly visible, together with one weaker line (1424.4cm^{-1}). The other lines were masked by the FSB. In order to obtain a clearer result, the spectrum of the fiber was subtracted from that of the sample, resulting in the appearance of the Raman bands peaks at 699.7cm^{-1} and 1046.7cm^{-1} . The intensity of the FSB affecting the measurement was considerably lower, with respect to the case of the single poled fiber without coupler. This is due to the fact that a (bulk) dichroic component used to recover the signal from the inner cladding of the waveguide also transmits all wavelengths other than the excitation one which are guided in the core of the fiber, thus collecting the highest contribution to the FSB. The double-clad fiber coupler, instead, retrieves the sole signal propagating in the inner-cladding region. An intuitive estimation of this improvement was given by comparing the ratio between one Raman peak from DMSO and one

peak from the background signal, arbitrarily chosen, in the cases of the probe with and without the coupler. The former was measured to be twice as high as the latter.

A tunable and low-loss all-in-fiber Rayleigh-rejection filter was also demonstrated in this work. The device was based on a photonic crystal fiber (PCF), i.e. a waveguide presenting a periodic distribution of air holes in the cladding region which is invariant along the longitudinal direction. The structure was infiltrated with a material with a higher refractive index than silica, so that guidance by the photonic bandgap (PBG) effect was made possible. PBG fibers exhibit spectral *bandgaps*, that is guidance of light is only allowed within certain wavelength ranges, while the transmission of light at other wavelengths is inhibited by the surrounding microstructure. Thus these structure behave like spectral filters. By choosing a filling material with thermo-optical properties, the spectral characteristic of the infiltrated-fiber can be tuned by changing the temperature of the filled section. The filter described in this Thesis was characterized by an insertion loss of 0.3dB and a full width at half maximum (FWHM) bandwidth of 143nm. A 32nm shift of the central wavelength was measured while tuning the temperature of the device from 22°C to 70°C. The spectrum of the component at these two temperature values was simulated by means of a finite element method (FEM) code. Considering that the mathematical model does not account for propagation losses, the simulated and experimental results are in good agreement. The device was employed in a Raman spectroscopic measurement of a sample of cyclohexane. In particular, the temperature of the filter was varied until the maximum attenuation of the Rayleigh line was found (65°C), then a Raman spectrum of the solvent was acquired. Raman lines at 1010, 1432, 2830, 2902 and 2912 cm^{-1} were visible in the spectrum, whereas the intense peak at 801.3 cm^{-1} was strongly attenuated by a small notch appearing in the spectrum of the filter.

The integration of the fiber components here described allows for the realization of an all-in-fiber Raman probe. The optimization of the double-clad fiber coupler by means of the fused biconical taper (FBT) technique or even the incorporation of a suitable micro-lens on the ending facet of the fiber are possible developments which will improve the results achieved so far. When complemented with a fiber laser emitting at 1064nm and a fiber-based spectrometer, whose demonstration seems nowadays much less unlikely than it did three years ago (see for example the work recently reported by Redding and Cao [117]), this probe will be part of a *complete* all-in-fiber Raman system. No similar system has

ever been demonstrated.

Thus, the results obtained during this Ph.D. project represent a further step in the field of in-fiber Raman spectroscopy, showing significant progress towards the realization of a truly all-in-fiber Raman system.

7.1 Future developments

At this point in time, the “building blocks” required to assemble the above-mentioned all-in fiber Raman probe (ideally, the all-in-fiber Raman *system*) are all available. The immediate future developments of this project are obviously the optimization of the single components and their integration into a complete device.

Investigations on the microscopic mechanisms behind optical poling stopped soon after thermal poling was invented, and so did all attempts to improve its conversion efficiency. Even though it is possible that a way to improve the efficiency of the optical poling process exists, *thermally* poling the fiber used to deliver the excitation light to the sample is the most straightforward way to optimize the devices realized in this work. In the case of a weaker scatterer than cyclohexane and DMSO (like for example the samples from the FøSu project), a higher conversion efficiency will make the difference between the detection of a Raman signal and no signal at all.

A more intense excitation light propagating along the core of the double-clad fiber translates into a more intense FSB. This in turn means that the use of a fiber coupler to recover the collected Raman signal from the inner cladding is necessary, in order to avoid a bulk dichroic mirror which would propagate the background emission from the waveguide towards the spectrometer.

The optimization of the coupler described in this Thesis implies its realization by means of the FBT technique. By fusing the two fibers together the insertion loss of the component will likely decrease, whereas its mechanical stability will be improved. The cumbersome structure which, as of now, holds the coupler in place won't be needed anymore, and the device will be ready for in-field measurements. However, while fusing the fibers to make the coupler it is important not to taper them down to such a small size that the propagation of the excitation light along one of the cores is perturbed by the component.

The *in-situ* application of the Rayleigh-rejection filter based on the PCF infiltrated with a high-index liquid requires the development of *portable* thermal plate and controller. On-chip integration of devices based on liquid crystal-filled PBG fibers and electrodes was recently demonstrated by Wei et al. [118], thus it is reasonable to think that a similar solution can be applied to the component here presented. However, in order to be used in conjunction with the double-clad fiber devices a different PCF will be needed, thus a different filter will have to be designed.

Once assembled together, these components need to be tested to better define their working conditions. For example, the conversion efficiency of an optically-poled fiber which is not polarization maintaining (PM) is sensitive to the temperature in the room. Thus, as of now the devices presented in this Thesis are not suitable for applications in thermally-unstable environments. Nevertheless, the fermentation processes studied within the FøSu project are run in thermally-controlled environments (30°C), thus the thermal stability of the poled components can be ensured.

7.1.1 Novel applications

Aside from the incorporation of a micro-lens on the fiber ending facet (if allowed by the specific application), other additions can be made to the devices presented in this Thesis, in order to “tailor” them for other applications.

SERS probe

More than one decade ago Stokes and Vo-Dinh [119] demonstrated a single-fiber surface-enhanced Raman spectroscopy (SERS) sensor. SERS technology relies on the enhancement in the Raman signal of a sample resulting from the interaction of the excitation light with a metallic nanostructured *substrate* onto which the given sample is adsorbed. This enhancement, which under optimized conditions can be of several orders of magnitude, is due to both electromagnetic and chemical factors. However, the electromagnetic contribution is known to be the most relevant.

The electromagnetic enhancement factor is related to the generation of intense localized electric fields at protrusions from the the metallic nanostructure of the substrate; these fields interact with the adsorbed

molecules to yield increased Raman scattering. In particular, the excitation light incident on the metallic surface induces an oscillation in the conductance electrons of the metal (*surface plasmons*), thus generating a secondary electric field which can be much more intense than the incident one, depending on the shape and size of the nanostructure.

In their work, Stokes and Vo-Dinh realized a single-fiber SERS probe by coating the ending $\sim 1\text{cm}$ of a $600\mu\text{m}$ -wide waveguide (outer diameter) with a nanoparticle-based SERS-active substrate, after the removal of the original coating and cladding. A first layer of alumina particles provided the surface roughness necessary to produce intense localized fields. A 1\AA -wide layer of silver later deposited on top of the alumina one provided the surface plasmons.

Both the end facet and the side walls of the fiber along the final $\sim 1\text{cm}$ were coated. However, the authors were not able to estimate the contribution to the SERS enhancement related to the coated side of the fiber, if any.

It is reasonable to expect that a double-clad fiber probe like the ones presented in this Thesis can be employed in a similar SERS experiment. By coating its end facet with a *proper* SERS-active material, an enhancement of the collected field is to be expected. The choice of the substrate, in terms of the metal and size/shape of the nanostructure, depends on the specific application. In particular, the wavelength used to excite the plasmons and the sample to be studied are important design parameters.

Microfluidic Raman probe

A microfluidic component can be realized by splicing the end facet of the optically-poled double-clad fiber to the side of a glass capillary tube, which acts as a sample “chamber”. The other side of the capillary tube is spliced to a 2-hole (2H) fiber, characterized by two holes on the sides of the core running along the entire length of the waveguide. The device is schematically illustrated in Fig. 7.1. The holes of the 2H fiber act as the inlet and outlet of the (liquid) sample, which flows inside the chamber and in front of the core of the double-clad fiber. The liquid is illuminated from the core of the waveguide, and the excited scattering is collected into the inner-cladding region, and coupled out to another fiber of the same kind by means of a double-clad fiber coupler.

Components based on a similar design were previously demonstrated,

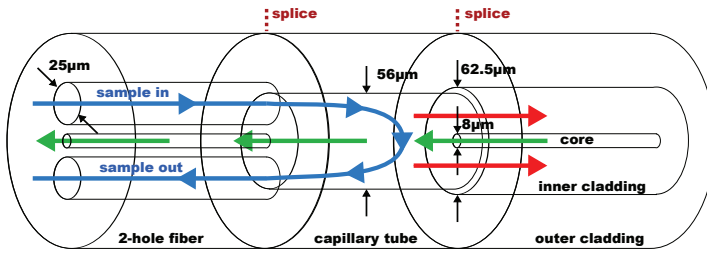


Figure 7.1: Schematic illustration of the microfluidic Raman component. The device is realized by splicing a 2-hole fiber (left) and a double-clad fiber (right) on the sides of a glass capillary tube (center). The double-clad fiber shown here is a smaller version of the waveguide used in this Ph.D. project.

see for example the work by Lopez-Cortes et al. [120].

For simplicity, the dimensions appearing in Fig. 7.1 refer to real fibers fabricated by Acreo Fiberlab. In particular, the double-clad fiber is a smaller version of the waveguide used in this work. The core and claddings diameters are $8\mu\text{m}$, $62.5\mu\text{m}$ (inner cladding) and $125\mu\text{m}$ (outer cladding), respectively.

The contribution to the Raman signal from glass due to the inner wall of the capillary might be significant. However, it is worth considering the possibility to coat the inner wall of the capillary with a SERS-active substrate, in order to enhance the Raman signal from the sample.

In the case of a Raman spectroscopic measurement, the alignment between the cores of the 2H and double-clad fibers is not critical.

On the quotes appearing in this Thesis

Dante Alighieri (~ 1265 - 1321) was a major Italian poet of the Middle Ages. His *La divina commedia* (Divine Comedy) is considered the greatest literary work ever composed in the Italian language.

Ray D. Bradbury (1920 - 2012) was an American fantasy, science fiction, horror and mystery fiction writer.

Russell A. Kirsch (1929 -) is one of the inventors of the first internally-programmable computer, the so-called Standards Eastern Automatic Computer (SEAC). The device was capable of scanning digital images and in 1957 produced the first ever digital picture.

Stephen W. Hawking (1942 -) is a British theoretical physicist and author.

Isaac Newton (1642 - 1727) was an English physicist, mathematician, astronomer, natural philosopher, alchemist and theologian.

Rita Levi-Montalcini (1909 -) is an Italian neurologist who, together with her colleague Stanley Cohen, received the 1986 Nobel Prize in Physiology or Medicine for their discovery of the nerve growth factor (NGF).

Andre K. Agassi (1970 -) is a retired American professional tennis player.

Charles L. Dodgson (1832 - 1898), better known by the pseudonym **Lewis Carroll**, was an English author, mathematician, logician, Anglican deacon and photographer.

Nelson R. Mandela (1918 -) is a South African politician who also served as President of South Africa from 1994 to 1999, the first ever to

be elected in a fully representative democratic election.

The text in this page was adapted from www.wikipedia.org

Acronyms

BP band-pass

CARS coherent anti-stokes Raman spectroscopy

CCD charge-coupled device

CW continuous wave

DMSO dimethyl sulfoxide

DPSS diode-pumped solid state

FBG fiber Bragg grating

FBT fused biconical taper

FEM finite element method

FSB fiber spectral background

FWHM full width at half maximum

HC hollow-core

IR infrared

LMA large mode area

LP long-pass

MM multi-mode

M-TIR modified total internal reflection

NA numerical aperture

PBG photonic bandgap

PCF photonic crystal fiber

PM polarization maintaining

- QPM** quasi-phase matching
- SEM** scanning electron microscope
- SERS** surface-enhanced Raman spectroscopy
- SH** second harmonic
- SHG** second harmonic generation
- SM** single-mode
- SP** short-pass
- SNR** signal to noise ratio
- TERS** tip-enhanced Raman spectroscopy
- TIR** total internal reflection
- UV** ultraviolet

Bibliography

- [1] A.L. Schawlow and C.H. Townes. Infrared and optical masers. *Physics Review*, 112:1940–1949, 1958.
- [2] W.S. Boyle and G.E. Smith. Charge coupled semiconductor devices. *Bell System Technical Journal*, 49(4):587–593, 1970.
- [3] P. Vandenabeele, H.G.M. Edwards, and L. Moens. A decade of Raman spectroscopy in art and archaeology. *Chemical Reviews*, 107(3):675–686, 2007.
- [4] E.L. Izake. Forensic and homeland security applications of modern portable Raman spectroscopy. *Forensic Science International*, 202(1-3):1–8, 2010.
- [5] N. Tarcea, T. Frosch, P. Rösch, M. Hilchenbach, T. Stuffer, S. Hofer, H. Thiele, R. Hochleitner, and J. Popp. Raman Spectroscopy-A powerful tool for in situ planetary science. In Oliver Botta, Jeffrey L. Bada, Javier Gomez-Elvira, Emmanuelle Javaux, Franck Selsis, and Roger Summons, editors, *Strategies of Life Detection*, volume 25 of *Space Sciences Series of ISSI*, pages 281–292. Springer US, 2008.
- [6] L.-P. Choo-Smith, H. G. M. Edwards, H. P. Endtz, J. M. Kros, F. Heule, H. Barr, J. S. Robinson, H. A. Bruining, and G. J. Puppels. Medical applications of Raman spectroscopy: From proof of principle to clinical implementation. *Biopolymers*, 67(1):1–9, 2002.
- [7] E.E. Lawson, B.W. Barry, A.C. Williams, and H.G.M. Edwards. Biomedical applications of Raman spectroscopy. *Journal of Raman Spectroscopy*, 28(2-3):111–117, 1997.
- [8] I. Nabiev, I. Chourpa, and M. Manfait. Applications of Raman and surface-enhanced Raman scattering spectroscopy in medicine. *Journal of Raman Spectroscopy*, 25(1):13–23, 1994.

- [9] G. R. Trott and T. E. Furtak. Angular resolved Raman scattering using fiber optic probes. *Review of Scientific Instruments*, 51(11):1493–1496, 1980.
- [10] R.L. McCreery, M. Fleischmann, and P. Hendra. Fiber optic probe for remote Raman spectrometry. *Analytical Chemistry*, 55(1):146–148, 1983.
- [11] U. Utzinger and R.R. Richards-Kortum. Fiber optic probes for biomedical optical spectroscopy. *Journal of Biomedical Optics*, 8(1):121–47, 2003.
- [12] H. Sato, H. Shinzawa, and Y. Komachi. Fiber-optic Raman probes for biomedical and pharmaceutical applications. In Pavel Matousek and Michael D. Morris, editors, *Emerging Raman Applications and Techniques in Biomedical and Pharmaceutical Fields*, Biological and Medical Physics, Biomedical Engineering, pages 25–45. Springer Berlin Heidelberg, 2010.
- [13] M.G. Shim, B.C. Wilson, E. Marple, and M. Wach. Study of fiber-optic probes for in vivo medical Raman spectroscopy. *Applied Spectroscopy*, 53(6):619–627, 1999.
- [14] J.T. Motz, M. Hunter, L.H. Galindo, J.A. Gardecki, J.R. Kramer, R.R. Dasari, and M.S. Feld. Optical fiber probe for biomedical Raman spectroscopy. *Applied optics*, 43(3):542–54, 2004.
- [15] F. Bylund, E. Collet, S.-O. Enfors, and G. Larsson. Substrate gradient formation in the large-scale bioreactor lowers cell yield and increases by-product formation. *Bioprocess and Biosystems Engineering*, 18:171–180, 1998.
- [16] S. George, G. Larsson, K. Olsson, and S.-O. Enfors. Comparison of the baker’s yeast process performance in laboratory and production scale. *Bioprocess and Biosystems Engineering*, 18:135–142, 1998.
- [17] S.-O. Enfors, M. Jahic, A. Rozkov, B. Xu, M. Hecker, B. Jürgen, E. Krüger, T. Schweder, G. Hamer, D. O’Beirne, N. Noisommit-Rizzi, M. Reuss, L. Boone, C. Hewitt, C. McFarlane, A. Nienow, T. Kovacs, C. Trägårdh, L. Fuchs, J. Revstedt, P.C. Friberg, B. Hjertager, G. Blomsten, H. Skogman, S. Hjort, F. Hoeks, H.-Y. Lin, P. Neubauer, R. van der Lans, K. Luyben, P. Vrabel, and Å. Manelius. Physiological responses to mixing in large scale bioreactors. *Journal of Biotechnology*, 85(2):175–185, 2001.

- [18] C.J. Hewitt, G. Nebe-Von Caron, A.W. Nienow, and C.M. McFarlane. The use of multi-parameter flow cytometry to compare the physiological response of *Escherichia coli* W3110 to glucose limitation during batch, fed-batch and continuous culture cultivations. *Journal of Biotechnology*, 75:251–264, 1999.
- [19] R. Lencastre Fernandes, M. Nierychlo, L. Lundin, A.E. Pedersen, P.E. Puentes Tellez, A. Dutta, M. Carlquist, A. Bolic, D. Schäpper, A.C. Brunetti, S. Helmark, A.-L. Heins, A.D. Jensen, I. Nopens, K. Rottwitt, N. Szita, J.D. van Elsas, P.H. Nielsen, J. Martinussen, S.J. Sørensen, A.E. Lantz, and K.V. Gernaey. Experimental methods and modeling techniques for description of cell population heterogeneity. *Biotechnology Advances*, 29(6):575–599, 2011.
- [20] K.C. Schuster, E. Urlaub, and J.R. Gapes. Single-cell analysis of bacteria by Raman microscopy: spectral information on the chemical composition of cells and on the heterogeneity in a culture. *Journal of Microbiological Methods*, 42(1):29–38, 2000.
- [21] Choo-Smith L.-P., Maquelin K., van Vreeswijk T., H.A. Bruining, G.J. Puppels, N.A. Ngo Thi, C. Kirschner, D. Naumann, D. Ami, A.M. Villa, F. Orsini, S.M. Doglia, H. Lamfarraj, G.D. Sockalingum, M. Manfait, P. Allouch, and H.P. Endtz. Investigating microbial (micro)colony heterogeneity by vibrational spectroscopy. *Applied Environmental Microbiology*, 67:11461–11469, 2001.
- [22] A.E. Cervera, N. Petersen, A.E. Lantz, A. Larsen, and K.V. Gernaey. Application of near-infrared spectroscopy for monitoring and control of cell culture and fermentation. *Biotechnology Progress*, 25(6):1561–1581, 2009.
- [23] H. Qu, B. Ung, F. Boismumu, N. Guo, A. Depuis, and M. Skorobogatiy. Photonic bandgap fiber bundle spectrometer. In *Optical Sensors*, page SThB5. Optical Society of America, 2010.
- [24] A.C. Brunetti, L. Scolari, T. Lund-Hansen, and K. Rottwitt. Low-loss tunable all-in-fiber filter for Raman spectroscopy. In *Optical Sensors*, page SWA3. Optical Society of America, 2011.
- [25] A.C. Brunetti, L. Scolari, T. Lund-Hansen, J. Weirich, and K. Rottwitt. All-in-fibre Rayleigh-rejection filter for Raman spectroscopy. *Electronics Letters*, 48(5):275–276, 2012.
- [26] A.C. Brunetti, W. Margulis, and K. Rottwitt. Raman probe based

- on optically-poled double-core fiber. In *Optical Sensors*, page STu1F.6. Optical Society of America, 2012.
- [27] C.V. Raman and K.S. Krishnan. A new type of secondary radiation. *Nature*, 121:501–502, 1928.
- [28] A. Smekal. Zur quantentheorie der dispersion. *Naturwissenschaften*, 11:873–875, 1923.
- [29] G.R. Sims. Principles of charge-transfer devices. In J.V. Sweedler, K.L. Ratzlaff, and M. Bonner Dento, editors, *Charge-transfer devices in spectroscopy*. VCH, New York, 1994.
- [30] R.L. McCreery. CCD array detectors for multichannel Raman spectroscopy. In J.V. Sweedler, K.L. Ratzlaff, and M. Bonner Dento, editors, *Charge-transfer devices in spectroscopy*. VCH, New York, 1994.
- [31] T. Hirschfeld and B. Chase. FT-Raman spectroscopy: Development and justification. *Applied Spectroscopy*, 40(2):133–137, 1986.
- [32] R.L. McCreery. *Raman Spectroscopy for Chemical Analysis*. John Wiley & Sons, 2005.
- [33] G. Fini. Applications of Raman spectroscopy to pharmacy. *Journal of Raman Spectroscopy*, 35(5):335–337, 2004.
- [34] F. Adar, R. Geiger, and J. Noonan. Raman spectroscopy for process/quality control. *Applied Spectroscopy Reviews*, 32(1-2):45–101, 1997.
- [35] J.R. Lombardi and R.L. Birke. A unified approach to surface-enhanced Raman spectroscopy. *The Journal of Physical Chemistry C*, 112(14):5605–5617, 2008.
- [36] Begley R.F., Harvey A.B., and Byer R.L. Coherent anti-Stokes Raman spectroscopy. *Applied Physics Letters*, 25(7):387–390, 1974.
- [37] W. M. Tolles, J. W. Nibler, J. R. McDonald, and A. B. Harvey. A review of the theory and application of coherent anti-stokes Raman spectroscopy (CARS). *Applied Spectroscopy*, 31(4):253–271.
- [38] V. Deckert. Tip-enhanced Raman spectroscopy. *Journal of Raman Spectroscopy*, 40(10):1336–1337, 2009.
- [39] D.A. Long. *The Raman effect: a unified treatment of the theory of Raman scattering by molecules*. John Wiley & Sons, 2001.

- [40] Nestor J.R. and Lippincott E.R. The effect of the internal field on Raman scattering cross sections. *Journal of Raman Spectroscopy*, 1(15):305–318, 1973.
- [41] Y. Komachi, H. Sato, K. Aizawa, and H. Tashiro. Micro-optical fiber probe for use in an intravascular Raman endoscope. *Applied optics*, 44(22):4722–32, 2005.
- [42] T. Aabo, I.R. Perch-Nielsen, J.S. Dam, D.Z. Palima, H. Siegumfeldt, J. Glückstad, and N. Arneborg. Effect of long- and short-term exposure to laser light at 1070 nm on growth of *saccharomyces cerevisiae*. *Journal of Biomedical Optics*, 15(4):041505 1–7, 2011.
- [43] A. Downes and A. Elfick. Raman spectroscopy and related techniques in biomedicine. *Sensors*, 10(3):1871–89, 2010.
- [44] I. Notingher, S. Verrier, H. Romanska, a. E. Bishop, J. M. Polak, and L. L. Hench. In situ characterisation of living cells by Raman spectroscopy. *Spectroscopy*, 16(2):43–51, 2002.
- [45] G.J. Puppels, J.H. Olminkhof, G.M. Segers-Nolten, C. Otto, F.F. de Mul, and J. Greve. Laser irradiation and Raman spectroscopy of single living cells and chromosomes: sample degradation occurs with 514.5nm but not with 660nm laser light. *Experimental Cell Research*, 195(2):361–367, 1991.
- [46] K.P.J. Williams and D.L. Gerrard. The use of 752.5 and 799.3 nm laser excitation in Raman spectroscopy. *Optics & Laser Technology*, 17(5):245–248, 1985.
- [47] B.T. Bowie, D. Bruce Chase, and P.R. Griffiths. Factors affecting the performance of bench-top Raman spectrometers. Part 2: Effect of sample. *Applied Spectroscopy*, 54(6):200–207, 2000.
- [48] A. Klehr, B. Sumpf, M. Maiwald, and H. Schmidt. Method and device for producing and detecting a Raman spectrum. *US Patent*, 0204715 A1, 2008.
- [49] B.T. Bowie, D. Bruce Chase, and P.R. Griffiths. Factors affecting the performance of bench-top Raman spectrometers. Part 1: Instrumental effects. *Applied Spectroscopy*, 54(5):164–173, 2000.
- [50] X. Fang and S. Ahmad. Detection of explosive vapour using surface-enhanced Raman spectroscopy. *Applied Physics B: Lasers and Optics*, 97:723–726, 2009.

- [51] D.S. Moore and R.J. Scharff. Portable Raman explosives detection. *Analytical and Bioanalytical Chemistry*, 393:1571–1578, 2009.
- [52] S.D. Harvey, M.E. Vucelick, R.N. Lee, and B.W. Wright. Blind field test evaluation of Raman spectroscopy as a forensic tool. *Forensic Science International*, 125(1):12–21, 2002.
- [53] M.L. Myrick, J. Kolis, E. Parsons, K. Chike, M. Lovelace, W. Scrivens, R. Holliday, and M. Williams. In situ fiber-optic Raman spectroscopy of organic chemistry in a supercritical water reactor. *Journal of Raman Spectroscopy*, 25(1):59–65, 1994.
- [54] M.M. Carrabba and R.D. Rauh. Apparatus for measuring Raman spectra over optical fibers. *US Patent*, 5112127, 1992.
- [55] I.R. Lewis and P.R. Griffiths. Raman spectrometry with fiber-optic sampling. *Applied Spectroscopy*, 50(10):12A–30A, 1996.
- [56] T.F. Cooney, H.T. Skinner, and S.M. Angel. Comparative study of some fiber-optic remote Raman probe designs. Part I: Model for liquids and transparent solids. *Applied Spectroscopy*, 50(7):836–848, 1996.
- [57] T.F. Cooney, H.T. Skinner, and S.M. Angel. Comparative Study of Some Fiber-Optic Remote Raman Probe Designs. Part II: Tests of Single-Fiber, Lensed, and Flat- and Bevel-Tip Multi-Fiber Probes. *Applied Spectroscopy*, 50(7):849–860, 1996.
- [58] J.M. Berg, K.C. Rau, D.K. Veirs, L.A. Worl, J.T. McFarlan, and D.D. Hill. Performance of fiber-optic Raman probes for analysis of gas mixtures in enclosures. *Applied Spectroscopy*, 56(1):83–90, 2002.
- [59] S.D. Schwab and R.L. McCreery. Versatile, efficient Raman sampling with fiber optics. *Analytical Chemistry*, 56(12):2199–2204, 1984.
- [60] E. Gantner and D. Steinert. Applications of laser Raman-spectrometry in process-control using optical fibers. *Fresenius' Journal of Analytical Chemistry*, 338(1):2–8, 1990.
- [61] M.L. Myrick, S.M. Angel, and R. Desiderio. Comparison of some fiber optic configurations for measurement of luminescence and Raman scattering. *Applied Optics*, 29(9):1333–1344, 1990.
- [62] C.K. Chong, C. Shen, Y. Fong, J. Zhu, F.-X. Yan, S. Brush, C.K.

- Mann, and T.J. Vickers. Raman spectroscopy with a fiber-optic probe. *Vibrational Spectroscopy*, 3:35–45, 1992.
- [63] J. Ma and Y.-S. Li. Fiber Raman background study and its application in setting up optical fiber Raman probes. *Applied Optics*, 35(15):2527–2533, 1996.
- [64] S.O. Konorov, C.J. Addison, H.G. Schulze, R.F.B. Turner, and M.W. Blades. Hollow-core photonic crystal fiber-optic probes for Raman spectroscopy. *Optics letters*, 31(12):1911–1913, 2006.
- [65] M.J. Pelletier. Fiber optic probe with integral optical filtering. *US Patent*, 5862273, 1999.
- [66] W.W. Morey, G. Meltz, and W.H. Glenn. Fiber optic bragg grating sensors. volume 1169, pages 98–107. SPIE, 1989.
- [67] A. Iocco, H.G. Limberger, R.P. Salathe, L.A. Everall, K.E. Chisholm, J.A.R. Williams, and I. Bennion. Bragg grating fast tunable filter for wavelength division multiplexing. *Journal of Lightwave Technology*, 17(7):1217, 1999.
- [68] H.G. Limberger, Nguyen H.K., D.M. Costantini, R.P. Salathe, C.A.P. Muller, and G.R. Fox. Efficient miniature fiber-optic tunable filter based on intracore Bragg grating and electrically resistive coating. *IEEE Photonics Technology Letters*, 10(3):361–363, 1998.
- [69] M.R. Mokhtar, C.S. Goh, S.A. Butler, S.Y. Set, K. Kikuchi, D.J. Richardson, and M. Ibsen. Fibre Bragg grating compression-tuned over 110 nm. *Electronics Letters*, 39(6):509–511, 2003.
- [70] E. Yablonovitch. Inhibited spontaneous emission in solid-state physics and electronics. *Physical Review Letters*, 58(20):2059–2062, 1987.
- [71] S. John. Strong localization of photons in certain disordered dielectric superlattices. *Physics Review Letters*, 58:2486–2489, 1987.
- [72] J.C. Knight, T.A. Birks, P. St.J. Russell, and D.M. Atkin. All-silica single-mode optical fiber with photonic crystal cladding. *Optics Letters*, 21(19):1547–1549, 1996.
- [73] J.C. Knight, J. Broeng, T. A. Birks, and P.St.J. Russell. Photonic band gap guidance in optical fibers. *Science*, 282(5393):1476–1478, 1998.

- [74] T.A. Birks, J.C. Knight, and P.S.J. Russell. Endlessly single-mode photonic crystal fiber. *Optics Letters*, 22(13):961–963, 1997.
- [75] P. Russell. Photonic crystal fibers. *Science*, 299(5605):358–362, 2003.
- [76] R.T. Bise, R.S. Windeler, K.S. Kranz, C. Kerbage, B.J. Eggleton, and D.J. Trevor. Tunable photonic band gap fiber. *Optical Fiber Communication Conference OFC 2002*, pages 466–468, 2002.
- [77] Jesper Lægsgaard. Gap formation and guided modes in photonic bandgap fibres with high-index rods. *Journal of Optics A: Pure and Applied Optics*, 6(8):798–804, 2004.
- [78] L. Scolari. *Liquid crystal in photonic crystal fibres: fabrication, characterization and devices*. PhD thesis, Technical University of Denmark, Denmark.
- [79] N.M. Litchinitser, A.K. Abeeluck, C. Headley, and B.J. Eggleton. Antiresonant reflecting photonic crystal optical waveguides. *Optics Letters*, 27(18):1592–1594, 2002.
- [80] N.M. Litchinitser, S.C. Dunn, B. Usner, B.J. Eggleton, T.P. White, R.C. McPhedran, and C.M. de Sterke. Resonances in microstructured optical waveguides. *Optics Express*, 11(10):1243–1251, 2003.
- [81] A.K. Abeeluck, N.M. Litchinitser, C. Headley, and B.J. Eggleton. Analysis of spectral characteristics of photonic bandgap waveguides. *Optics Express*, 10(23):1320–1333, 2002.
- [82] N.M. Litchinitser, S.C. Dunn, P.E. Steinvurzel, B.J. Eggleton, T.P. White, R.C. McPhedran, and C.M. de Sterke. Application of an ARROW model for designing tunable photonic devices. *Optics Express*, 12(8):1540–1550, 2004.
- [83] A.C. Brunetti, L. Scolari, J. Weirich, L. Eskildsen, G. Bellanca, P. Bassi, and A. Bjarklev. Gaussian filtering with tapered oil-filled photonic bandgap fibers. In *Proceedings of 1st Workshop on Specialty Optical Fibers and Their Applications WSOF 2008*, pages 113–116, 2008.
- [84] T.T. Alkeskjold. *Optical devices based in liquid crystal photonic bandgap fibers*. PhD thesis, Technical University of Denmark, Denmark.

- [85] J. Weirich. *Liquid Crystal Photonic Bandgap Fibers: Modeling and Devices*. PhD thesis, Technical University of Denmark, Denmark.
- [86] T.R. Wolinski, K. Szaniawska, S. Ertman, P. Lesiak, A.W. Domanski, R. Dabrowski, E. Nowinowski-Kruszelnicki, and J. Wojcik. Influence of temperature and electrical fields on propagation properties of photonic liquid-crystal fibres. *Measurement Science and Technology*, 17(5):985–991, 2006.
- [87] K.R. Khan and T.X. Wu. Finite element modeling of dual-core photonic crystal fiber. *Applied Computational Electromagnetics*, 23(3):215–219, 2008.
- [88] I.H. Malitson. Interspecimen comparison of the refractive index of fused silica. *Journal of the Optical Society of America*, 55(10):1205–1209, 1965.
- [89] J. Weirich, J. Lægsgaard, L. Scolari, L. Wei, T.T. Alkeskjold, and A. Bjarklev. Biased liquid crystal infiltrated photonic bandgap fiber. *Optics Express*, 17(6):4442–4453, 2009.
- [90] McCreery Research Group. Raman shift frequency standards. URL <http://www.chem.ualberta.ca/~mccreery/ramanmaterials.html>.
- [91] D. Yelin, B.E. Bouma, S.H. Yun, and G.J. Tearney. Double-clad fiber for endoscopy. *Optics letters*, 29(20):2408–2410, 2004.
- [92] B.S. Wang and E.W. Mies. Review of fabrication techniques for fused fiber components for fiber lasers. In *Proceedings of SPIE 7195, Fiber Lasers VI: Technology, Systems, and Applications*, pages 71950A–1–11, 2009.
- [93] A. Phillip and W. Lauterborn. Cavitation erosion by single laser-produced bubbles. *Journal of Fluid Mechanics*, 361:75–116, 1998.
- [94] R.M. Atkins, P.G. Simpkins, and A.D. Yablon. Track of a fiber fuse: A Rayleigh instability in optical waveguides. *Optics Letters*, 28(12):974–976, 2003.
- [95] R. Kashyap. Poling of glasses and optical fibers. In *Fiber Bragg Gratings*, pages 527–596. Academic press, 2nd edition, 2009.
- [96] S.R.J. Brueck R.A. Myers, N. Mukherhee. Large second-order nonlinearity in poled fused silica. *Optics Letters*, 16(22):1732–1734, 1991.

- [97] A. Canagasabay, C. Corbari, A.V. Gladyshev, F. Liegeois, S. Guillemet, Y. Hernandez, M.V. Yashkov, A. Kosolapov, E.M. Dianov, M. Ibsen, and P.G. Kazansky. High-average-power second-harmonic generation from periodically poled silica fibers. *Optics Letters*, 34:2483–2485, 2009.
- [98] L. Wang, H.Y. Choi, Y. Jung, B.H. Lee Byeong Ha, and K.-T. Kim. Optical probe based on double-clad optical fiber for fluorescence spectroscopy. *Optics Express*, 15(26):17681–17689, 2007.
- [99] H. Bao, S.Y. Ryu, B.H. Lee, W. Tao, and M. Gu. Nonlinear endomicroscopy using a double-clad fiber coupler. *Optics Letters*, 35:995–997, 2010.
- [100] S.-Y. Ryu, H.-Y. Choi, M.-J. Ju, J.-H. Na, W.-J. Choi, and B.-H. Lee. The development of double clad fiber and double clad fiber coupler for fiber based biomedical imaging systems. *Journal of the Optical Society of Korea*, 13(3):310–315, 2009.
- [101] S. Lemire-Renaud, M. Rivard, M. Strupler, D. Morneau, F. Verpillat, X. Daxhelet, N. Godbout, and C. Boudoux. Double-clad fiber coupler for endoscopy. *Optics Express*, 18(6):9755–9764, 2010.
- [102] Y. Fujii, B.S. Kawasaki, K.O. Hill, and D.C. Johnson. Sum-frequency light generation in optical fibers. *Optics Letters*, 5(2):48–50, 1980.
- [103] Y. Sasaki and Y. Ohmori. Phase-matched sum-frequency light generation in optical fibers. *Applied Physics Letters*, 39(6):466–468, 1981.
- [104] U. Österberg and W. Margulis. Dye laser pumped by Nd:YAG laser pulses frequency doubled in a glass optical fiber. *Optics Letters*, 11:516–518, 1986.
- [105] I.C.S. Carvalho, W. Margulis, and B. Lesche. Second-order nonlinear effects in optical fibers. In H.S. Nalwa, editor, *Polymer optical fibers*, pages 127–166. American Scientific Publishers, 2004.
- [106] E.E. Dianov, P.G. Kazansky, and D.Y. Stepanov. Photovoltaic model of photoinduced second harmonic generation in optical fibers. *Soviet Lightwave Communication*, 1:247–253, 1991.
- [107] J.A. Armstrong, N. Bloembergen, J. Ducuing, and P.S. Pershan. Interaction between light waves in a nonlinear dielectric. *Physics Reviews*, 127(6):1918–1939, 1962.

- [108] R.H. Stolen and H.W.K. Tom. Self-organized phase-matched harmonic generation in optical fibers. *Optics Letters*, 12(8):585–587, 1987.
- [109] W. Margulis, F. Laurell, and B. Lesche. Imaging the nonlinear grating in frequency-doubling fibres. *Nature*, 378:699–701, 1995.
- [110] M.M. Lacerda, I.C.S. Carvalho, W. Margulis, and B. Lesche. Grating evolution in frequency-doubling fibers. *Optics Letters*, 19(13):948–950, 1994.
- [111] P.J. Lemaire, R.M. Atkins, V. Mizrahi, and W.A. Reed. High pressure H_2 loading as a technique for achieving ultrahigh UV photosensitivity and thermal sensitivity in GeO_2 doped optical fibres. *Electronics Letters*, 29(13):1191–1193, 1993.
- [112] F. Ouellette, K.O. Hill, and D.C. Johnson. Enhancement of second-harmonic generation in optical fibers by a hydrogen and heat treatment. *Applied Physics Letters*, 54(12):1086–1088, 1989.
- [113] W. Margulis. Private communication, 2011.
- [114] Y.T. Shah, A.B. Pandit, and Moholkar. Factors affecting cavitation behavior. In Dan Luss, editor, *Cavitation Reaction Engineering*, The Plenum Chemical Engineering Series, pages 55–83. Springer US, 1999.
- [115] C. Reichardt. *Solvents and Solvent Effects in Organic Chemistry*. Wiley-VCH, 3rd edition, 2003.
- [116] W.N. Martens, R.L. Frost, J. Kristof, and J. Theo Klopogge. Raman spectroscopy of dimethyl sulphoxide and deuterated dimethyl sulphoxide at 298 and 77K. *Journal of Raman Spectroscopy*, 33:84–91, 2002.
- [117] B. Redding and H. Cao. Using a multimode fiber as a high-resolution, low-loss spectrometer. *Optics Letters*, 37(16):3384–3386, 2012.
- [118] L. Wei, J. Weirich, T.T. Alkeskjold, and A. Bjarklev. On-chip tunable long-period grating devices based on liquid crystal photonic bandgap fibers. *Optics Letters*, 34(24):3818–3820, 2009.
- [119] D.L. Stokes and T. Vo-Dinh. Development of an integrated single-fiber SERS sensor. *Sensors and Actuators B: Chemical*, 69(1-2):28–36, 2000.

- [120] D. Lopez-Cortes, O. Tarasenko, and W. Margulis. All-fiber Kerr cell. *Optics Letters*, 37(15):3288–3290, 2012.



Copyright: Anna Chiara Brunetti
and DTU Fotonik
All rights reserved
ISBN: 87-92062-95-4

Published by:
DTU Fotonik
Department of Photonics Engineering
Technical University of Denmark
Ørsteds Plads, building 343
DK-2800 Kgs. Lyngby

Anna Chiara Brunetti was born in 1983 in Faenza (RA), Italy. Shortly after obtaining her M.Sc. Degree in Telecommunications Engineering (University of Bologna, 2009), she started a Ph.D. project at the Technical University of Denmark, under the supervision of Prof. Karsten Rottwitt (main supervisor) and Prof. Krist V. Gernaey (co-supervisor). The Ph.D. Thesis was successfully defended on October 15, 2012, in front of an evaluation committee consisting of Prof. Christiano De Matos (Universidade Presbiteriana Mackenzie, São Pedro, Brasil), Prof. Gilberto Brambilla (University of Southampton, UK), and Ass. Prof. Peter Tidemand-Lichtenberg (DTU Fotonik, Denmark).